

Technical Memorandum No. 33-191

*Maximum Model-Size Determination and Effects
of the Sting Diameter on an Entry Shape and
Sphere for Low Supersonic Mach-Number Testing*

J.G. Herrera

GPO PRICE \$ _____

OTS PRICE(S) \$ _____

Hard copy (HC) 3.00

Microfiche (MF) .50

**JET PROPULSION LABORATORY
CALIFORNIA INSTITUTE OF TECHNOLOGY
PASADENA, CALIFORNIA**

October 30, 1964

N65-26407

(ACCESSION NUMBER)

57

(PAGES)

CR 63429

(NASA CR OR TMX OR AD NUMBER)

(THRU)

1

(CODE)

01

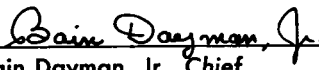
(CATEGORY)

Sgt 2976

Technical Memorandum No. 33-191

***Maximum Model-Size Determination and Effects
of the Sting Diameter on an Entry Shape and
Sphere for Low Supersonic Mach-Number Testing***

J. G. Herrera


Bain Dayman, Jr., Chief
Aerodynamic Facilities Section

**JET PROPULSION LABORATORY
CALIFORNIA INSTITUTE OF TECHNOLOGY
PASADENA, CALIFORNIA**

October 30, 1964

Copyright © 1964
Jet Propulsion Laboratory
California Institute of Technology

Prepared Under Contract No. NAS 7-100
National Aeronautics & Space Administration

CONTENTS

I. Introduction	1
II. Model Description	1
III. Wind Tunnel and Instrumentation	3
IV. Test Procedure	4
V. Data Reduction	5
VI. Conclusions	5
Nomenclature	9
References	10
Plots	11

TABLE

1. Run summary	4
--------------------------	---

FIGURES

1. Shadowgraph of 2.5-in.-diam. sphere with 1.1-in.-diam. sting	2
2. Entry-shape sting mounted in 20-in. supersonic wind tunnel	2
3. Shadowgraph of 2.5-in.-diam. entry shape with 1.1-in.-diam. sting	3
4. Sphere drag-force coefficient and base free-stream static-pressure ratio as a function of Mach number	6
5. Schlieren photograph of 3.0-in.-diam. entry shape on a 1.1-in.-diam. sting with supersonic flow established and with tunnel blocked, Mach No. 1.40	7
6. Schlieren photograph of 3.5-in.-diam. entry shape showing bow wave due to presence of the tunnel boundaries	7

PLOTS

1. C_L vs α for a sphere	11
2. C_D vs α for a sphere	11
3. C_m vs α for a sphere	11
4. P_b/P vs α for a sphere	12
5. C_L vs α for a sphere	12

PLOTS (Cont'd)

6. C_D vs α for a sphere	12
7. C_m vs α for a sphere	13
8. P_b/P vs α for a sphere	13
9. C_L vs α for a sphere	14
10. C_D vs α for a sphere	14
11. C_m vs α for a sphere	14
12. P_b/P vs α for a sphere	15
13. C_N vs α for an entry shape	15
14. C_{D_c} vs α for an entry shape	16
15. $-C_m$ vs α for an entry shape	16
16. P_b/P vs α for an entry shape	17
17. C_N vs α for an entry shape	17
18. C_{D_c} vs α for an entry shape	17
19. $-C_m$ vs α for an entry shape	18
20. P_b/P vs α for an entry shape	18
21. C_N vs α for an entry shape	19
22. C_{D_c} vs α for an entry shape	19
23. $-C_m$ vs α for an entry shape	20
24. P_b/P vs α for an entry shape	20
25. C_N vs α for an entry shape	21
26. C_N vs α for an entry shape	21
27. C_N vs α for an entry shape	21
28. C_N vs α for an entry shape	22
29. C_N vs α for an entry shape	22
30. C_{D_c} vs α for an entry shape	23
31. C_{D_c} vs α for an entry shape	23
32. C_{D_c} vs α for an entry shape	24
33. C_{D_c} vs α for an entry shape	24
34. C_{D_c} vs α for an entry shape	25
35. $-C_m$ vs α for an entry shape	25
36. $-C_m$ vs α for an entry shape	26
37. $-C_m$ vs α for an entry shape	26
38. $-C_m$ vs α for an entry shape	27

PLOTS (Cont'd)

72. C_M vs Mach for a sphere	44
73. C_M vs Mach for a sphere	44
74. P_b/P vs Mach for a sphere	45
75. P_b/P vs Mach for a sphere	45
76. P_b/P vs Mach for a sphere	46
77. P_b/P vs Mach for a sphere	46
78. P_b/P vs Mach for a sphere	47
79. C.P. (in.) vs Mach for a sphere	47
80. C.P. (in.) vs Mach for a sphere	48
81. C.P. (in.) vs Mach for a sphere	48
82. C.P. (in.) vs Mach for a sphere	49
83. C_m vs model diameter (in.) for a sphere	49
84. C_m vs model diameter (in.) for a sphere	50
85. $-C_m$ vs model diameter (in.) for an entry shape	50
86. $-C_m$ vs model diameter (in.) for an entry shape	51
87. $-C_m$ vs model diameter (in.) for an entry shape	51
88. $-C_m$ vs model diameter (in.) for an entry shape	51

PLOTS (Cont'd)

39. $-C_m$ vs α for an entry shape	27
40. P_b/P vs α for an entry shape	28
41. P_b/P vs α for an entry shape	28
42. P_b/P vs α for an entry shape	29
43. P_b/P vs α for an entry shape	29
44. P_b/P vs α for an entry shape	30
45. C_N vs Mach for an entry shape	30
46. C_N vs Mach for an entry shape	31
47. C_N vs Mach for an entry shape	31
48. C_N vs Mach for an entry shape	32
49. C_N vs Mach for an entry shape	32
50. C_M vs Mach for an entry shape	33
51. C_M vs Mach for an entry shape	33
52. C_M vs Mach for an entry shape	34
53. C_M vs Mach for an entry shape	34
54. C_M vs Mach for an entry shape	35
55. P_b/P vs Mach for an entry shape	35
56. P_b/P vs Mach for an entry shape	36
57. P_b/P vs Mach for an entry shape	36
58. P_b/P vs Mach for an entry shape	37
59. P_b/P vs Mach for an entry shape	37
60. C.P. (in.) vs Mach for an entry shape	38
61. C.P. (in.) vs Mach for an entry shape	38
62. C.P. (in.) vs Mach for an entry shape	39
63. C.P. (in.) vs Mach for an entry shape	39
64. C_L vs Mach for a sphere	40
65. C_L vs Mach for a sphere	40
66. C_L vs Mach for a sphere	41
67. C_L vs Mach for a sphere	41
68. C_L vs Mach for a sphere	42
69. C_M vs Mach for a sphere	42
70. C_M vs Mach for a sphere	43
71. C_M vs Mach for a sphere	43

ABSTRACT

26407

This Report describes the experimental determination of the maximum-size entry shape that could be tested at a low supersonic Mach number in the 20-in. wind tunnel at the Jet Propulsion Laboratory (JPL). In addition basic aerodynamic sphere data, to supplement existing data, and the effect of sting diameter on the aerodynamic characteristics are included. Tunnel blockage is discussed, and base flow data are presented.

Author

I. INTRODUCTION

This test program was initiated in an effort to aid the prime contractor for the *Apollo* project, Space and Information Division of North American Aviation, Inc. (Downey, Calif.), in the fabrication of the appropriate-size test models. In most wind-tunnel tests where a force model is employed, it is typically required that the model be built as large as permitted in order that relatively large aerodynamic forces and moments might be experi-

enced by the model (Ref. 1). This is particularly important for some configurations where the apparent variation in forces and moments might be difficult to resolve. Moreover, since the *Apollo* testing program consisted of various types of tests (force, moment, pressure, dynamic stability, etc.) with several different models, it was imperative that the allowable maximum size be used to accommodate the instrumentation inside the model.

II. MODEL DESCRIPTION

The two basic configurations tested were (1) a sphere and (2) an entry shape (Fig. 1, 2, and 3). A total of six different models were employed; these consisted of three

spheres, 2.5, 3.0, and 3.5 in. diam., and three entry-shape configurations of the same three base diameters (dimensions are perpendicular to axis of symmetry).

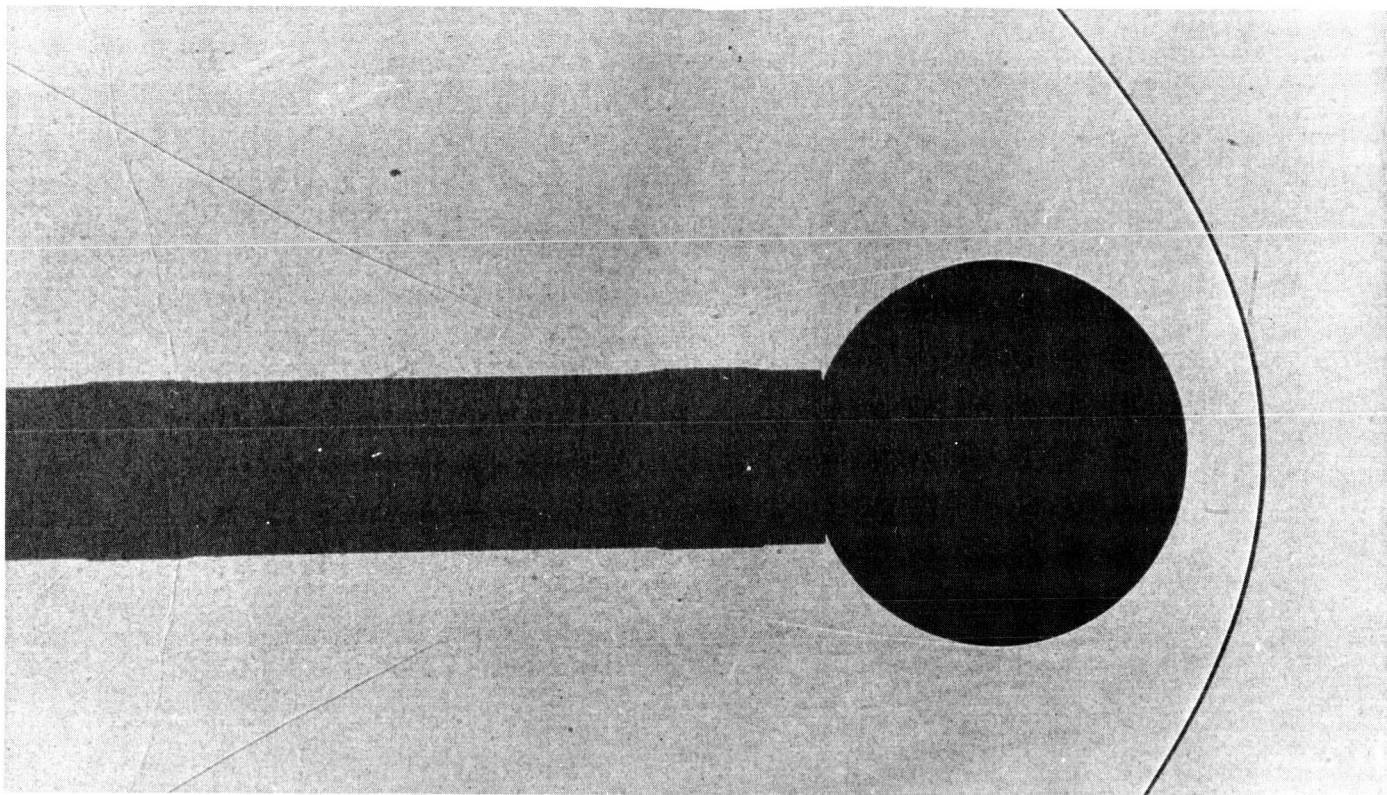


Fig. 1. Shadowgraph of 2.5-in.-diam. sphere with 1.1-in.-diam. sting

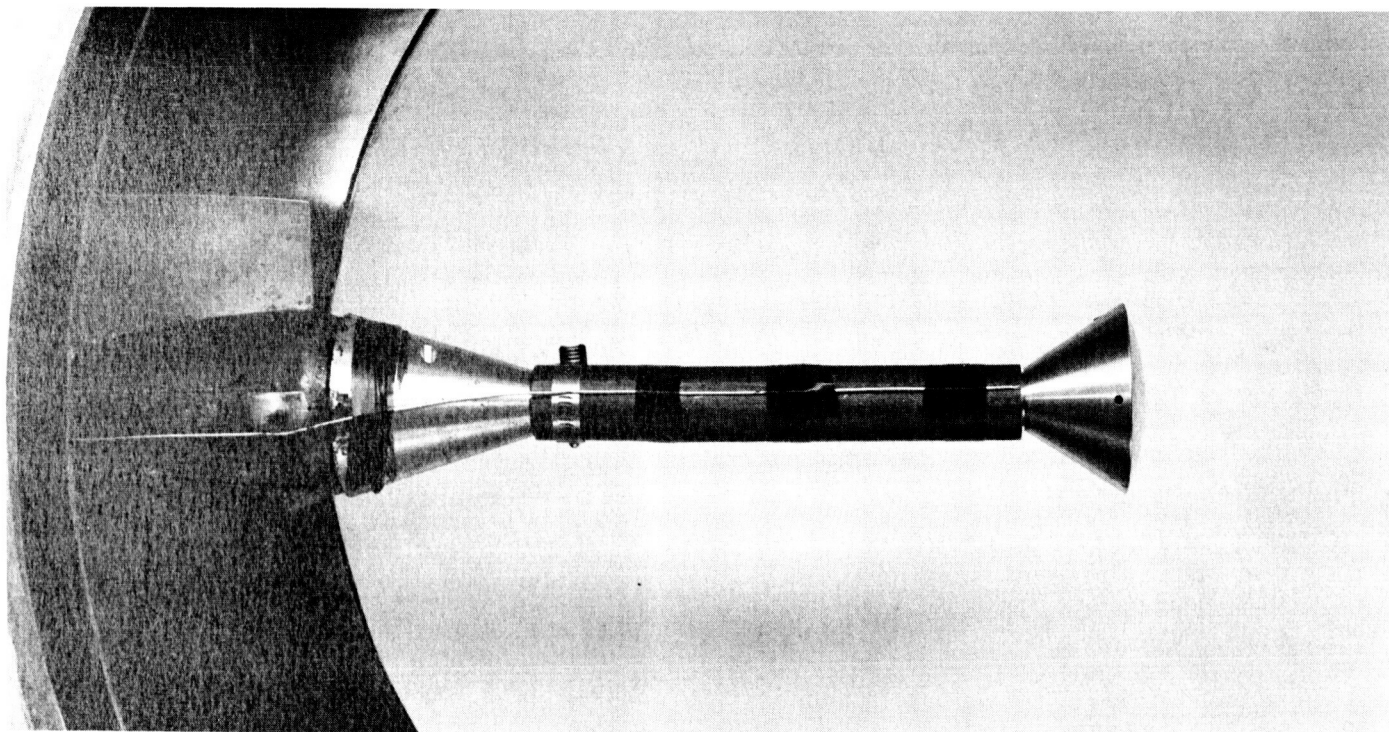


Fig. 2. Entry-shape sting mounted in 20-in. supersonic wind tunnel

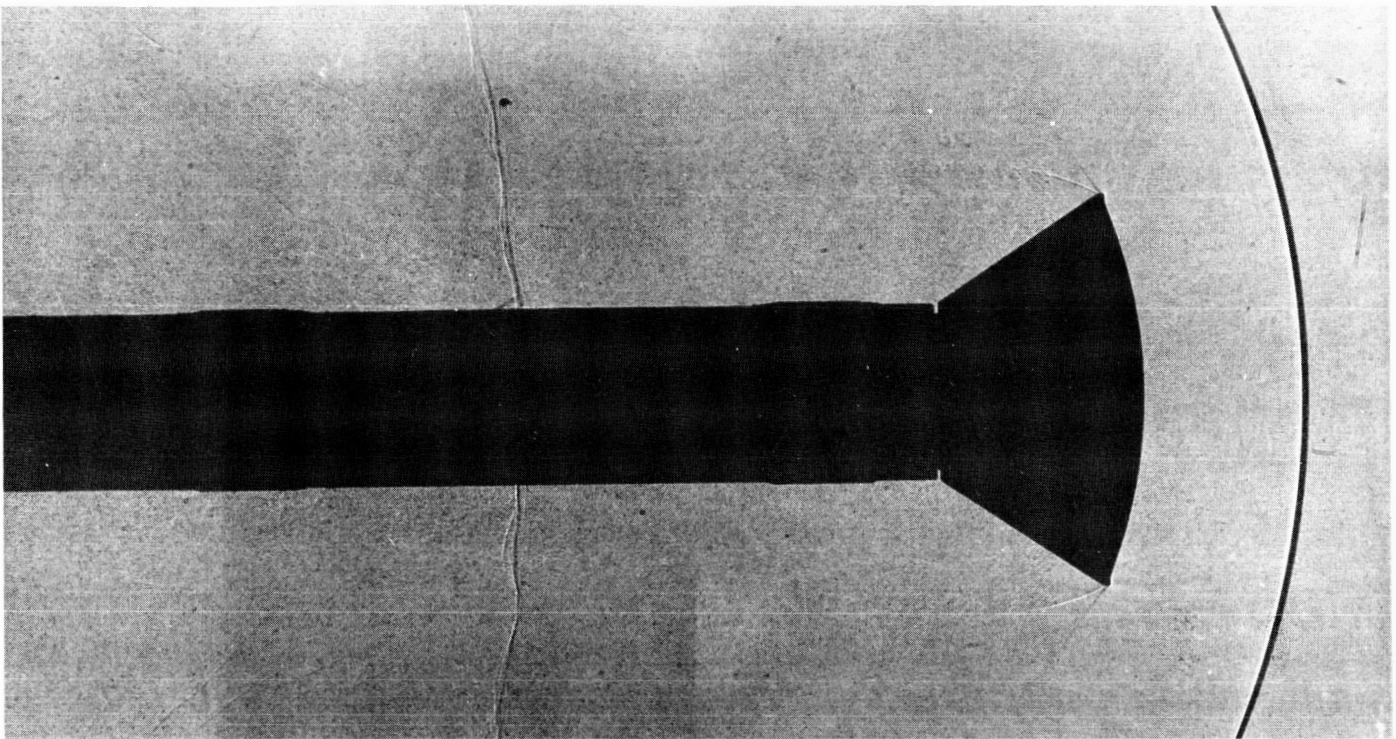


Fig. 3. Shadowgraph of 2.5-in.-diam. entry shape with 1.1-in.-diam. sting

III. WIND TUNNEL AND INSTRUMENTATION

Design features of the 20-in. wind tunnel permit its continuous operation as either a variable-density closed circuit or an open-circuit facility. For this test, it was operated as a closed-circuit tunnel. Any value of test-section Mach number between 1.33 and 5.60 may be set remotely.

For normal operation, however, nineteen calibrated Mach numbers which range from 1.33 to 5.01 are available. Operation at other than calibrated Mach numbers is based on interpolated nozzle settings and, in some instances, on partial calibrations. At all Mach numbers,

the test section is nominally 20 in. high and 18 in. wide. Additional information is contained in Ref. 2.

A six-component, internal, strain-gage balance was used to obtain force and moment data. Figure 2 shows the support system and one of the entry models. The models were sting-supported from the crescent-shaped strut carrier which may be rotated 30 deg in the pitch plane. For this particular test, the angle of attack of the sting varied from -1 to 25 deg. The base pressure was measured with a transducer and a modified slide-wire potentiometer.

IV. TEST PROCEDURE

Pre-test measurements and calibrations were conducted to determine the actual model position under various loads and to obtain deflection constants required for the data reduction.

During the test, an automatic raw-data plotter and typewriter were used to check the variation of the aerodynamic parameters. The flow field was observed through the schlieren system, and frontlighted schlieren photographs and spark-shadowgraph pictures were taken (Fig. 1 and 3).

The effect of sting diameter on the aerodynamic characteristics was studied by installing a tube over the basic 1.1-in.-diam. sting. The two different tubes which were used to simulate different stings were 1.3 and 1.5 in. in outside diameter respectively, as indicated in the run summary (Table 1).

The data were recorded on tape and typed by an automatic typewriter. Balance readings were plotted vs angle of attack, and any data which appeared questionable were checked before the conclusion of the run. The test program as conducted appears in Table 1.

Table 1. Run summary

Date (1962)	Run No.	Model	Diam. (in.)	Mach No.	Tunnel Supply Pressure (cm Hg, abs.)	Sting Diam. (in.)	Comments
1-30	1	Entry Shape	3.5	—	—	1.1	Static tare
↓	2	↓	3.0	↓	↓	↓	Static tare
	3	↓	2.5				Static tare
1-31	4	↓	2.5	1.65	115		Wake somewhat unsteady at $\alpha = -1$ to 5°
↓	5	↓	3.0	↓	75		Wake somewhat unsteady at $\alpha = -1$ to 6°
	6	↓	3.5	↓	50		Steady wake, but divergent
	7	↓	3.5	1.40	60		Could not establish supersonic flow (model blockage)
	8	↓	3.0	↓	90		Could not establish supersonic flow until model was pitched to $\alpha = 5^\circ$
	9	↓	2.5		100		Divergent wake
	10	Sphere	2.5		120		Unsteady wake, especially at $\alpha = 0^\circ$
	11	↓	3.0		100		Unsteady wake
	12	↓	3.5		↓	↓	Divergent wake; data unrepeatable
	13	↓	3.0		↓	1.3	Divergent wake
	14	Entry Shape	3.0	↓	90	1.3	Divergent wake
2-2	15	↓	3.5	1.81	64	1.1	Well-defined wake but unsteady from $\alpha = -1$ to 1°
↓	16	↓	3.0	↓	↓	↓	Wake unsteady from $\alpha = -1$ to 2°
	17	↓	2.5			↓	Steady well-defined wake
	18	↓	2.5			1.5	Steady wake, but large sting affects it significantly
	19	↓	3.0			↓	Steady wake
	20	↓	3.5			↓	Wake unsteady at $\alpha = -1$ to 2°
	21	Sphere	3.5			1.1	Wake unsteady at $\alpha = -1$ to 1°
	22	↓	3.0		↓		Steady wake
	23	↓	2.5	↓	↓	↓	Steady wake
	24	Entry Shape	2.5	1.65	75		Wake unsteady at $\alpha = -1$ to 1°
↓	25	Entry Shape	3.5	1.65	75	↓	Divergent wake

V. DATA REDUCTION

The aerodynamic coefficients are defined as follows:

Lift-force coefficient $C_L = L/qA$

Normal-force coefficient $C_N = N/qA$

Drag-force coefficient $C_D = D/qA$

Drag-force coefficient
(including base-drag correction)... $C_{Dc} = D_c/qA$

Pitching-moment coefficient $C_m = M_p/qAd$

This term was then subtracted from the chord force in the following manner:

$$C_c = C - (P - P_b) A_b$$

where

A_b = model base area (in.²)

C_b = base-drag correction term (lb)

C_c = chord force (including base-drag correction), (lb)

C = total chord force (lb)

P = free-stream static pressure (psia)

P_b = model base pressure (psia)

The force and moment data were plotted, using body axes for C_N , C_m , and using tunnel wind axes for C_D and C_{Dc} . The sphere pitching-moment data were reduced about the center of gravity, and the entry-model data were reduced about the most forward point on the model. A base-drag correction term was included only in the entry model data and was of the form:

$$C_b = (P - P_b) A_b$$

VI. CONCLUSIONS

The experimental determination of the maximum-size models was based primarily on data which represented the normal-force, drag-force, and pitching-moment coefficients (Plots 1 through 88). Since three models of each configuration (entry shape and sphere) were tested, it was possible to compare the aerodynamic data obtained. In this manner, model-size limitations could be determined by comparing the data from the small models with data from the larger models at the same tunnel conditions.

In the case of the spheres, the normal-force coefficient values for the 3.0 and 3.5-in.-diam. models were different at Mach No. 1.40 and zero angle of attack. Inspection of the schlieren pictures indicated that the shock-wave reflections significantly affect the wake shape which, in turn, can directly affect the characteristics of the model. For the low Mach numbers where the near wake is sub-

sonic, any asymmetrical shock-wave reflections in the subsonic portion of the wake can, indeed, produce lift even when the model is at zero angle of attack. This is undoubtedly what occurred in the case where the spheres were tested at Mach No. 1.40 (see Plot 5).

The 3.5-in. sphere at Mach No. 1.40 shows an example of a divergent wake with no visible evidence of convergence in any portion of the wake. After analyzing the photographs, one could see that the effect of the bow-shock reflections is realized at 1.3 diameters downstream of the model base. These reflections were unsteady, and the pressure fluctuations transmitted through the wake produced unsteady and unrepeatable base pressures and normal-force coefficients. In contrast, the normal-force coefficient for the three sphere diameters of 2.5, 3.0, and 3.5 in. at Mach No. 1.80 was virtually the same. Moreover, the P_b/P ratio was constant for all three sizes of spheres.

The data indicate that the model sizes are not critical for Mach No. 1.81, as was the case for Mach No. 1.40. Figure 4 presents sphere drag-force coefficient and P_b/P ratio data, as a function of Mach number from various facilities.

The entry shape on the other hand, showed a relatively constant normal-force coefficient throughout the Mach range, with the exception of Mach No. 1.40. At this Mach number, supersonic flow could not be fully established with either the 3.0 or 3.5-in.-diam. model (with the 1.1-in.-diam. sting) at an angle of attack of 0 deg. However, when the 3.0-in. model was pitched to approximately 5 deg, supersonic flow was fully established (see Fig. 5).

This points out the fact that not only the model, support size, and shape are important in blockage, but also that the model attitude is important in the test section.

Presently, some blocking data are available for spheres, hemisphere-cylinders, and discs with their axis of symmetry parallel to the air flow. From this information, it is possible to predict the blocking characteristics of these models (Ref. 1, 3, and 4) and perhaps apply the same data to the entry shape. However, even if the blocking limits could be determined with a reasonable amount of accuracy, this would not guarantee the validity of the aerodynamic data. This fact was illustrated in the case of the

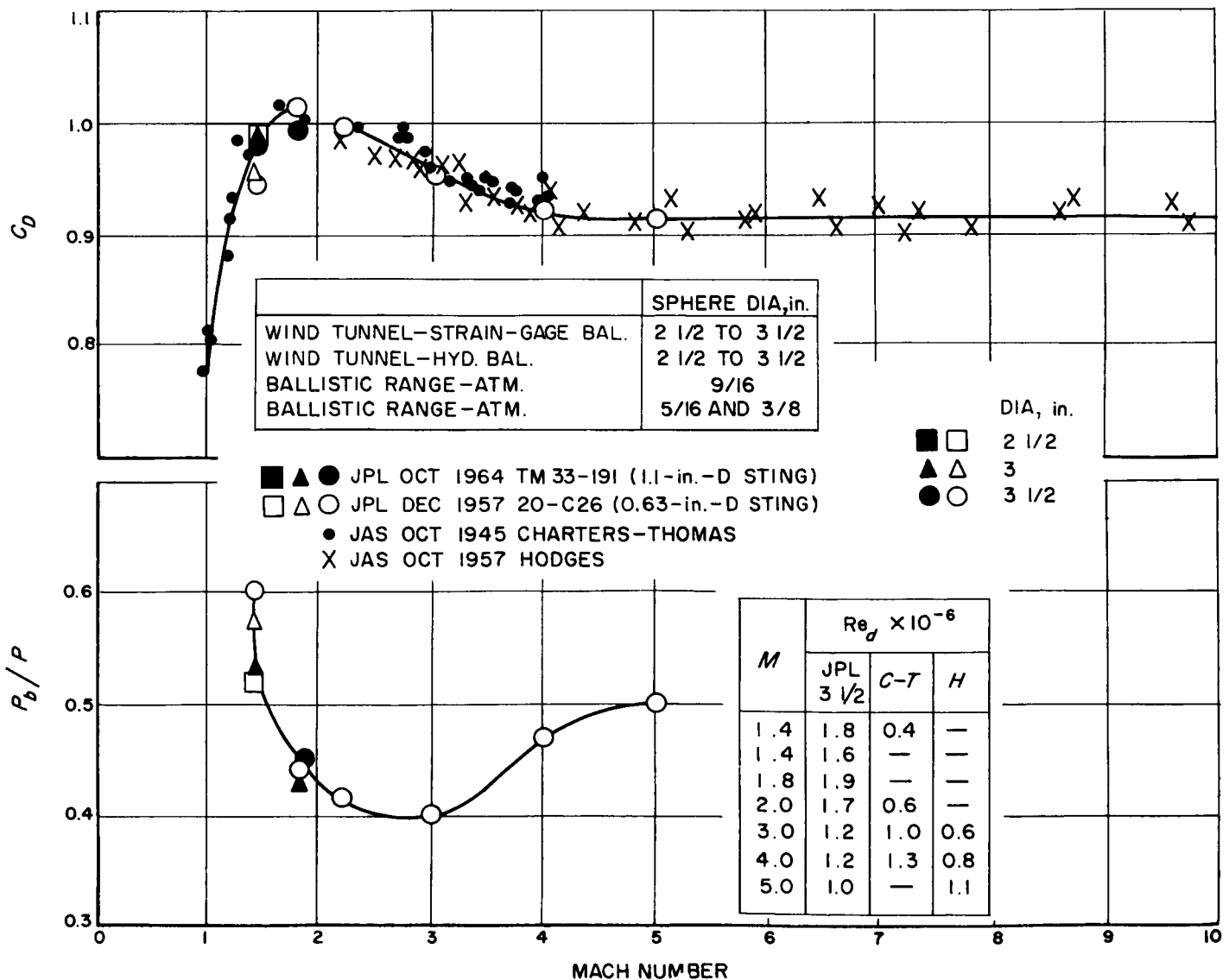
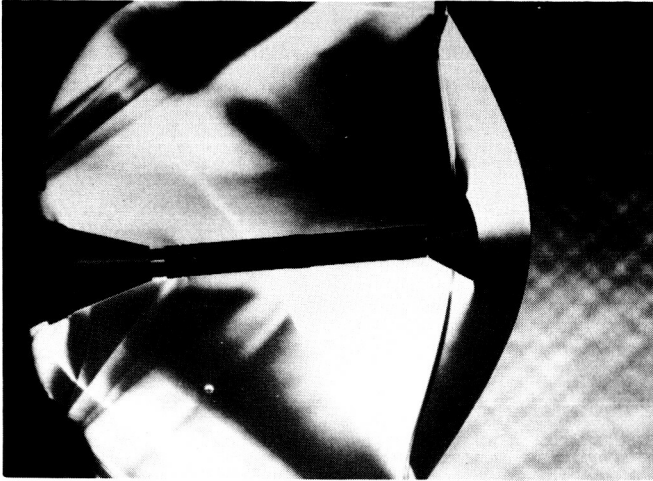


Fig. 4. Sphere drag-force coefficient and base free-stream static-pressure ratio as a function of Mach number

FLOW ESTABLISHED
 $\alpha = 5 \text{ deg}$



TUNNEL BLOCKED
 $\alpha = 0 \text{ deg}$

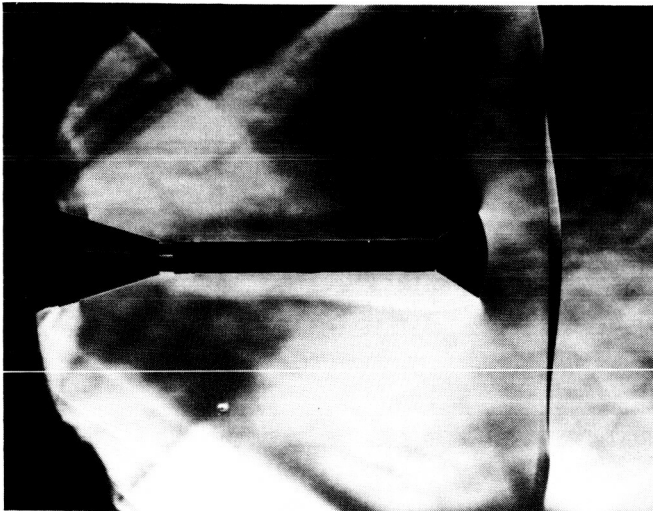


Fig. 5. Schlieren photograph of 3.0-in.-diam. entry shape on a 1.1-in.-diam. sting with supersonic flow established and with tunnel blocked, Mach No. 1.40

3.5-in.-diam. sphere at Mach No. 1.40 where, although supersonic flow was fully established, some of the data were not repeatable (see Plot 8). Therefore, in order to determine properly the allowable maximum-size model for a specific Mach number, it is necessary that this be done experimentally. The pitching-moment coefficient, however, for each entry model in this test remained constant throughout the Mach-number range.

For all the entry models, as was the case for the spheres, the P_b/P ratio decreased as the Mach number increased. However, one should bear in mind that this relationship

was affected by the position of the bow shock reflected from the tunnel boundaries and did not represent the true variation which would exist if the boundaries were not present (see Fig. 6). The position of the reflected bow wave was determined mainly by the model size relative to the test-section dimensions. In other applications, it is possible to locate the model well upstream of the wave, and thus minimize its disturbance.

The variation in sting diameter affected the sphere data more than the entry-model data under the same tunnel conditions. In particular, at Mach No. 1.40 the components most affected were the drag coefficient and P_b/P ratio. The effect of sting interference on aerodynamic data has been realized for some time. However, the problem has been the application of the proper correction to the data. Presently, enough data are available which indicate that for moderately slender bodies of revolution in supersonic flow, the base pressure may decrease as the sting diameter is reduced. For these *blunt* models, however, the trend was in the opposite direction. The sting-interference data were insufficient in this test to make any concrete statements comparing blunt bodies with slender ones. The trends that were found in this test, however, were consistent for the Mach numbers investigated.

The following conclusions were based on the information obtained in the determination of the maximum model size. The conclusions were also based on test conditions indicated in the run summary (Table 1). Plots 1 through

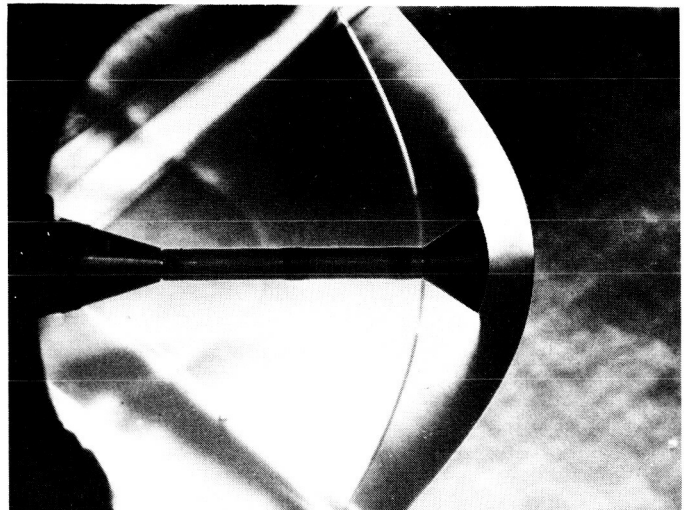


Fig. 6. Schlieren photograph of 3.5-in.-diam. entry shape showing bow wave due to presence of the tunnel boundaries

88 contain all the aerodynamic data used in the analysis. The conclusions of this test program are:

Entry Shape:

1. With the 3.5-in.-diam. model installed, supersonic flow could not be established at Mach No. 1.40.
2. The 3.0-in.-diam. model is too large to be tested at Mach No. 1.40. Initially, with the model mounted on the 1.1-in.-diam. sting and at zero angle of attack, the tunnel was partially blocked. As the model attitude was increased to approximately 5 deg, the shock moved downstream to its normal position for this Mach number; thus, the tunnel was fully started (Fig. 5). Once flow was established, it was possible to pitch the model to a maximum of 15 and back to 0 deg, without disturbing flow conditions.
3. At Mach No. 1.40, the 2.5-in.-diam. model is marginal in size; this restricts obtaining reliable aerodynamic data (Plots 18 and 20).
4. At Mach No. 1.65, the 3.5-in.-diam. model is large, and therefore testing at this Mach number should be avoided (see Plots 22 and 24).
5. The 2.5 and 3.0-in.-diam. entry models can be adequately tested at a minimum Mach No. 1.65 (see Plots 21 through 24). Based on this conclusion, the 3.0-in.-diam. test models were fabricated.
6. Repeatable data can be obtained at Mach No. 1.81 with the 2.5-in.-diam. model.

Sphere:

1. With the 3.5-in.-diam. model, supersonic flow can be established at Mach No. 1.40, but lift-force coefficient and base-pressure data are erratic and unrepeatable (Plots 5 and 8).
2. At Mach No. 1.40, the 2.5 and 3.0-in.-diam. models are also too large and should not be tested. The lift-force coefficient was somewhat irregular as the angle of attack increased.
3. At Mach No. 1.81, the 3.0 and 3.5-in.-diam. models are of the proper size so that repeatable data can be obtained.

Sting Effects (results obtained when sting diameter was varied):

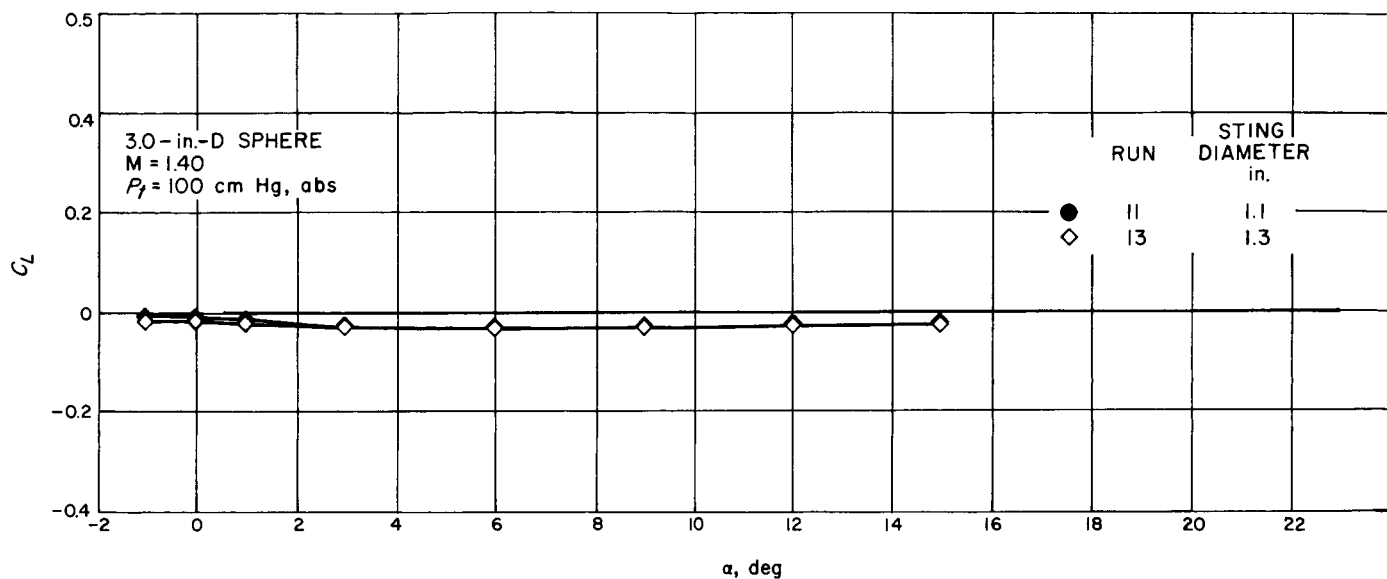
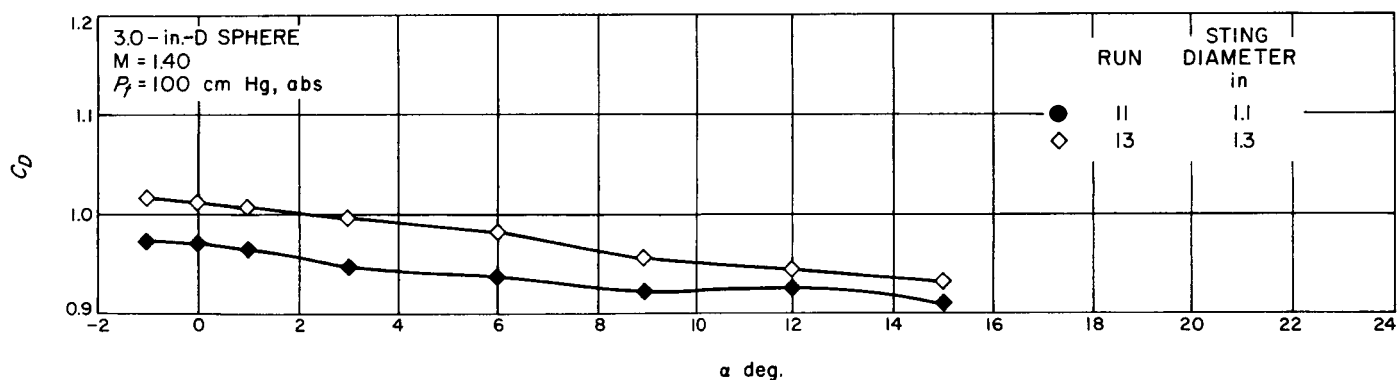
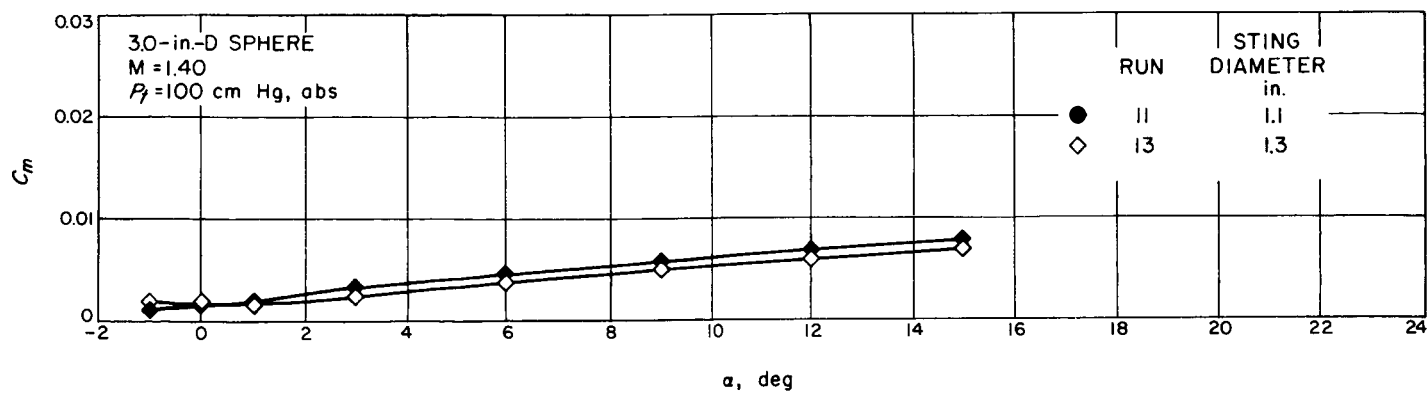
1. At Mach No. 1.40, for the 3.0-in.-diam. sphere an 18% increase in sting diameter decreased the base free-stream static-pressure ratio (P_b/P) by a maximum of 7% and increased the drag-force coefficient (C_D) by as much as 4%. At small angles of attack (1 to 3 deg), an effect on the lift-force coefficient was observed.
2. At Mach No. 1.81, for the three entry shapes tested, a maximum variation was found on the 2.5-in.-diam. model; the 36% increase in sting diameter decreased base free-stream static-pressure ratio by as much as 14% and increased the corrected drag-force coefficient by a maximum of 3.4% (for $\alpha < 15$ deg), see Plots 30 and 40. No detectable effect could be found on the normal-force coefficient.

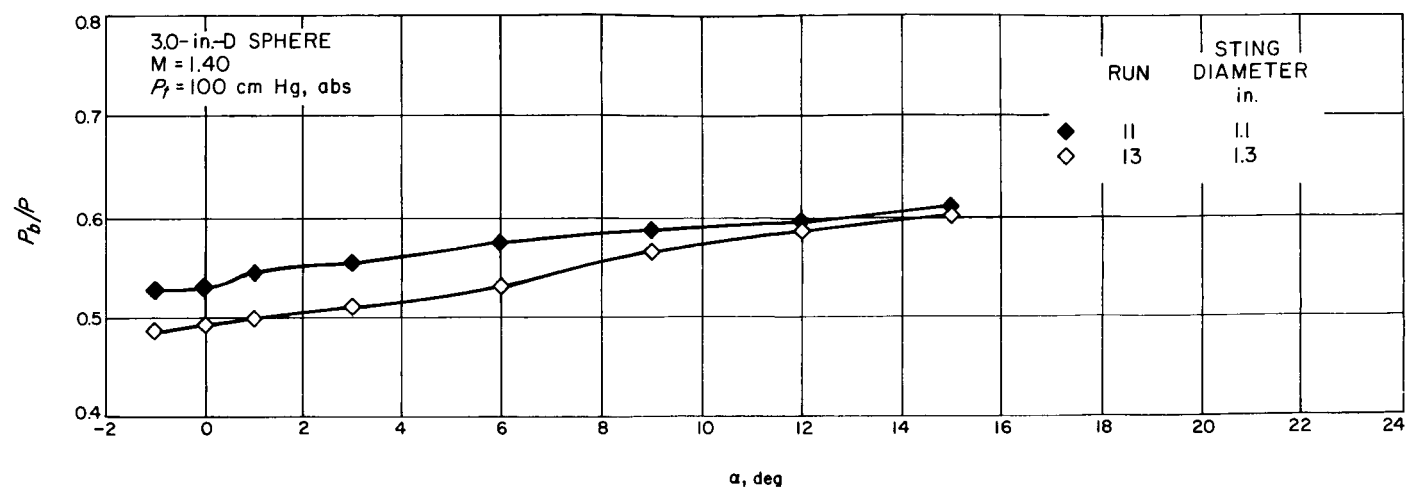
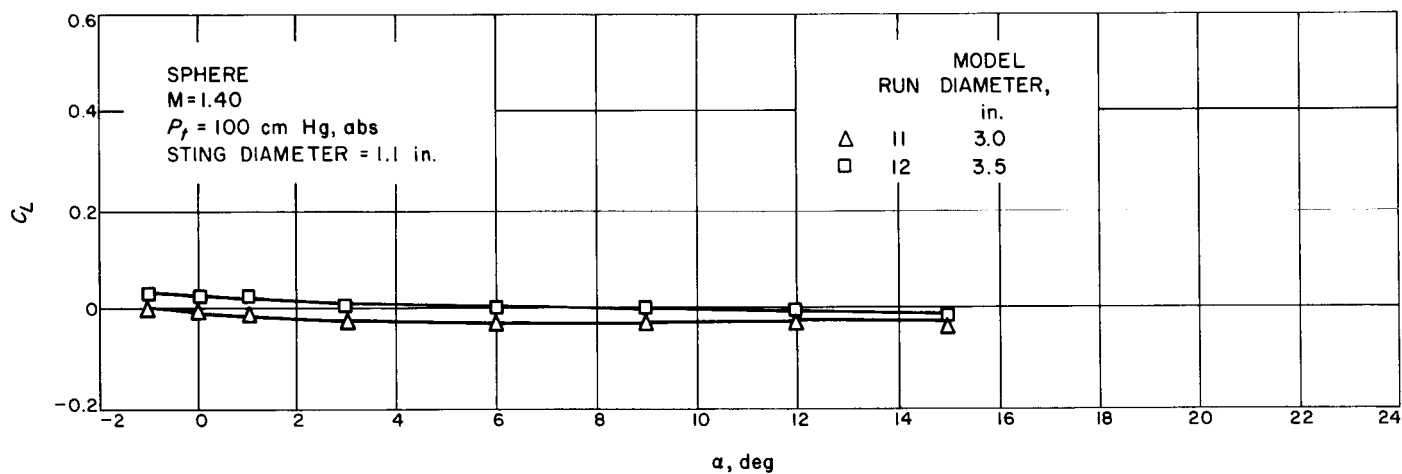
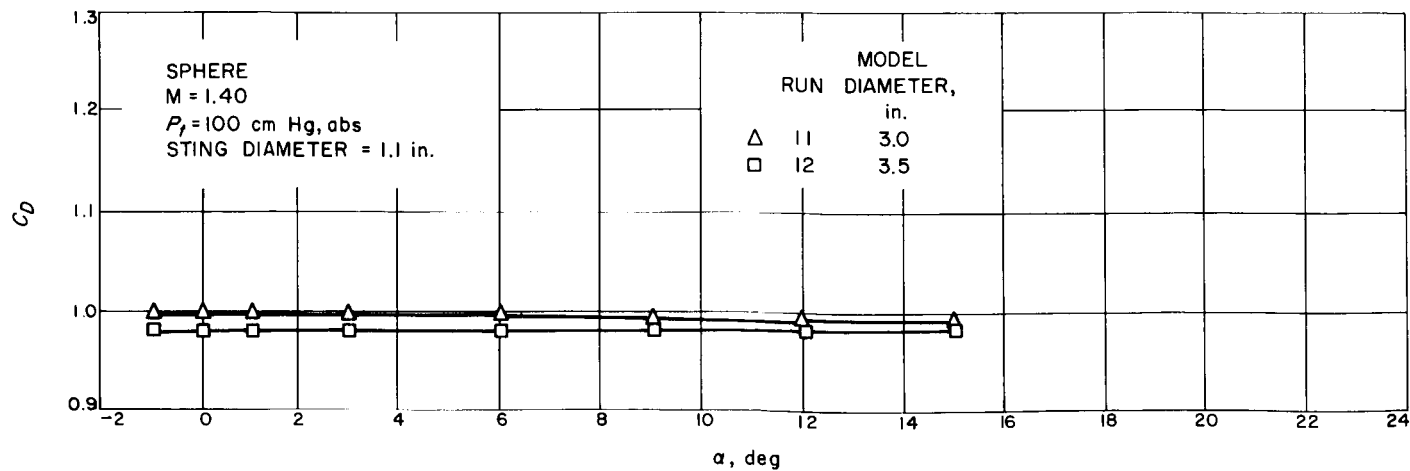
NOMENCLATURE

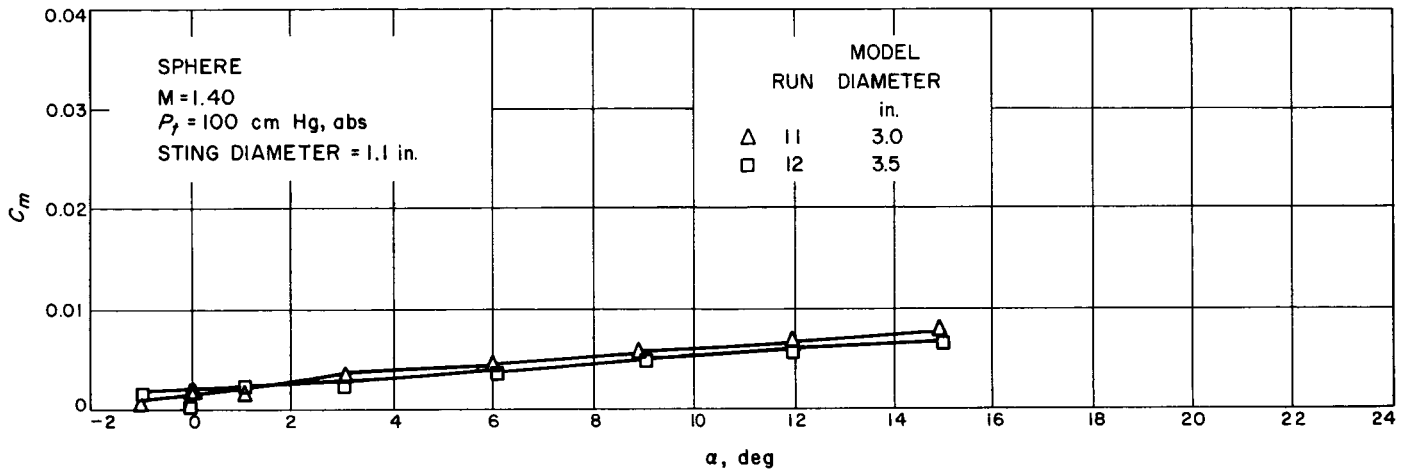
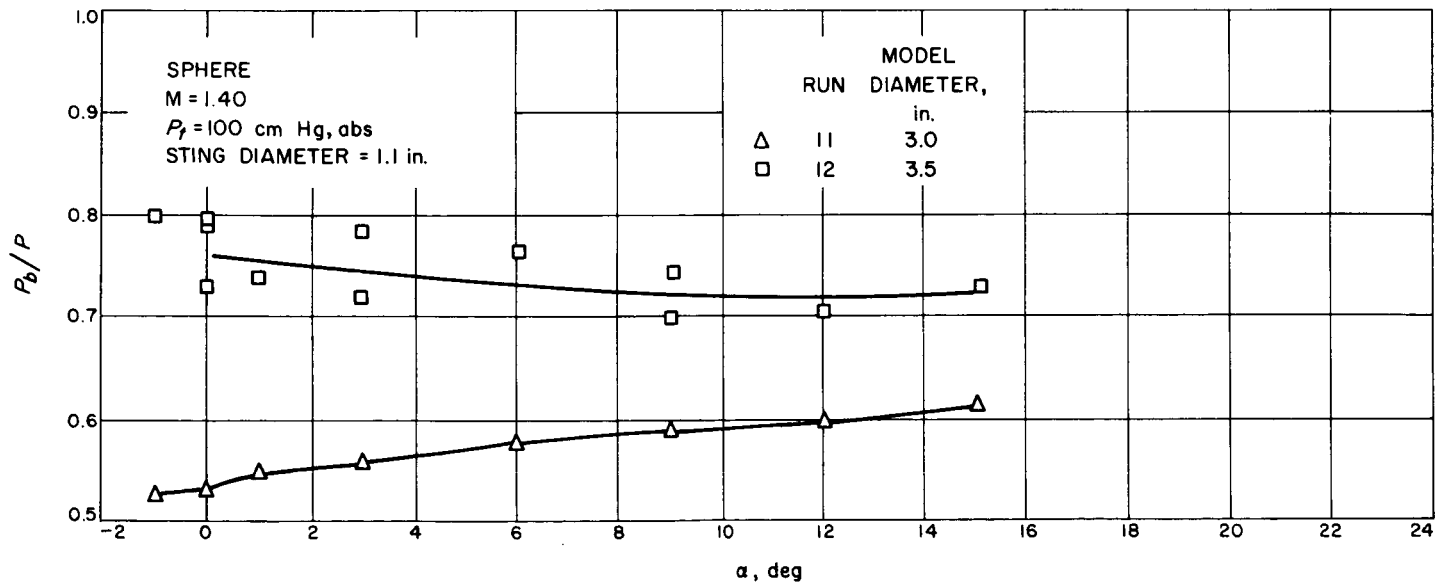
- A = frontal area, when $\alpha = 0$ deg, (in.²)
- $C.P.$ = center of pressure (referenced to center of gravity for the sphere and for the entry shape to the model's most forward point), (in.)
- d = model diameter (in.)
- D = drag force (lb)
- D_c = drag force (including base-drag correction), (lb)
- L = lift force (lb)
- M = Mach number
- M_p = pitching moment (in.-lb)
- N = normal force (lb)
- P_b/P = base free-stream static-pressure ratio
- P_t = tunnel supply pressure (cm Hg, abs.)
- q = free-stream dynamic pressure (psia)
- α = sting angle of attack (deg)

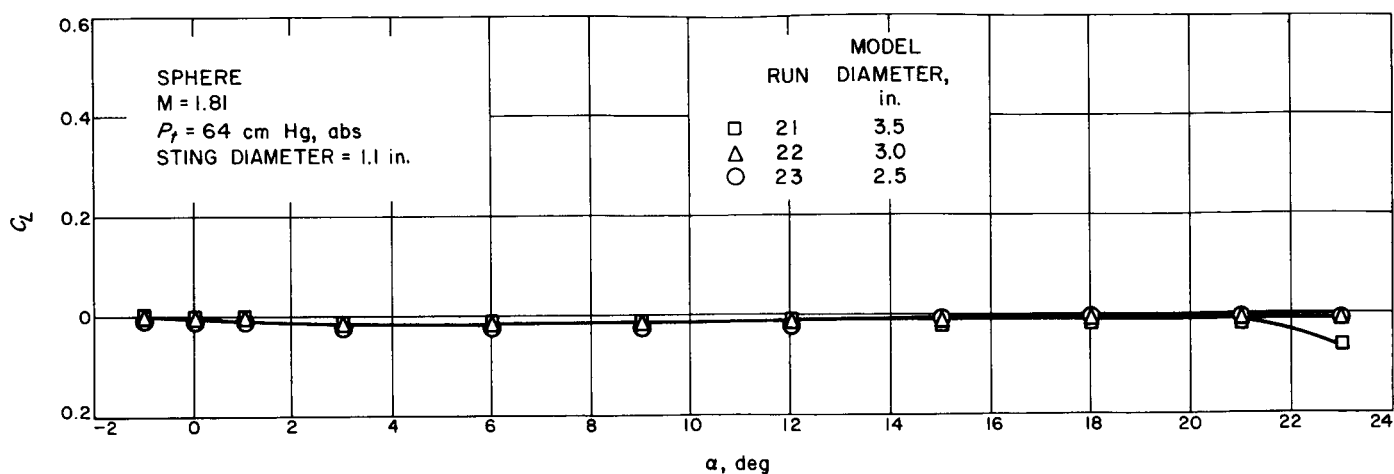
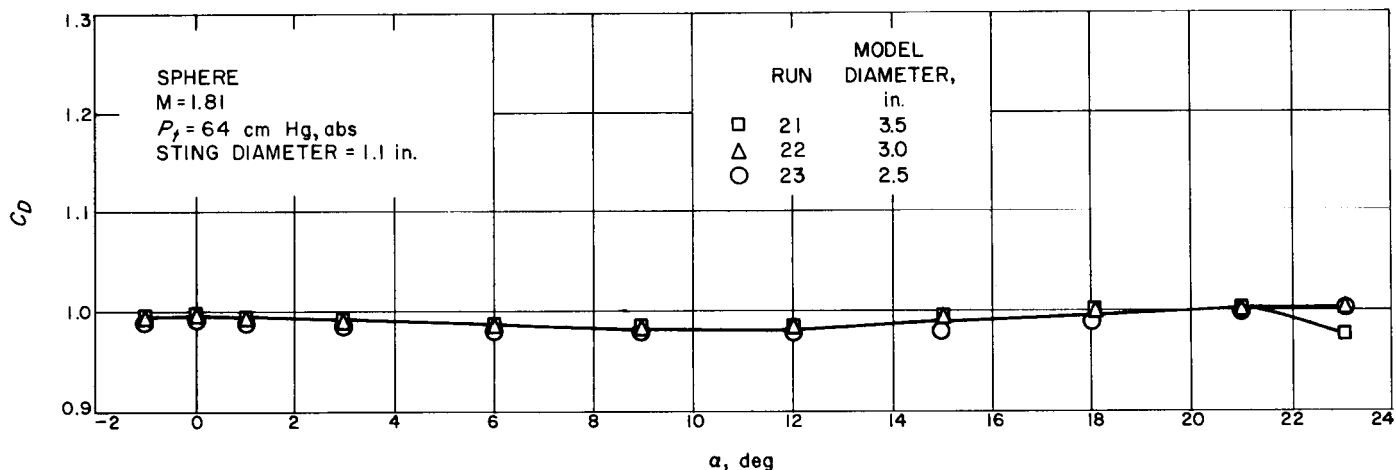
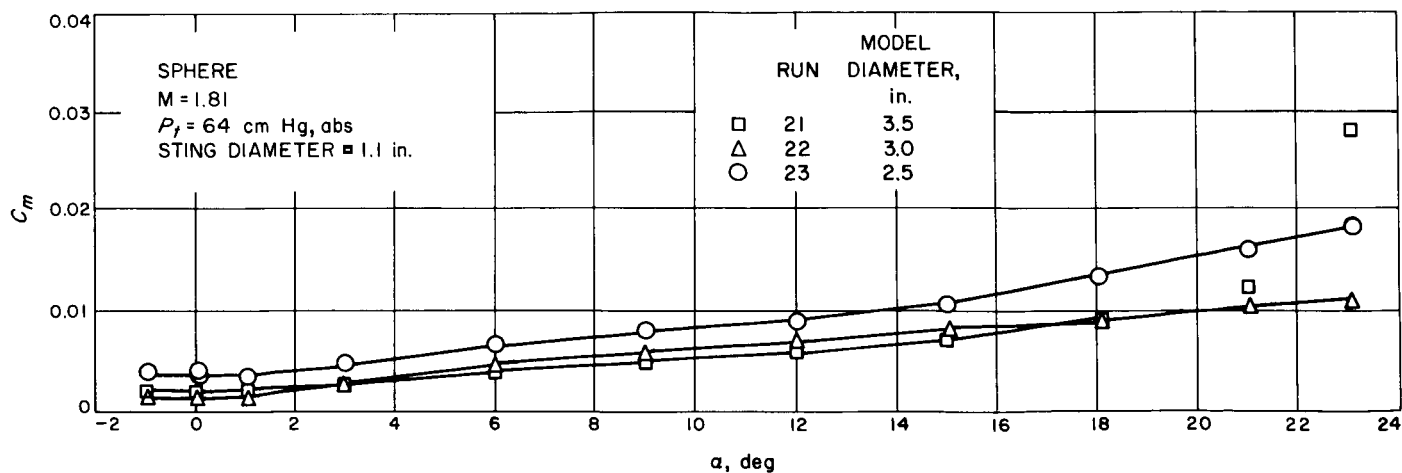
REFERENCES

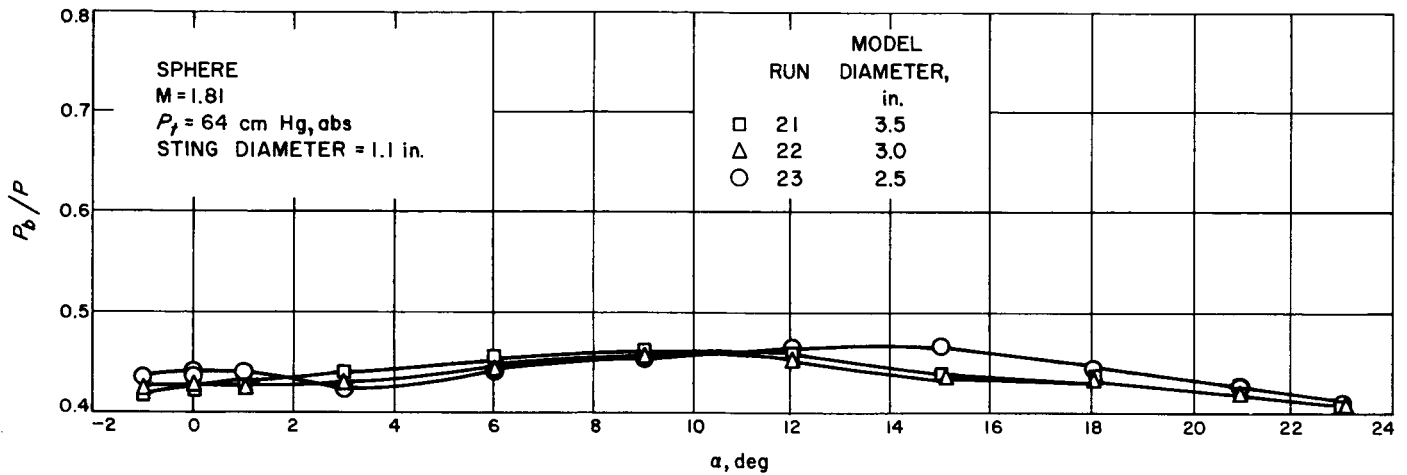
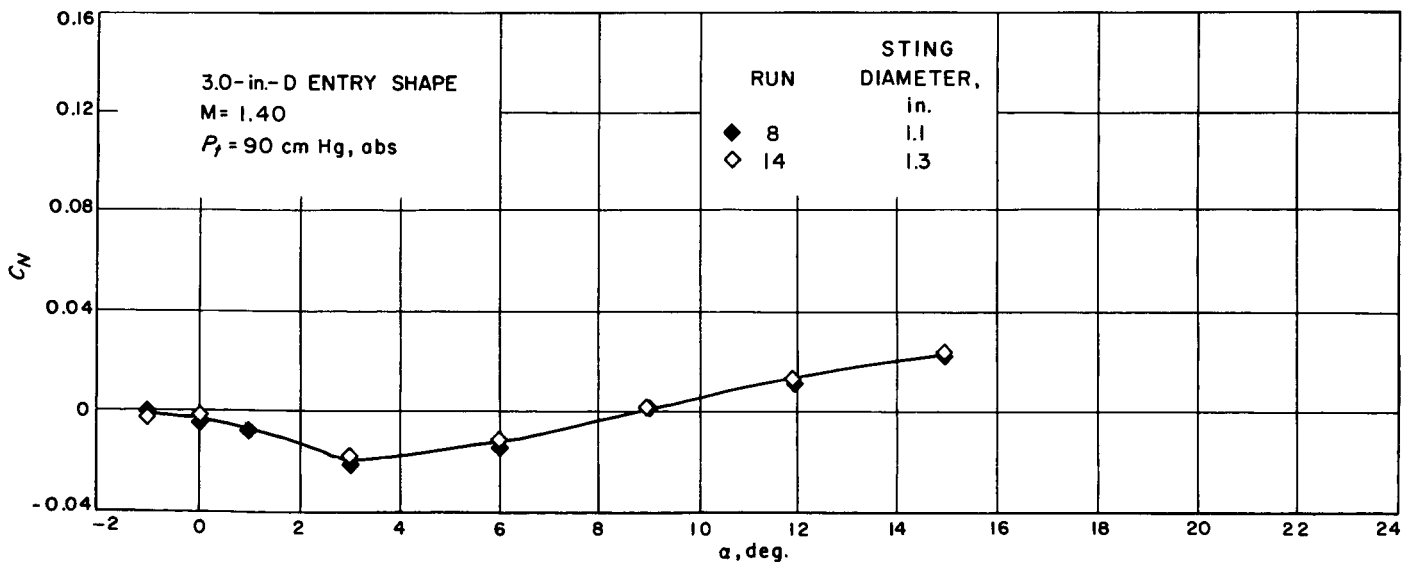
1. Dayman, Jr., Bain, *Prediction of Blocking in the Supersonic Wind Tunnel during an Attempted Start*, External Publication No. 669, Jet Propulsion Laboratory, Pasadena, June 17, 1959.
2. Staff, Wind-Tunnel, *Wind-Tunnel Facilities at the Jet Propulsion Laboratory*, Technical Release No. 34-257, Jet Propulsion Laboratory, Pasadena, January 1, 1962.
3. Dayman, Jr., Bain, *Apparent Sphere Aerodynamics on Sting Support*, Internal Memorandum No. 20-C26, Jet Propulsion Laboratory, Pasadena, December, 1957.
4. Hodges, A. J., "The Drag Coefficient of Very High Velocity Spheres," *Journal of Aeronautical Sciences*, Vol. 24, No. 10, pp. 755-758, October 1957.

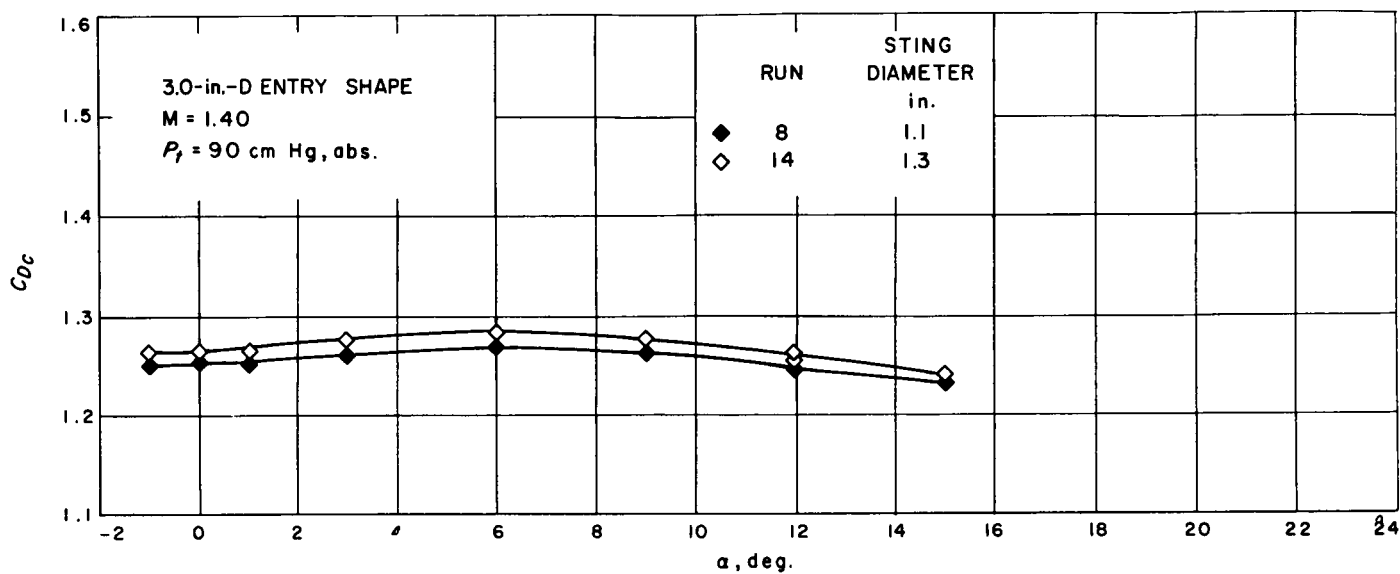
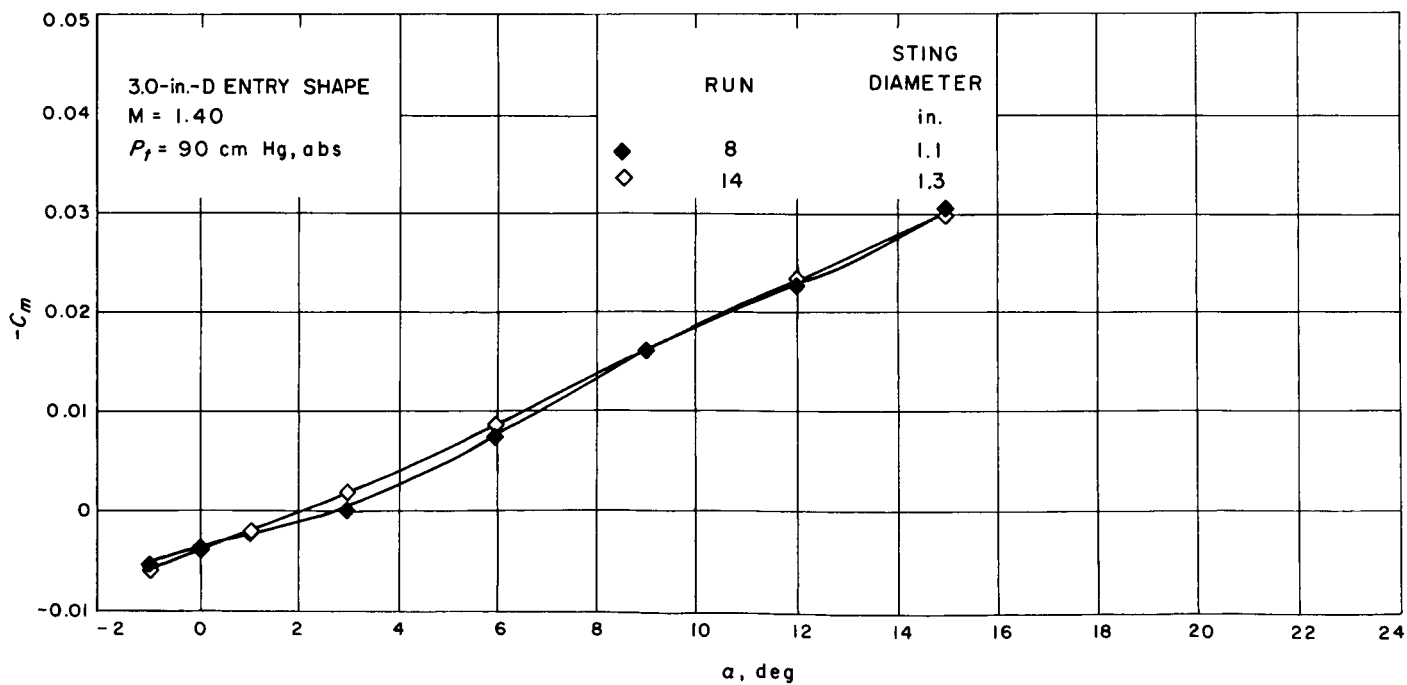
Plot 1. C_L vs α for a spherePlot 2. C_D vs α for a spherePlot 3. C_m vs α for a sphere

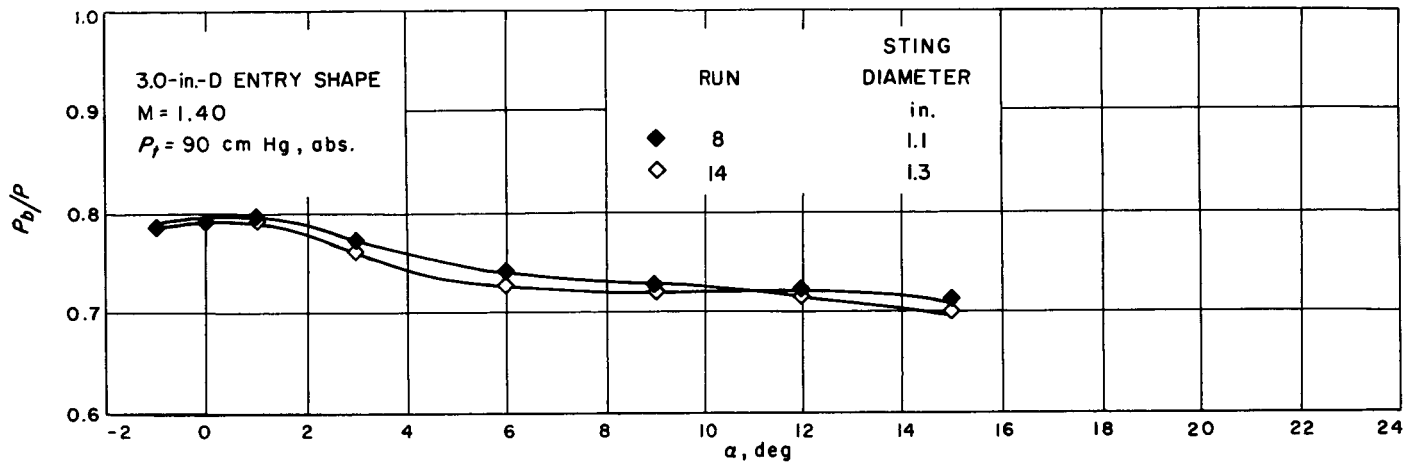
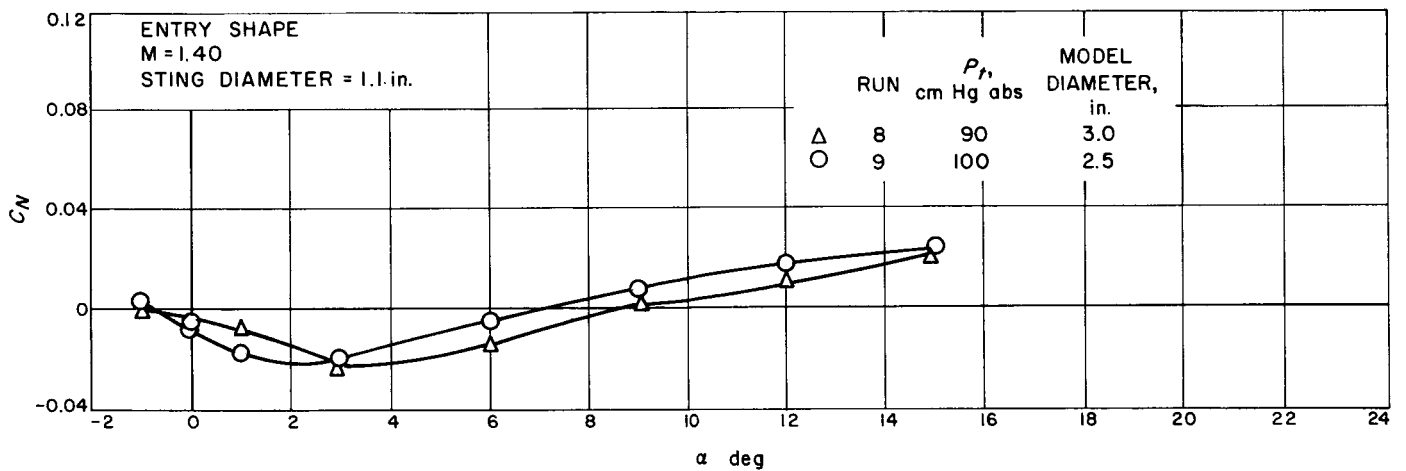
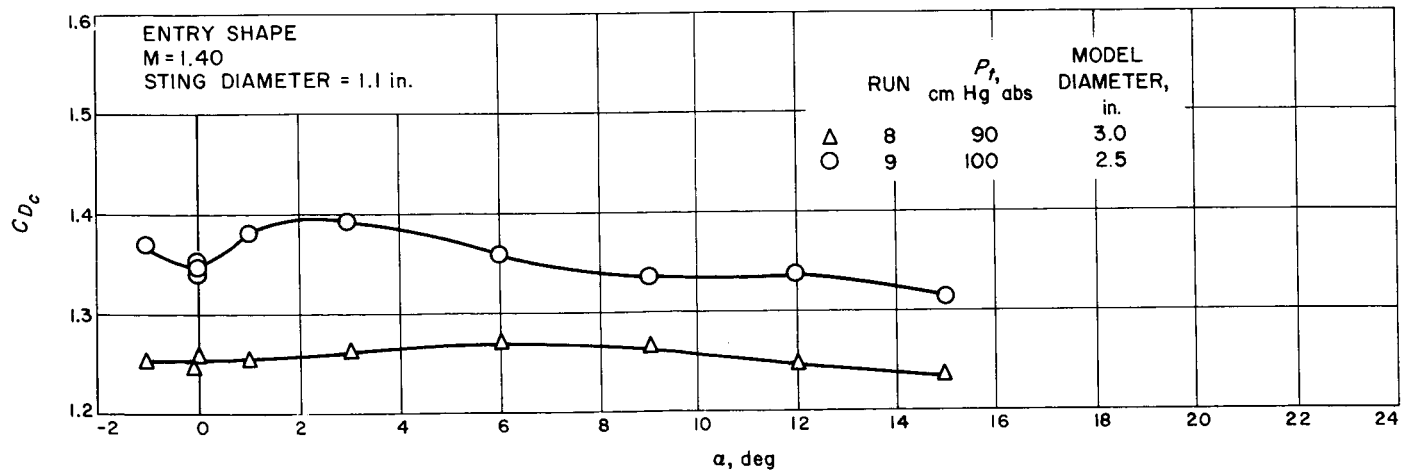
Plot 4. P_b/P vs α for a spherePlot 5. C_L vs α for a spherePlot 6. C_D vs α for a sphere

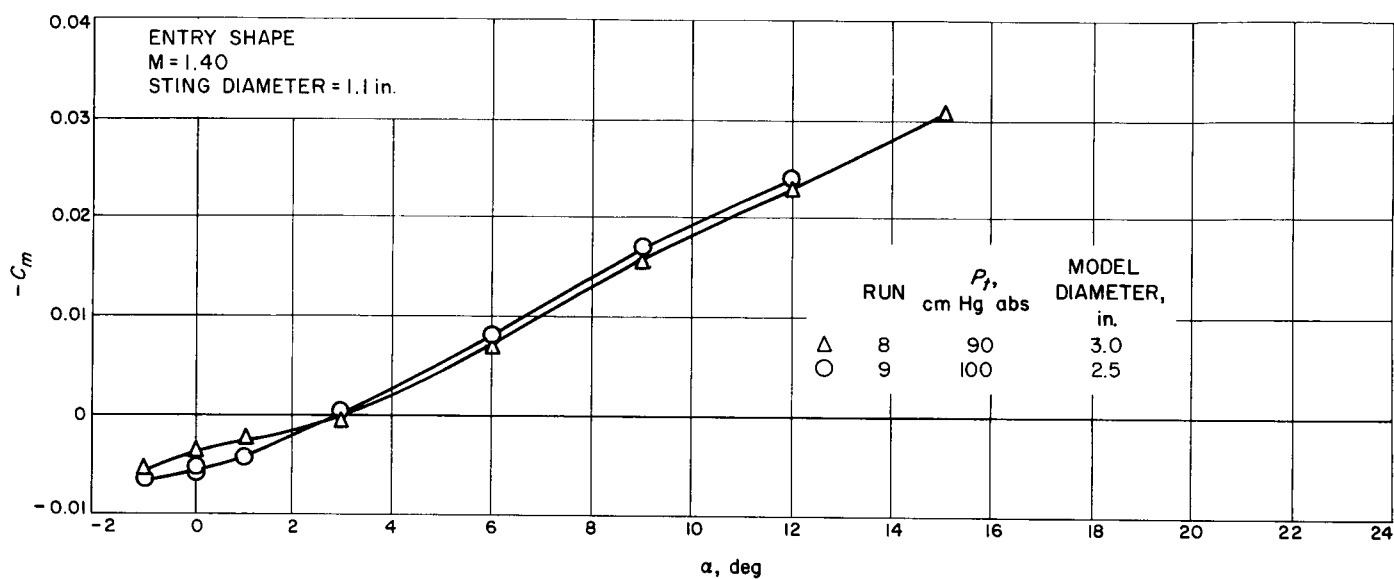
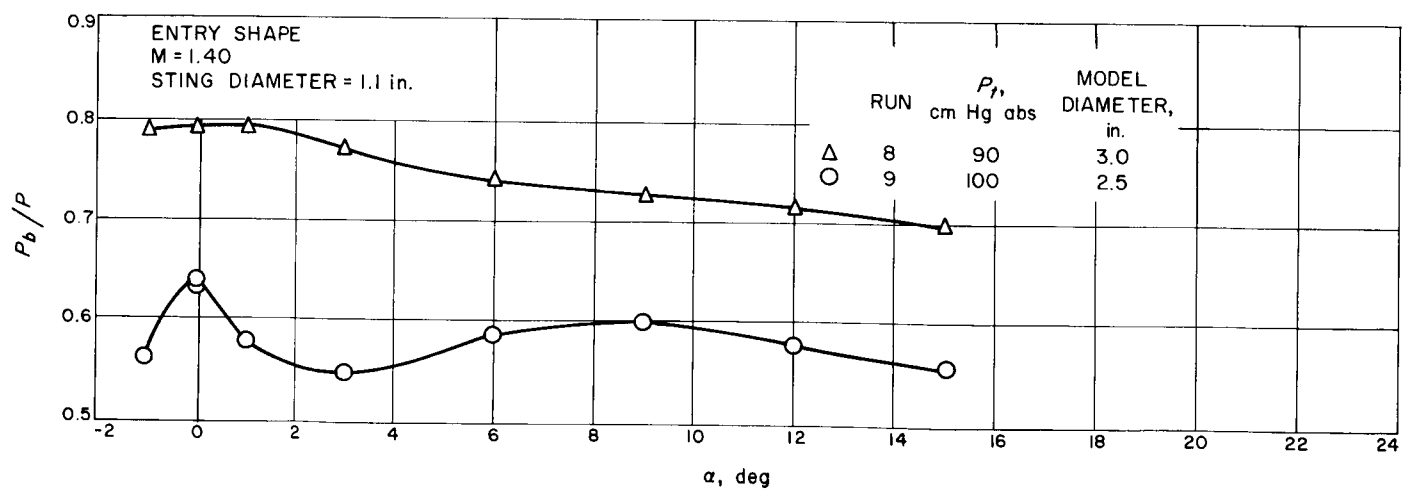
Plot 7. C_m vs α for a spherePlot 8. P_b/P vs α for a sphere

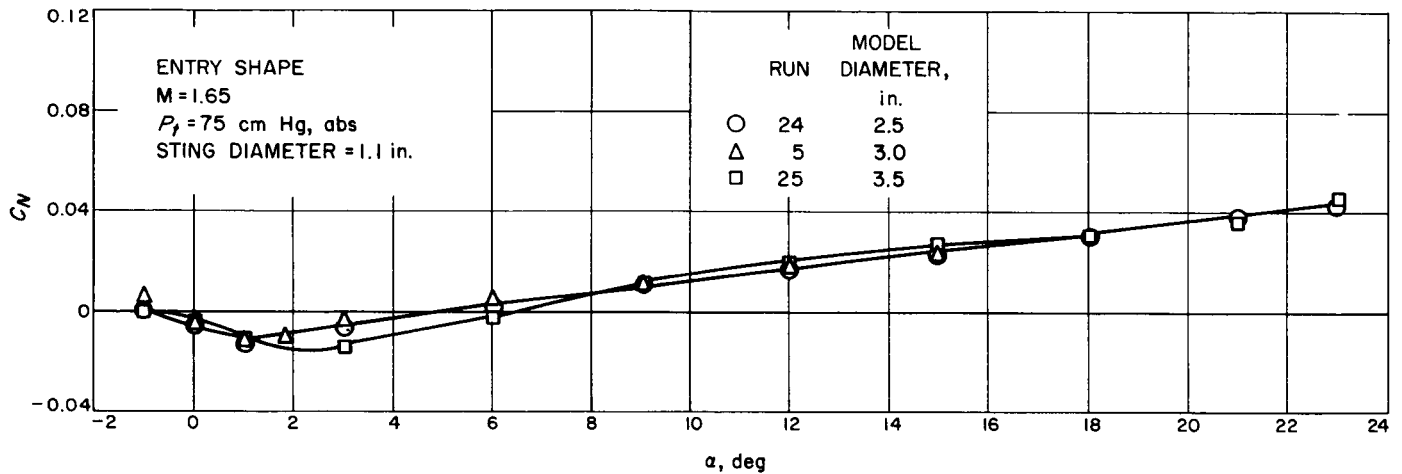
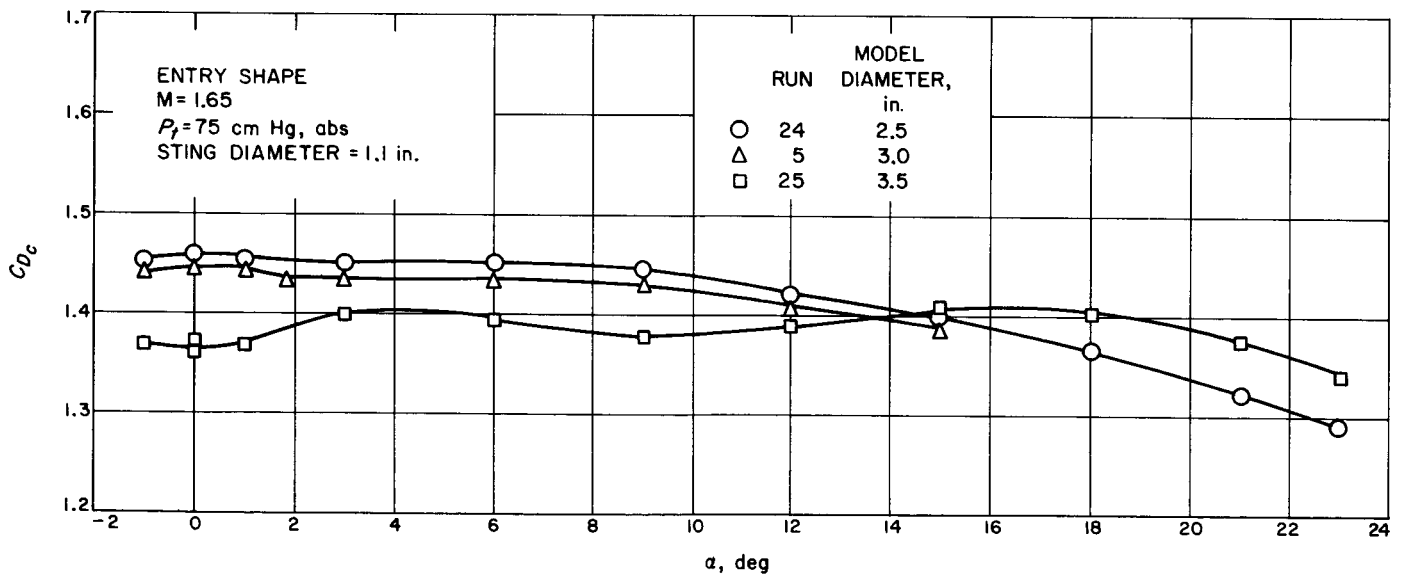
Plot 9. C_L vs α for a spherePlot 10. C_D vs α for a spherePlot 11. C_m vs α for a sphere

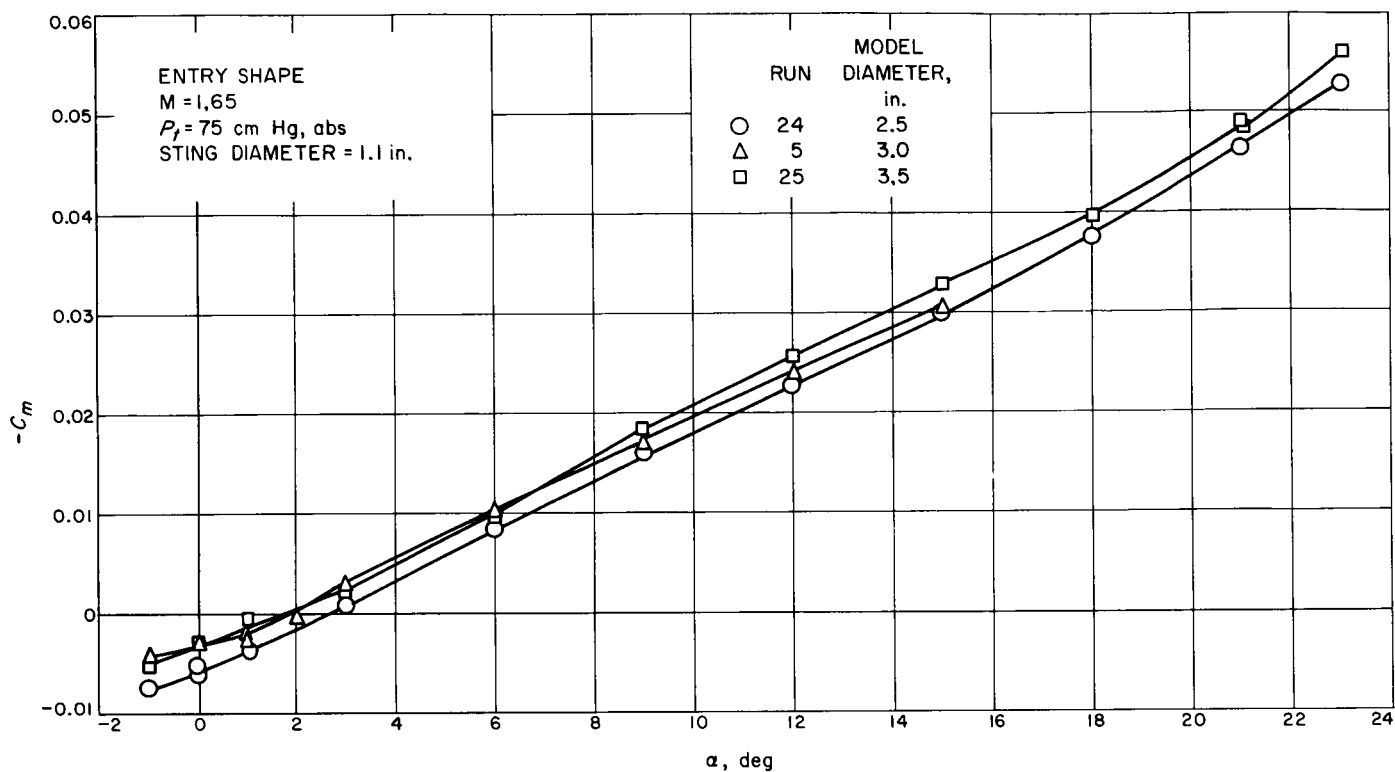
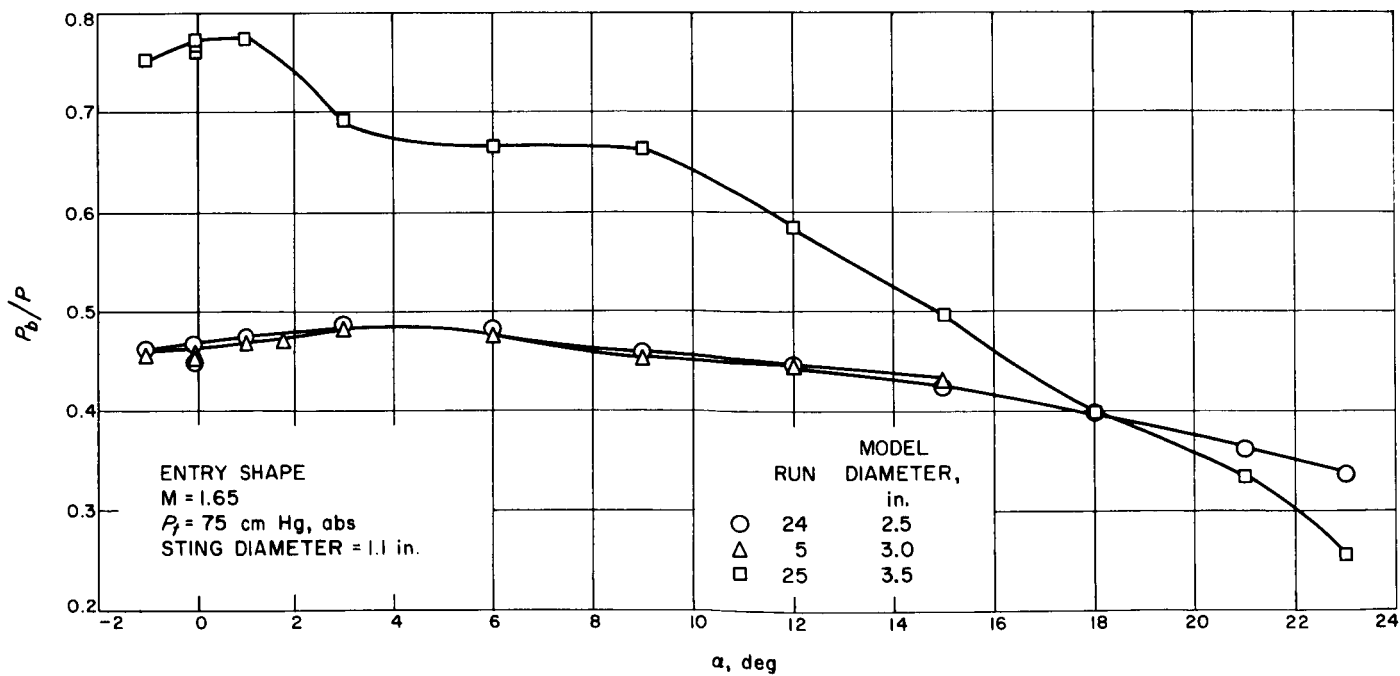
Plot 12. P_b/P vs α for a spherePlot 13. C_N vs α for an entry shape

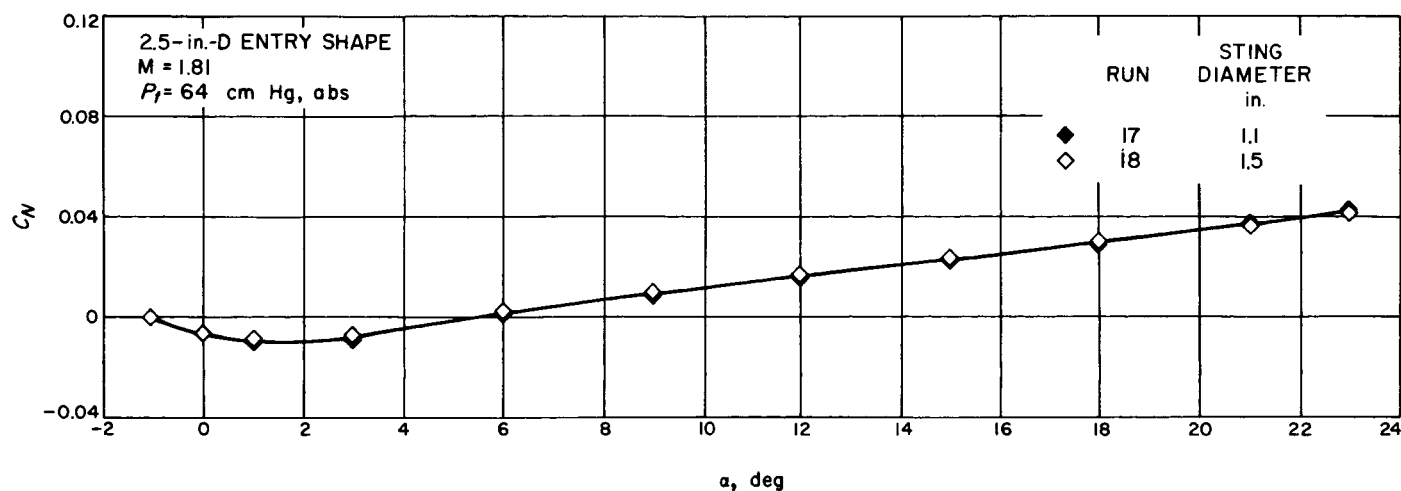
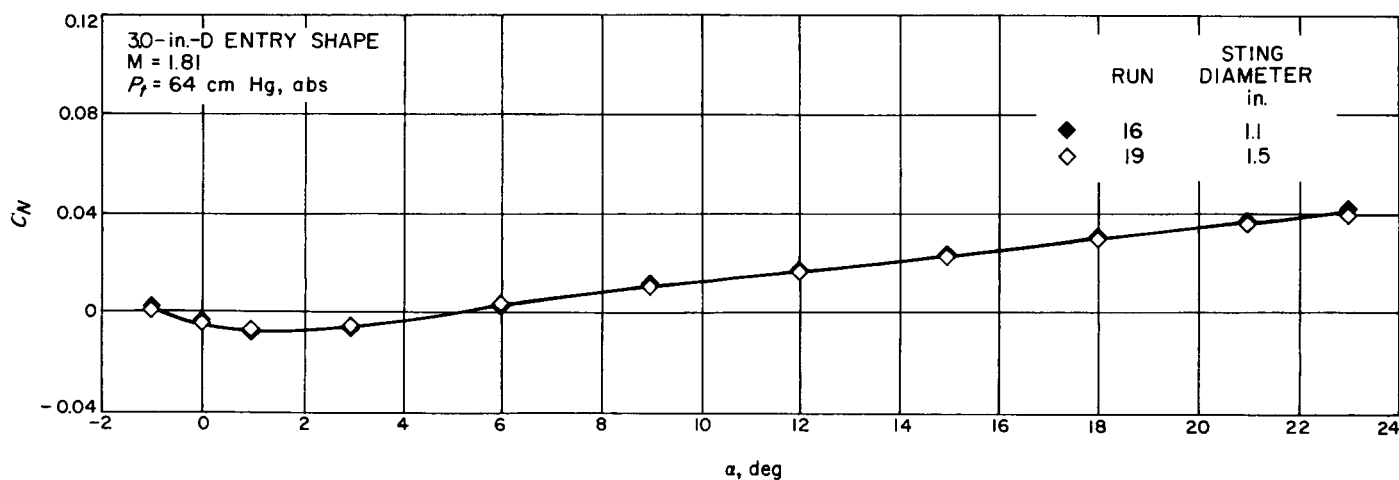
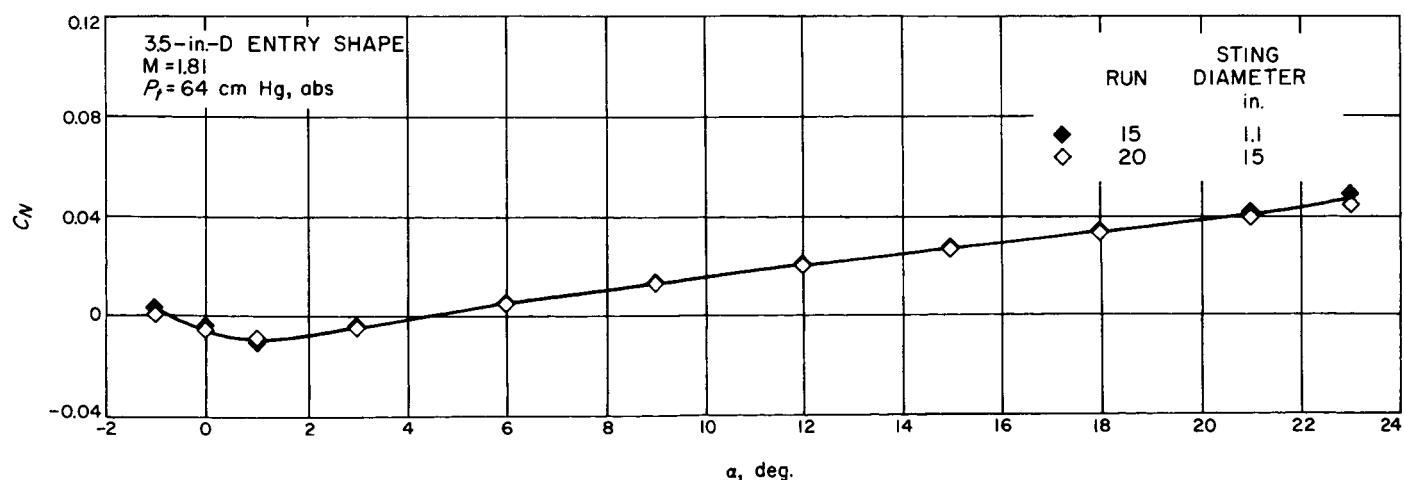
Plot 14. C_{Dc} vs α for an entry shapePlot 15. $-C_m$ vs α for an entry shape

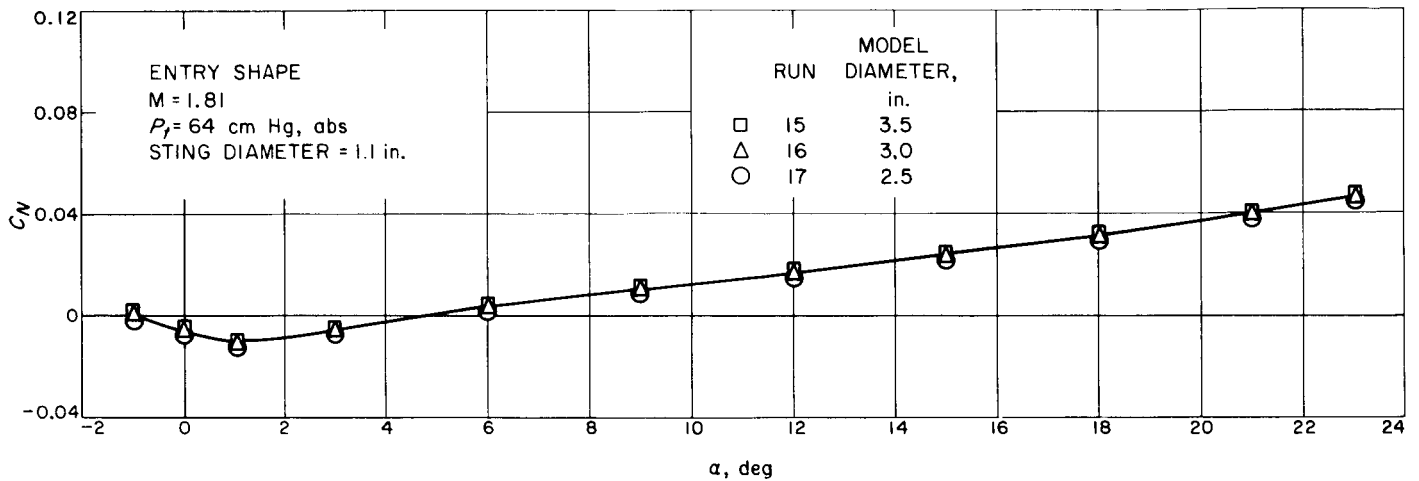
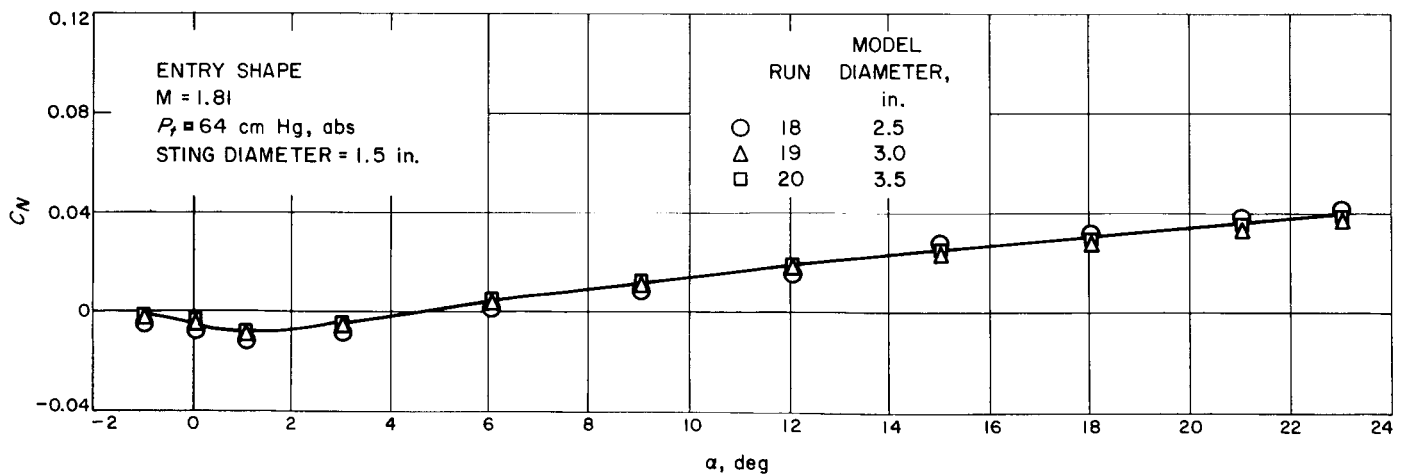
Plot 16. P_b/P vs α for an entry shapePlot 17. C_N vs α for an entry shapePlot 18. C_{Dc} vs α for an entry shape

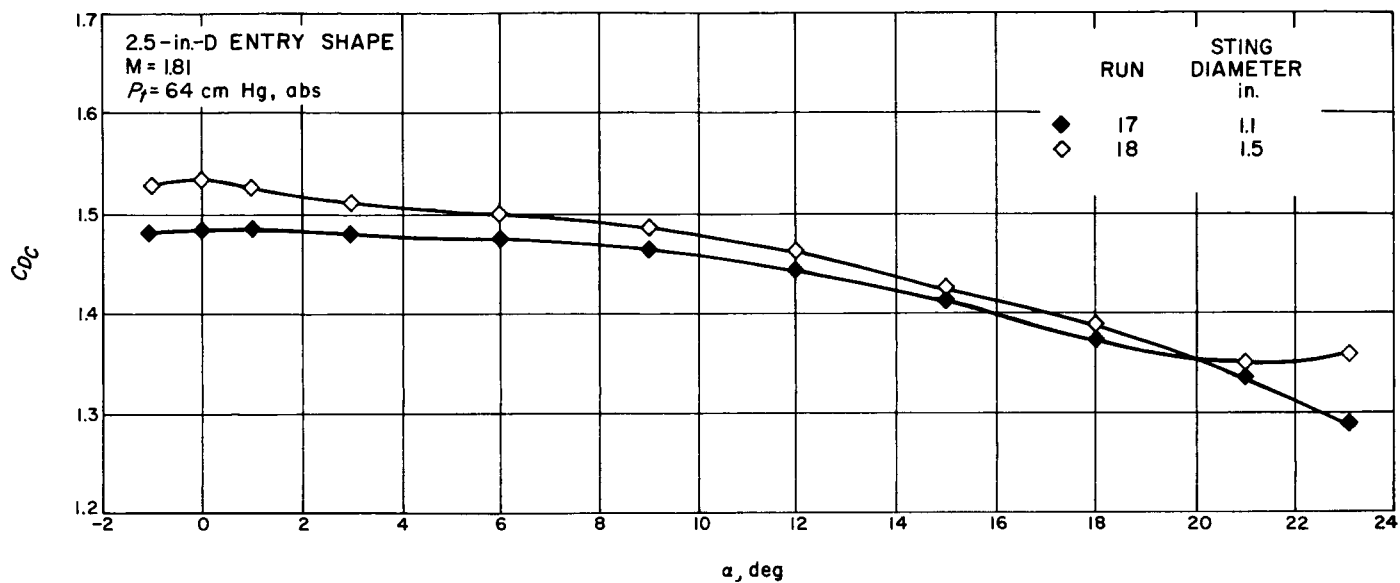
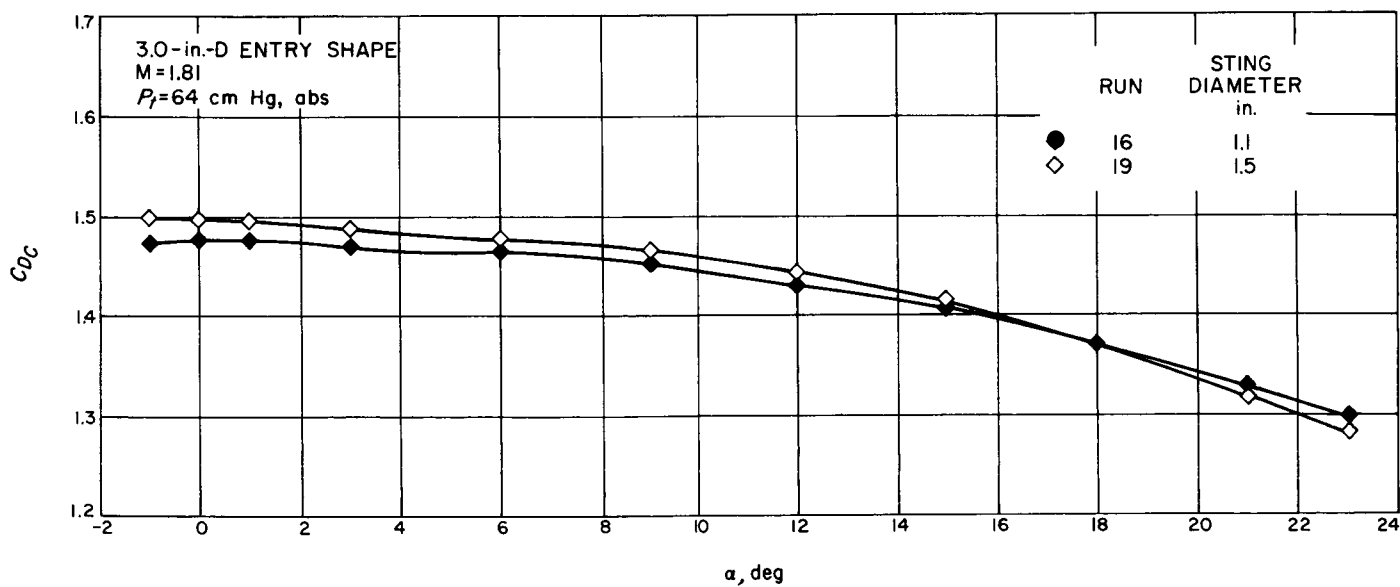
Plot 19. $-C_m$ vs α for an entry shapePlot 20. P_b/P vs α for an entry shape

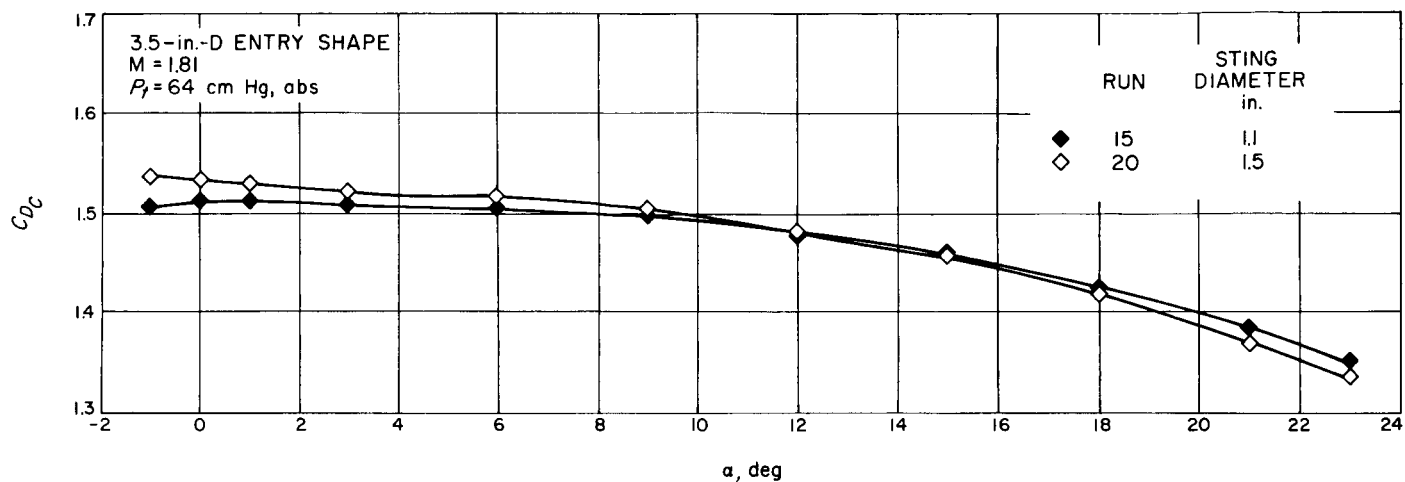
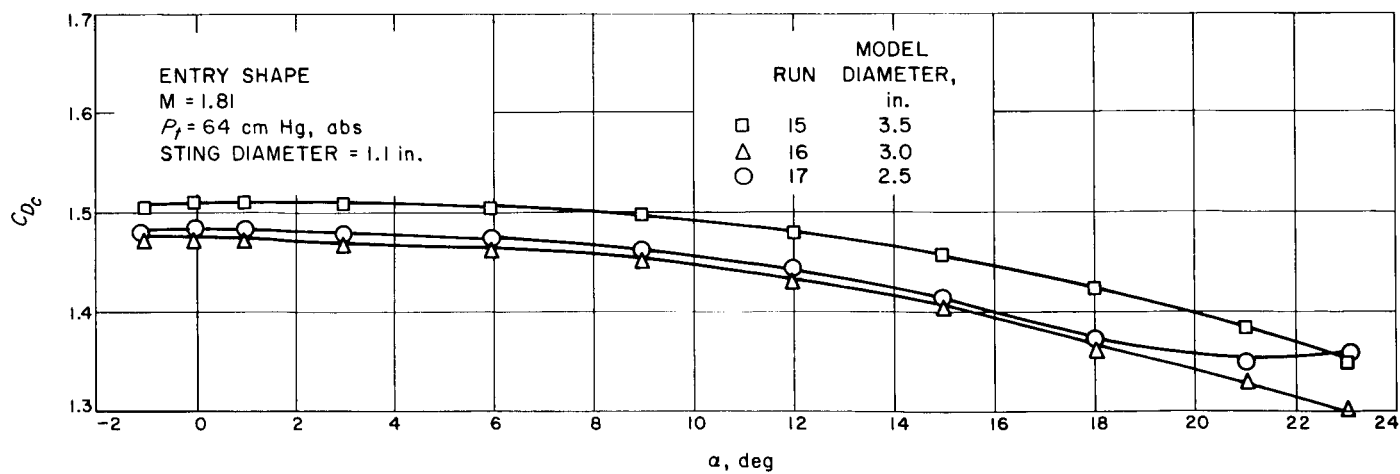
Plot 21. C_N vs α for an entry shapePlot 22. C_{Dc} vs α for an entry shape

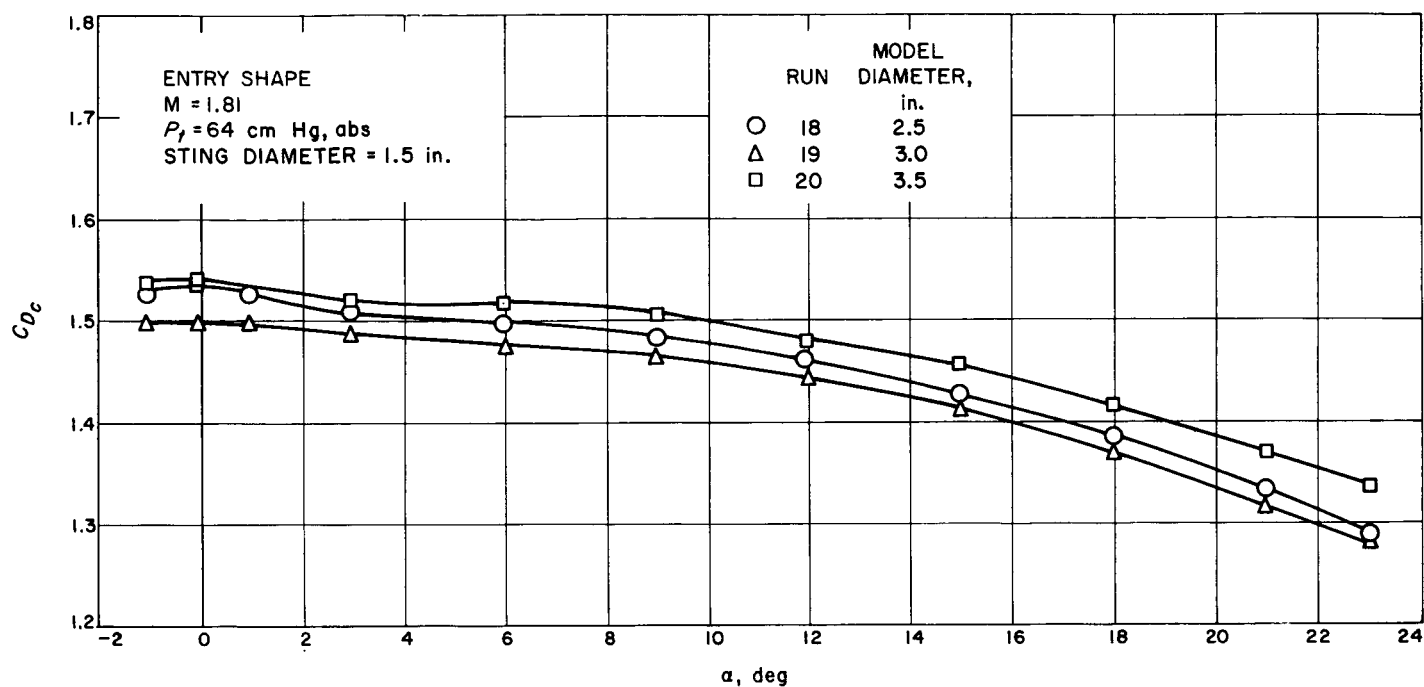
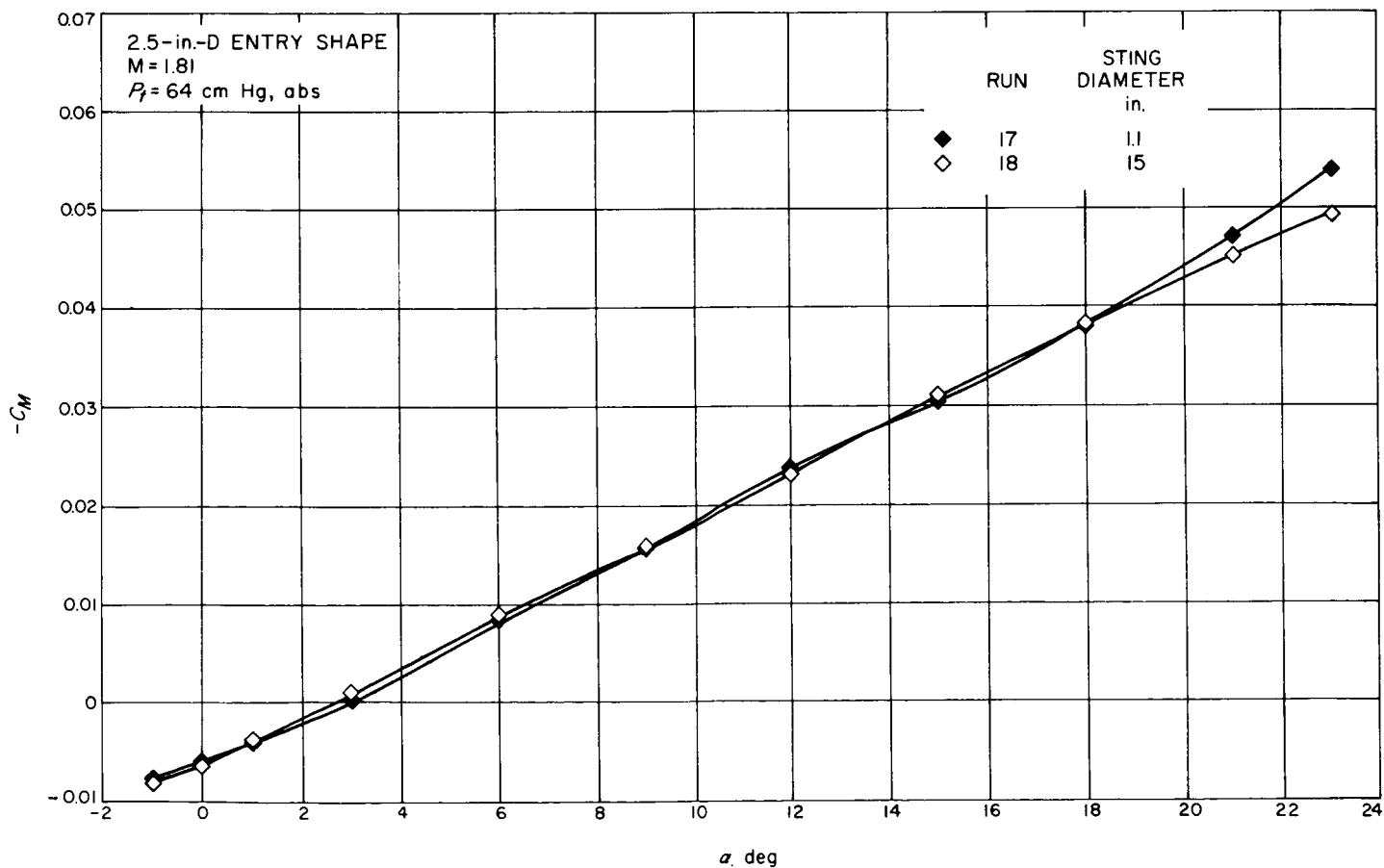
Plot 23. $-C_m$ vs α for an entry shape

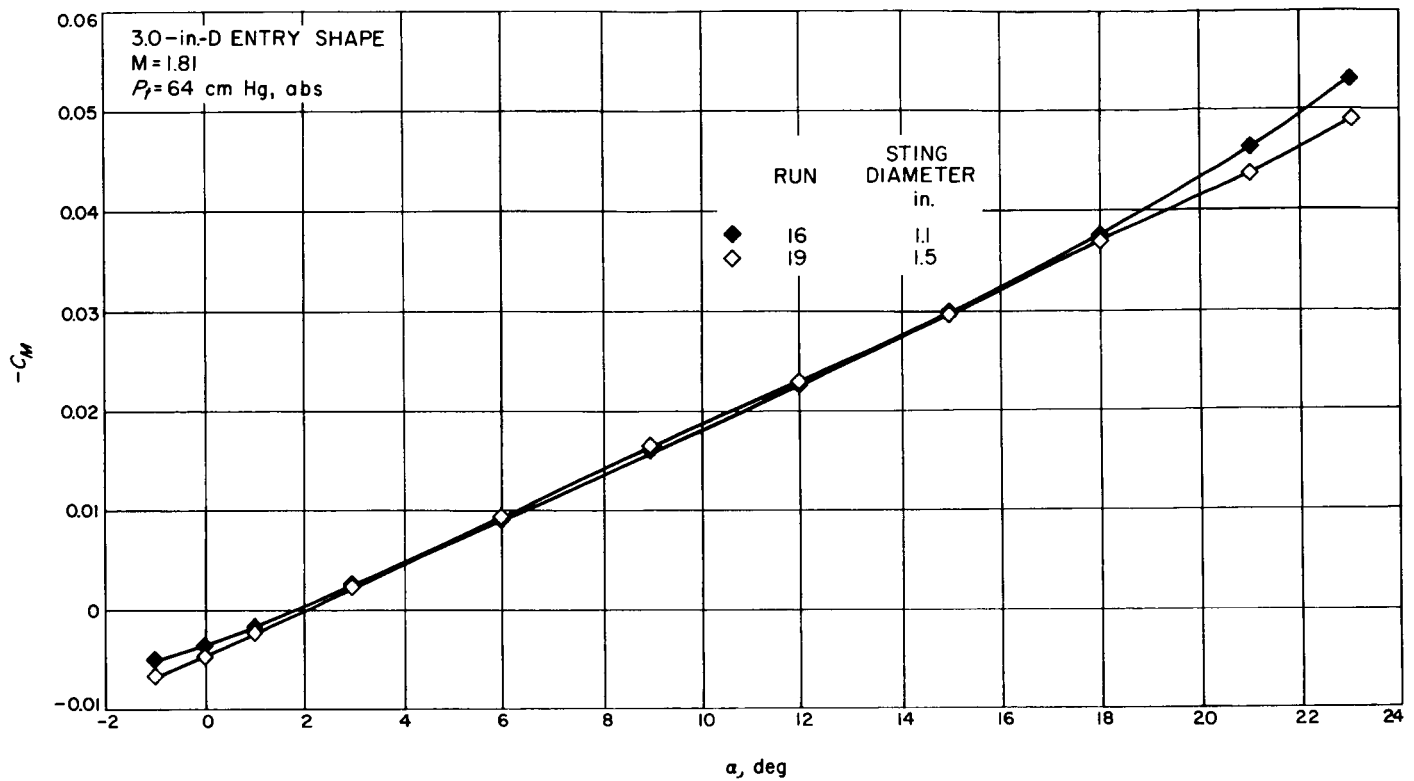
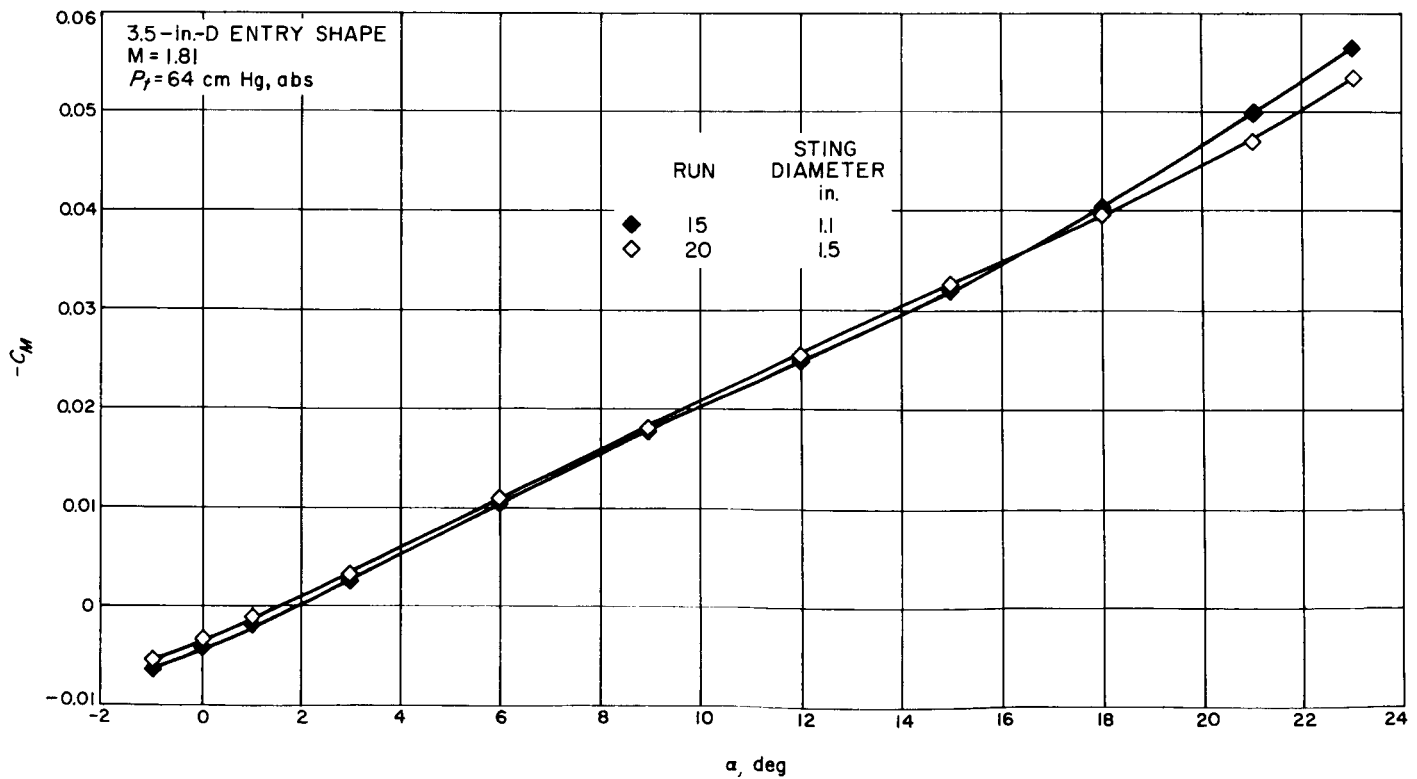
Plot 25. C_N vs α for an entry shapePlot 26. C_N vs α for an entry shapePlot 27. C_N vs α for an entry shape

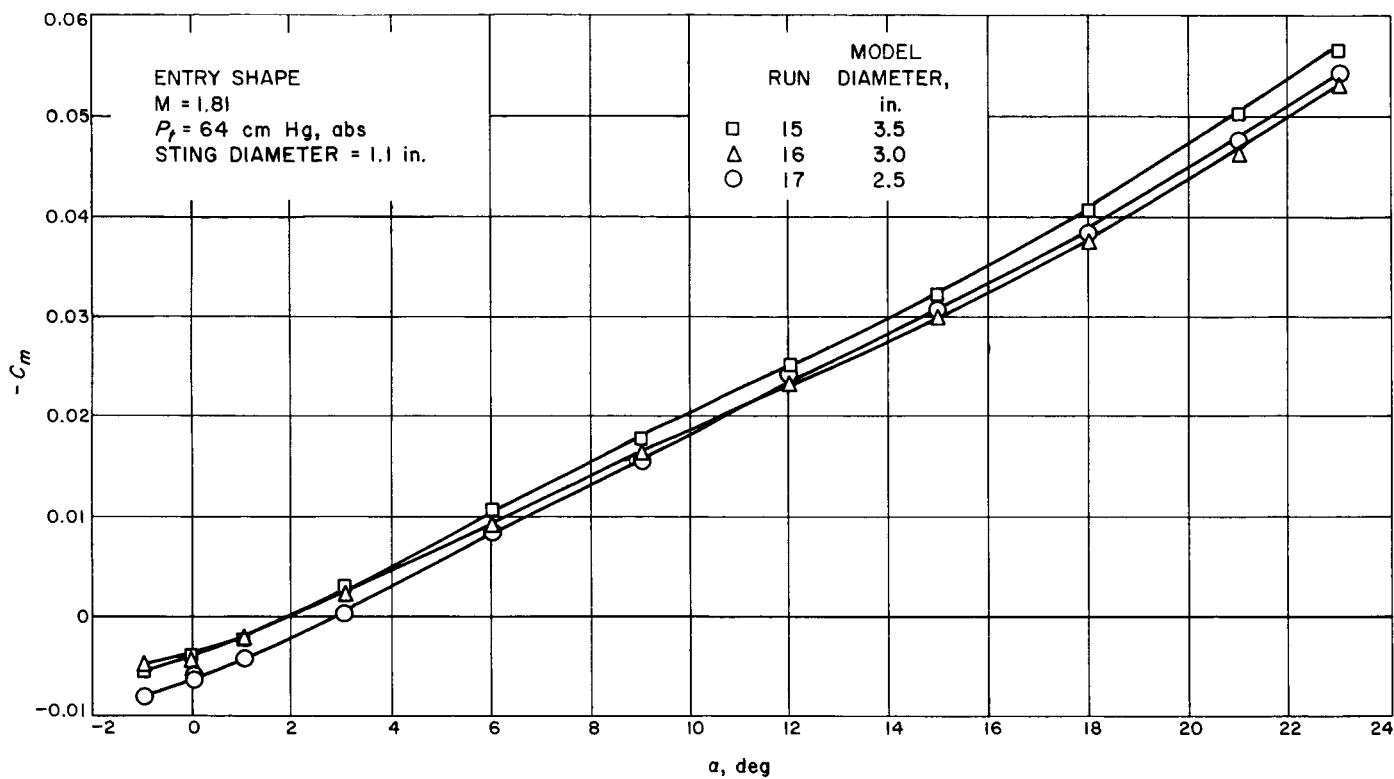
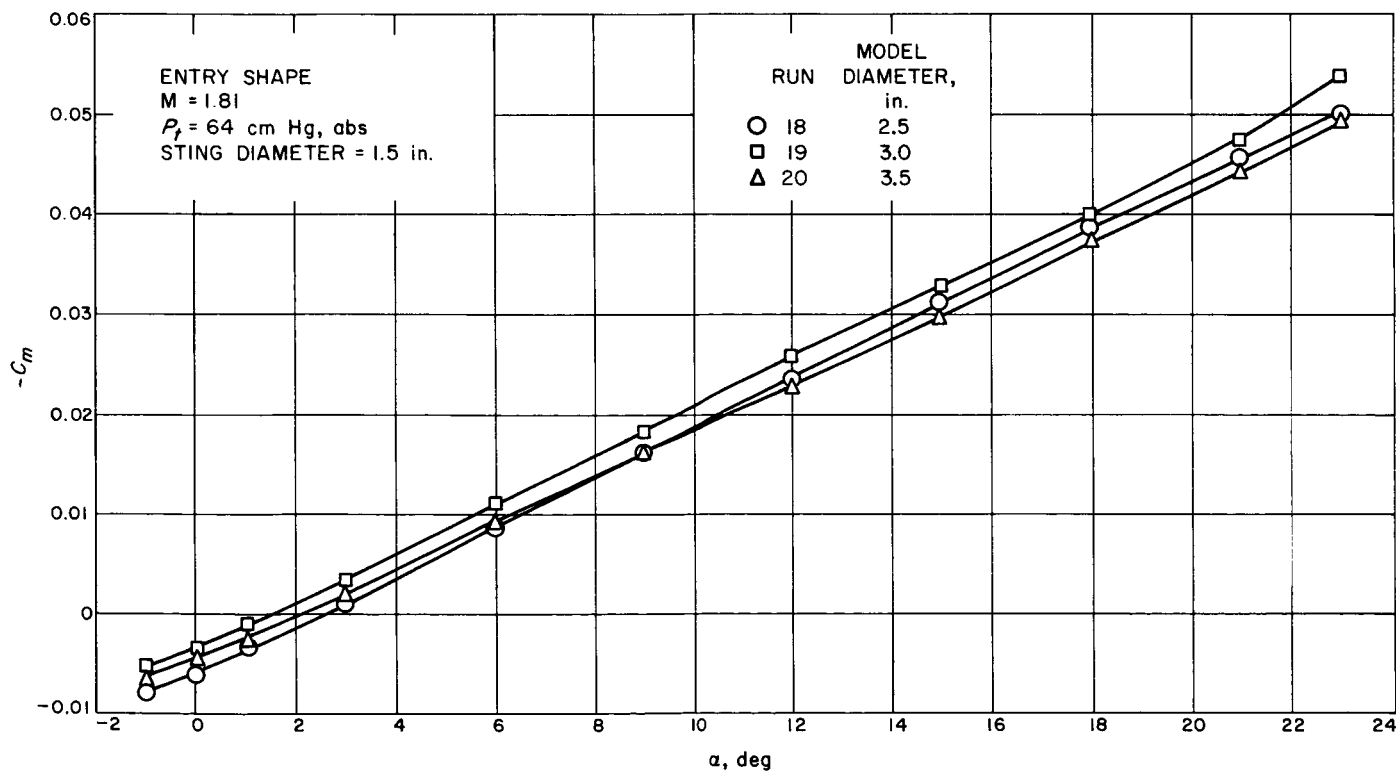
Plot 28. C_N vs α for an entry shapePlot 29. C_N vs α for an entry shape

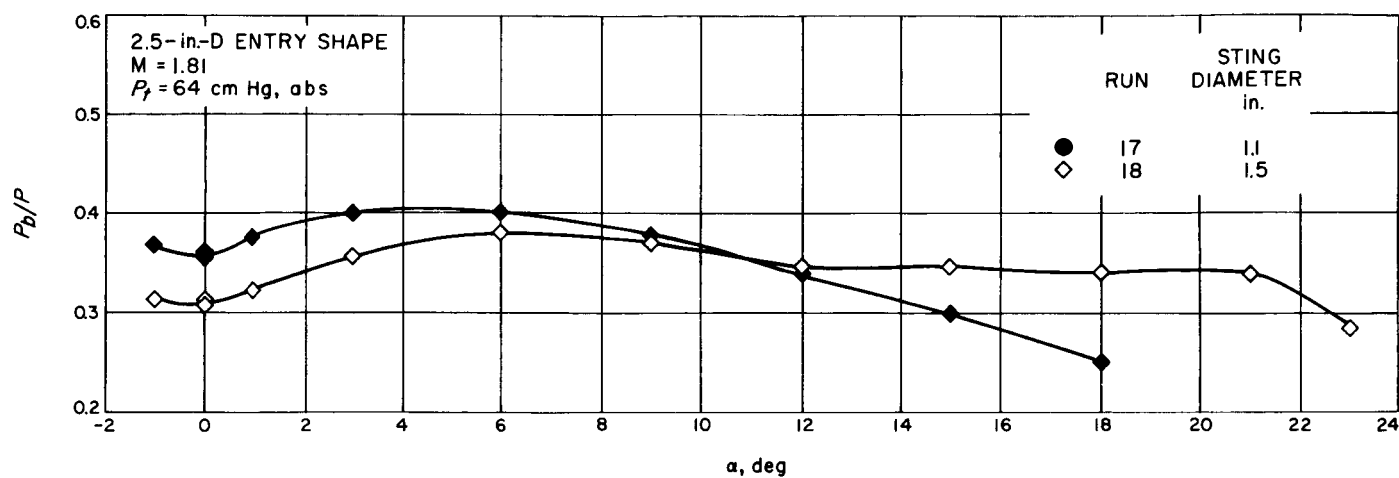
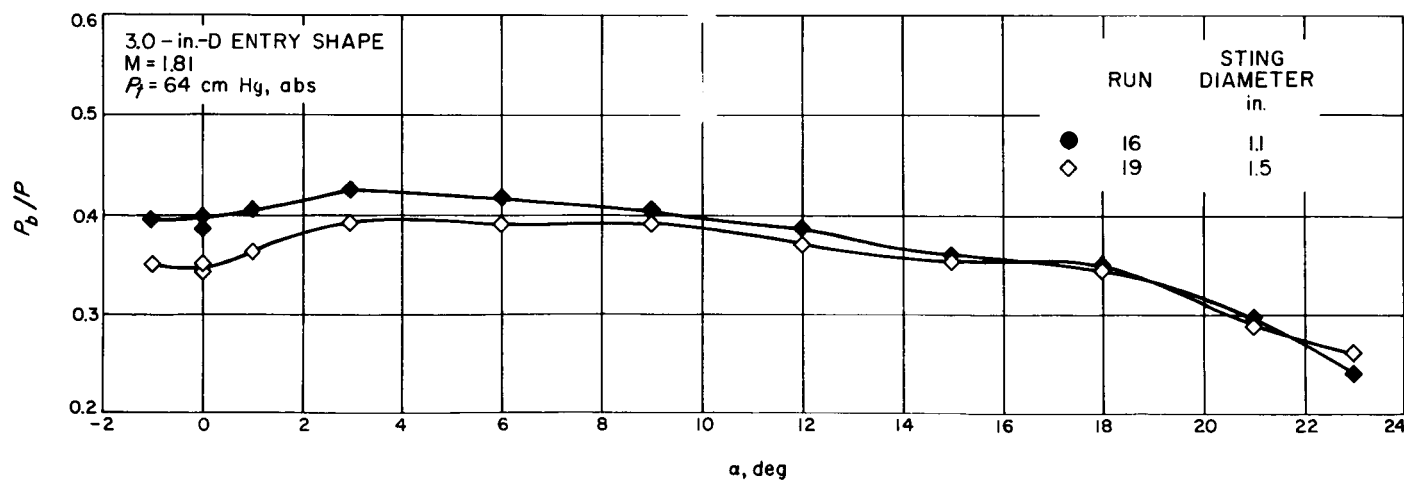
Plot 30. C_{Dc} vs α for an entry shapePlot 31. C_{Dc} vs α for an entry shape

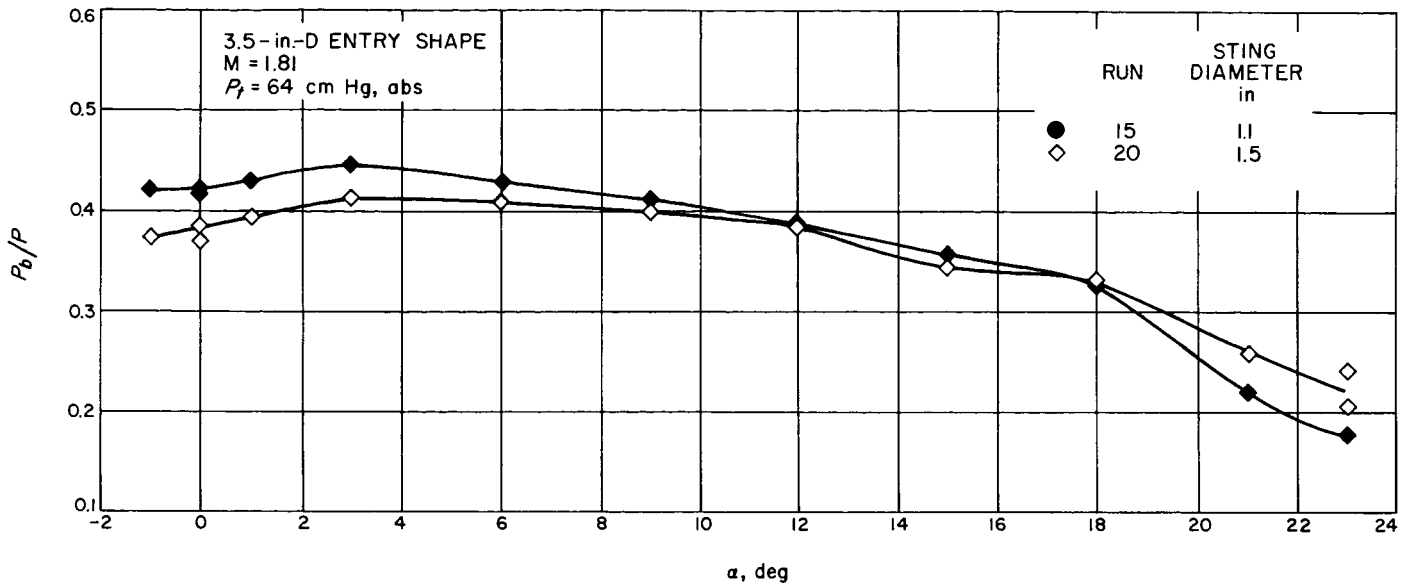
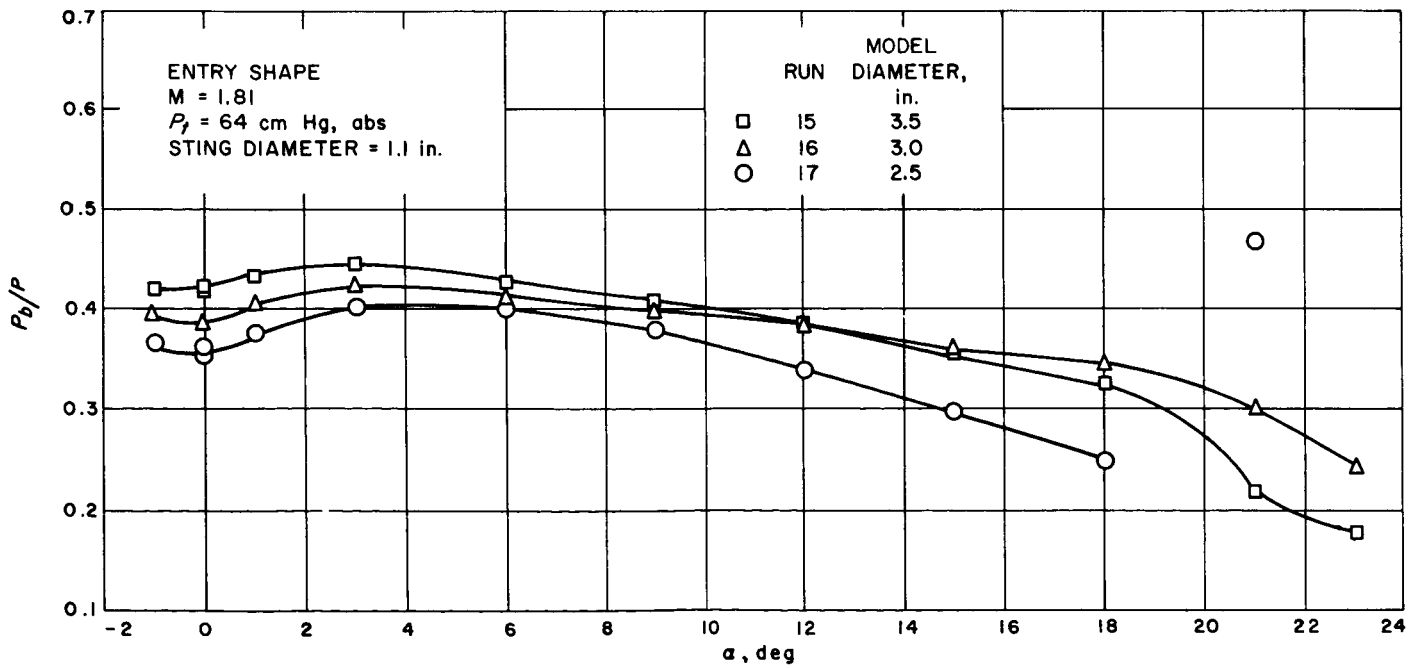
Plot 32. C_{Dc} vs α for an entry shapePlot 33. C_{Dc} vs α for an entry shape

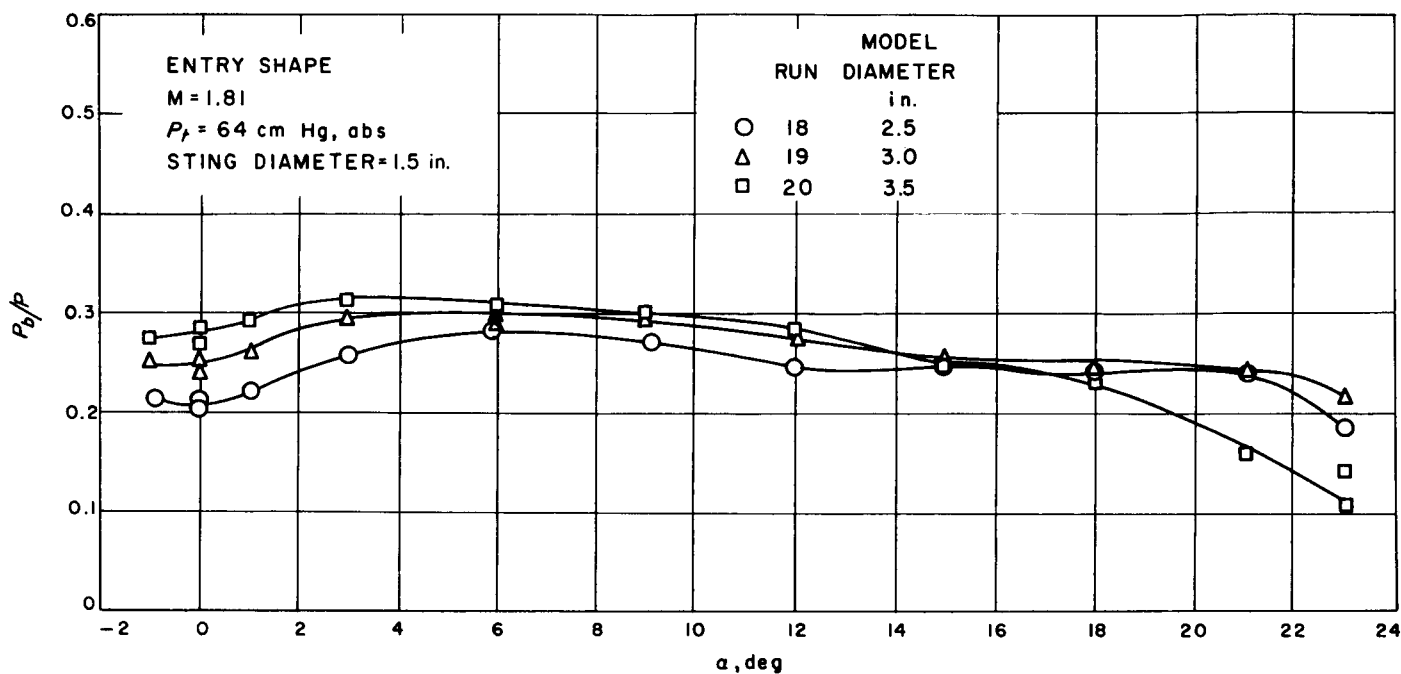
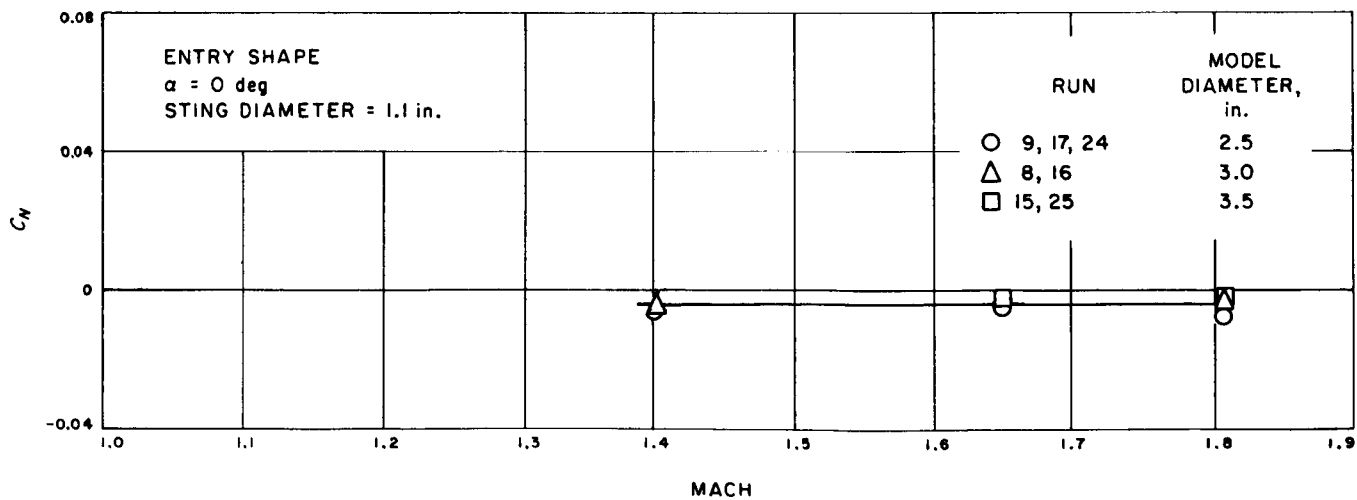
Plot 34. C_{D_c} vs α for an entry shapePlot 35. $-C_m$ vs α for an entry shape

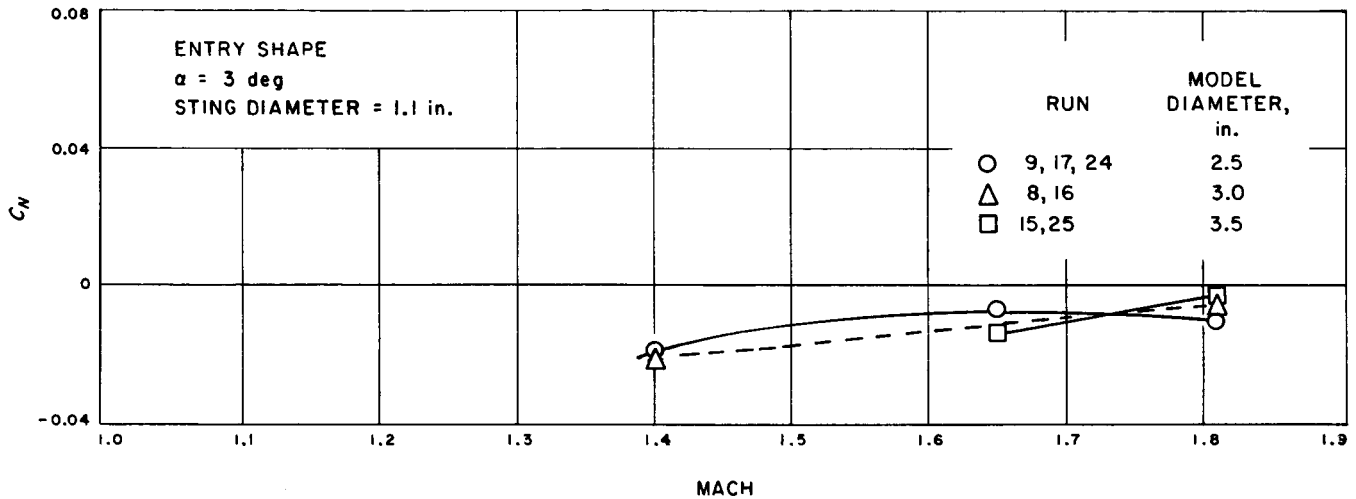
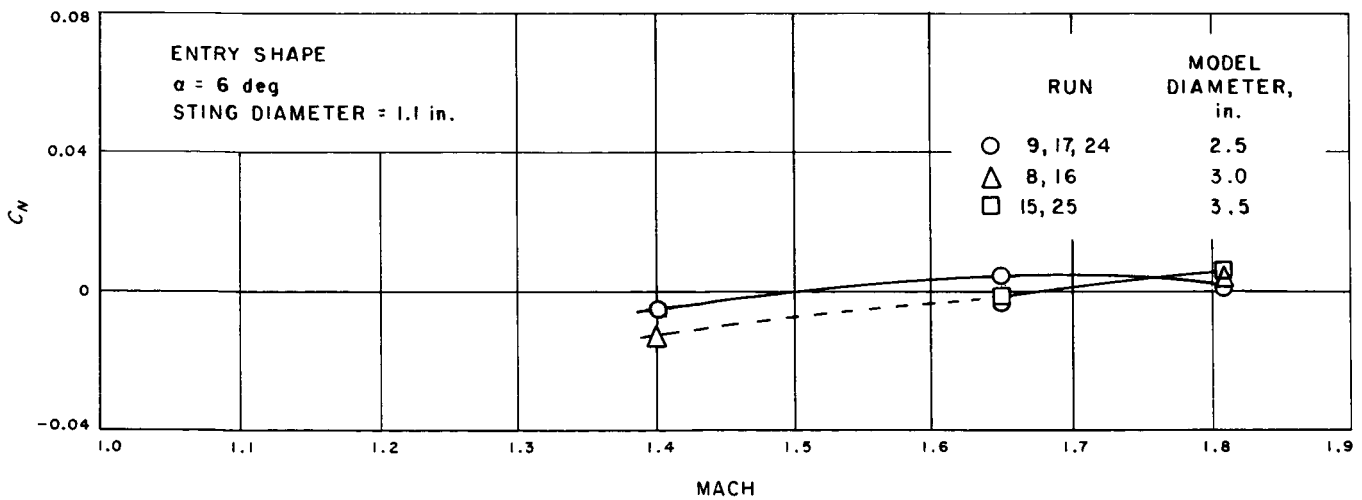
Plot 36. $-C_m$ vs α for an entry shapePlot 37. $-C_m$ vs α for an entry shape

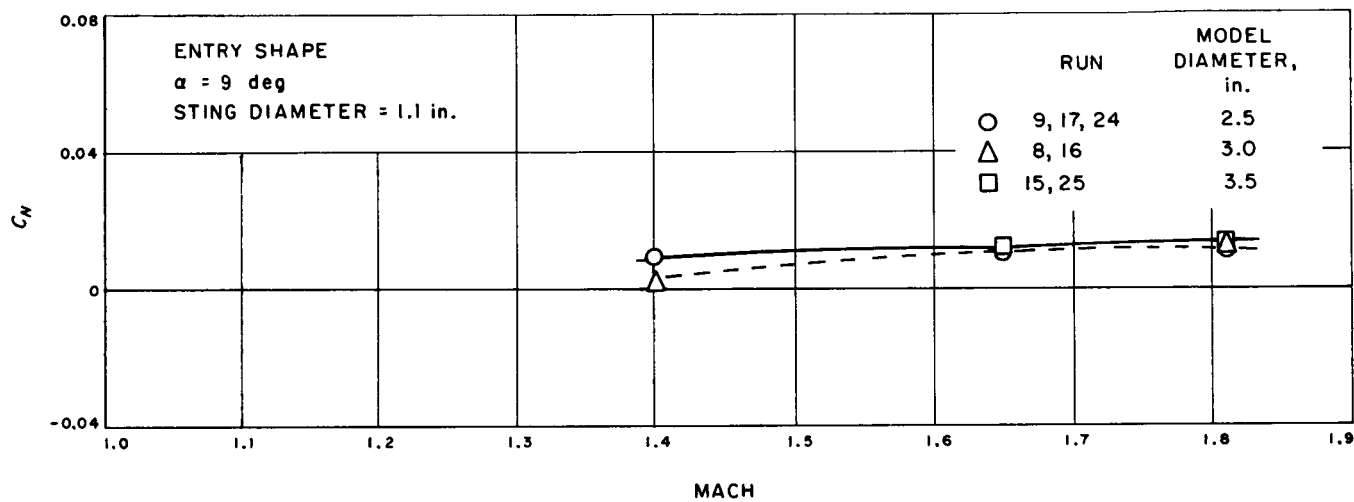
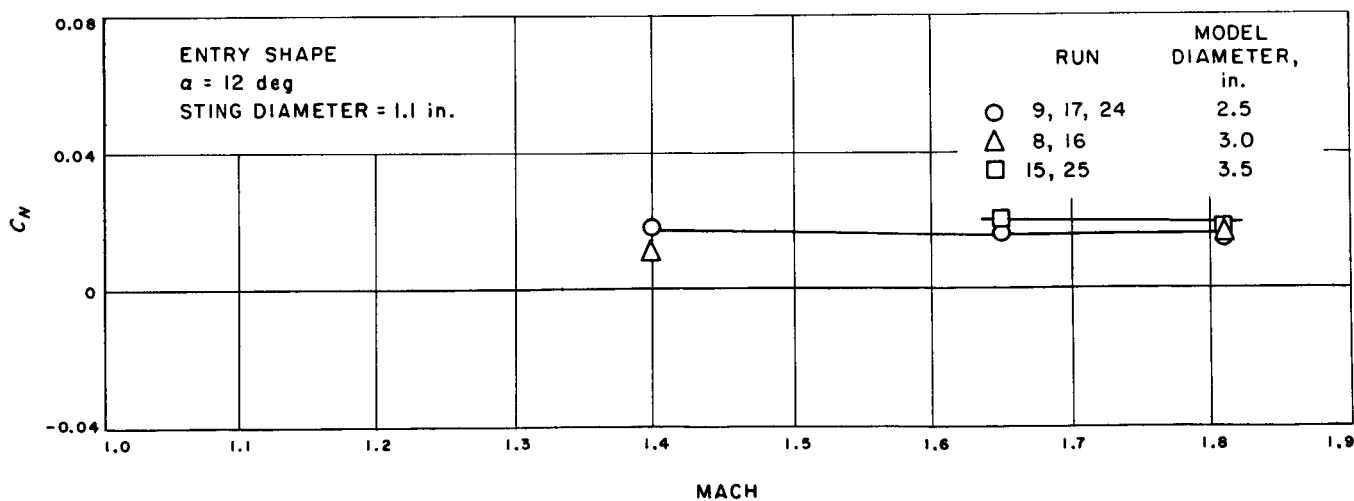
Plot 38. $-C_m$ vs α for an entry shapePlot 39. $-C_m$ vs α for an entry shape

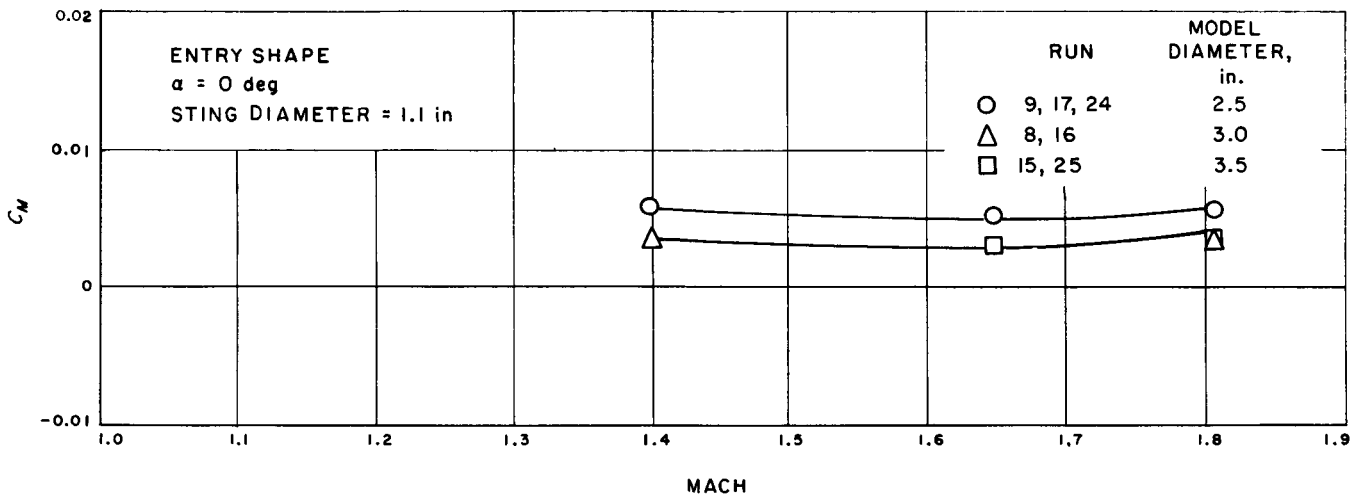
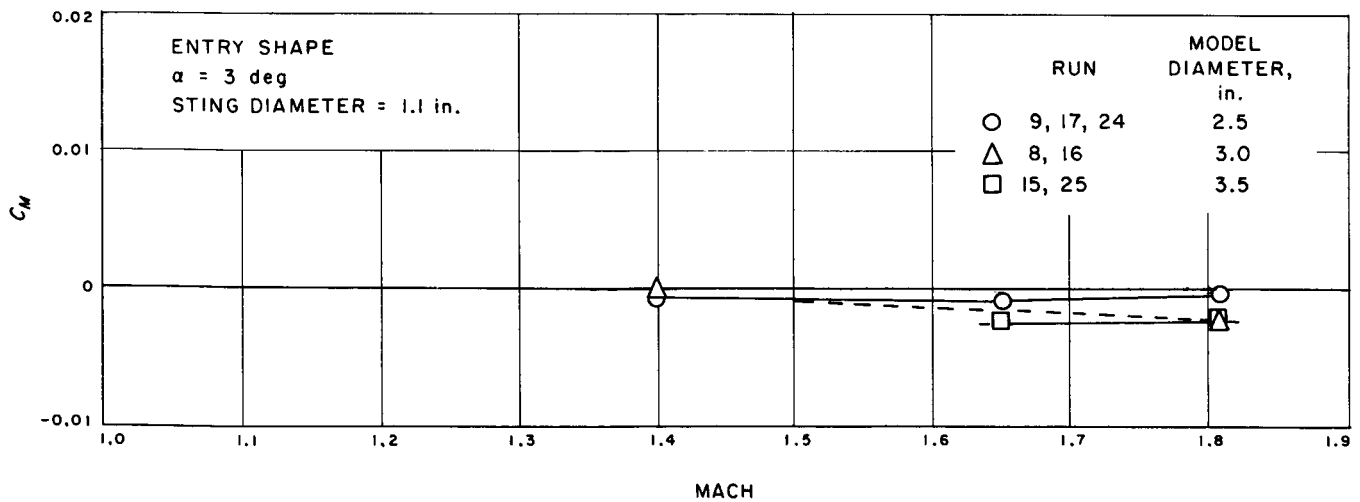
Plot 40. P_b/P vs α for an entry shapePlot 41. P_b/P vs α for an entry shape

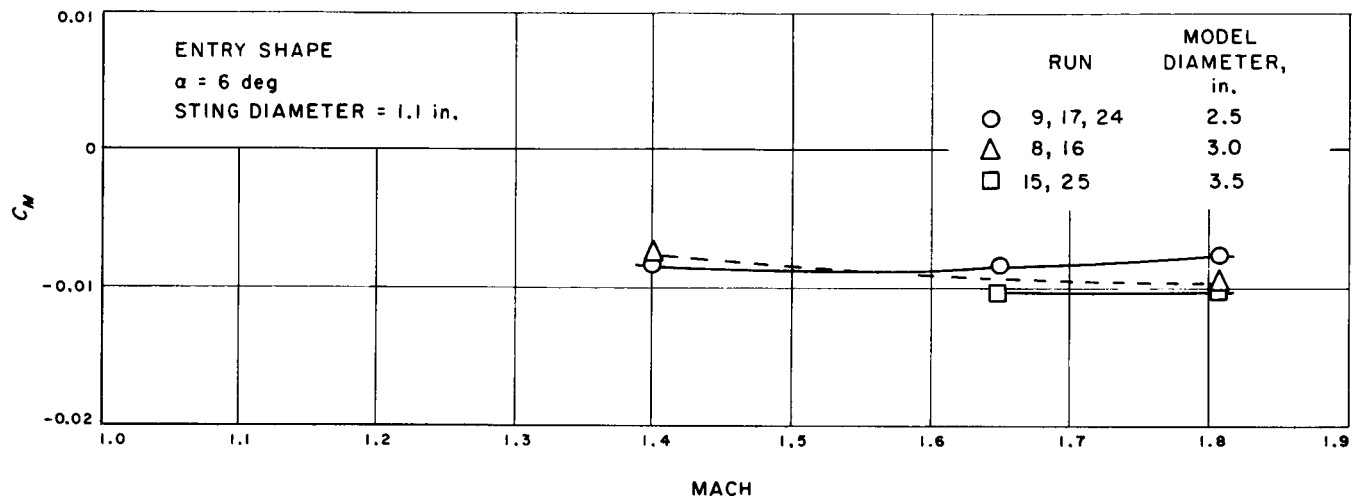
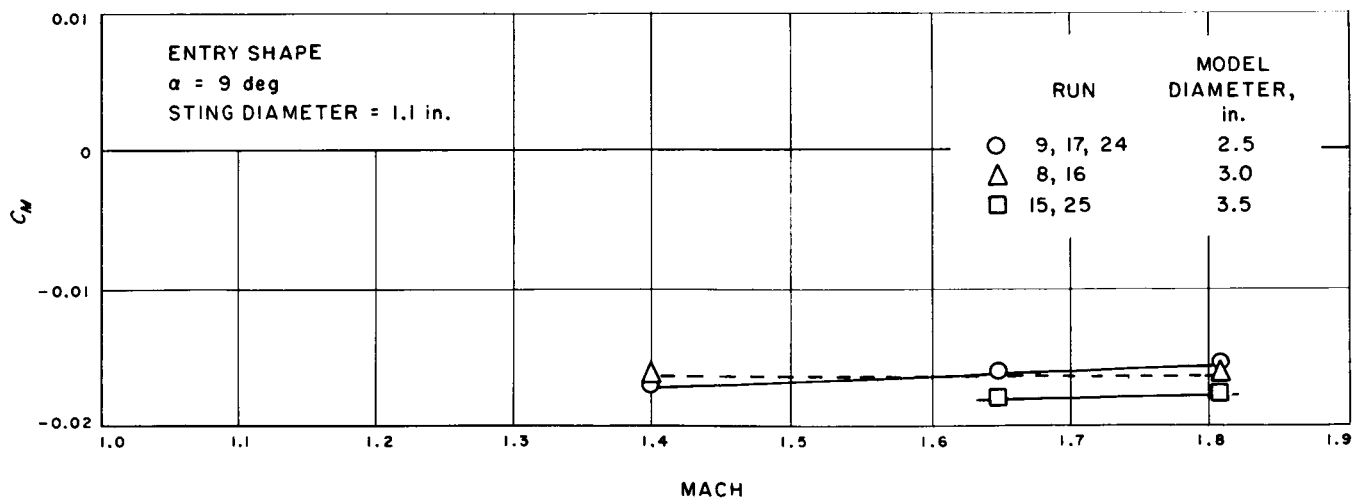
Plot 42. P_b/P vs α for an entry shapePlot 43. P_b/P vs α for an entry shape

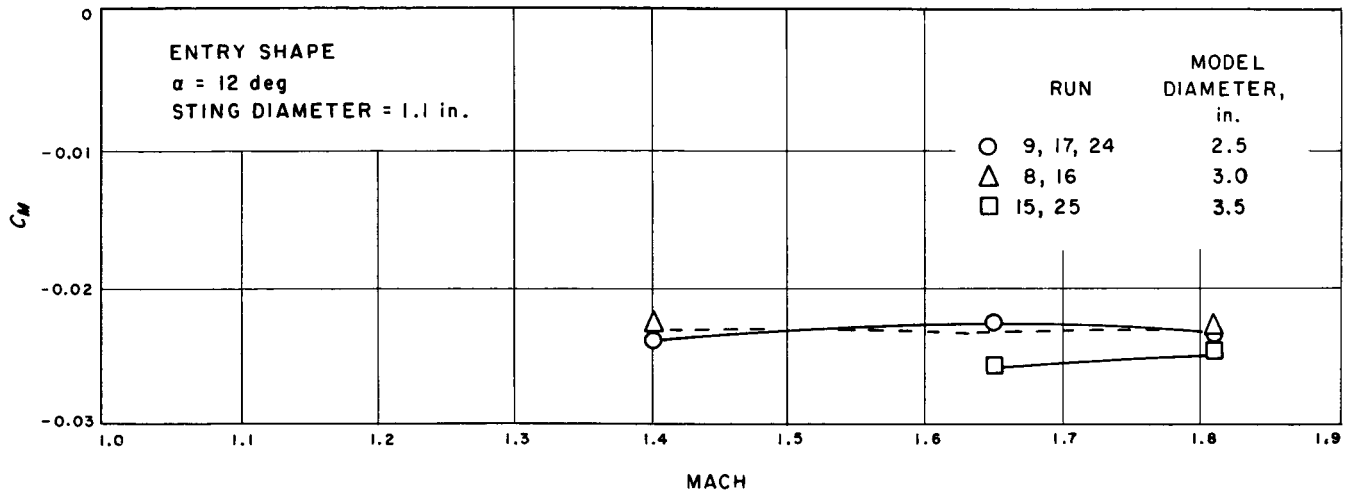
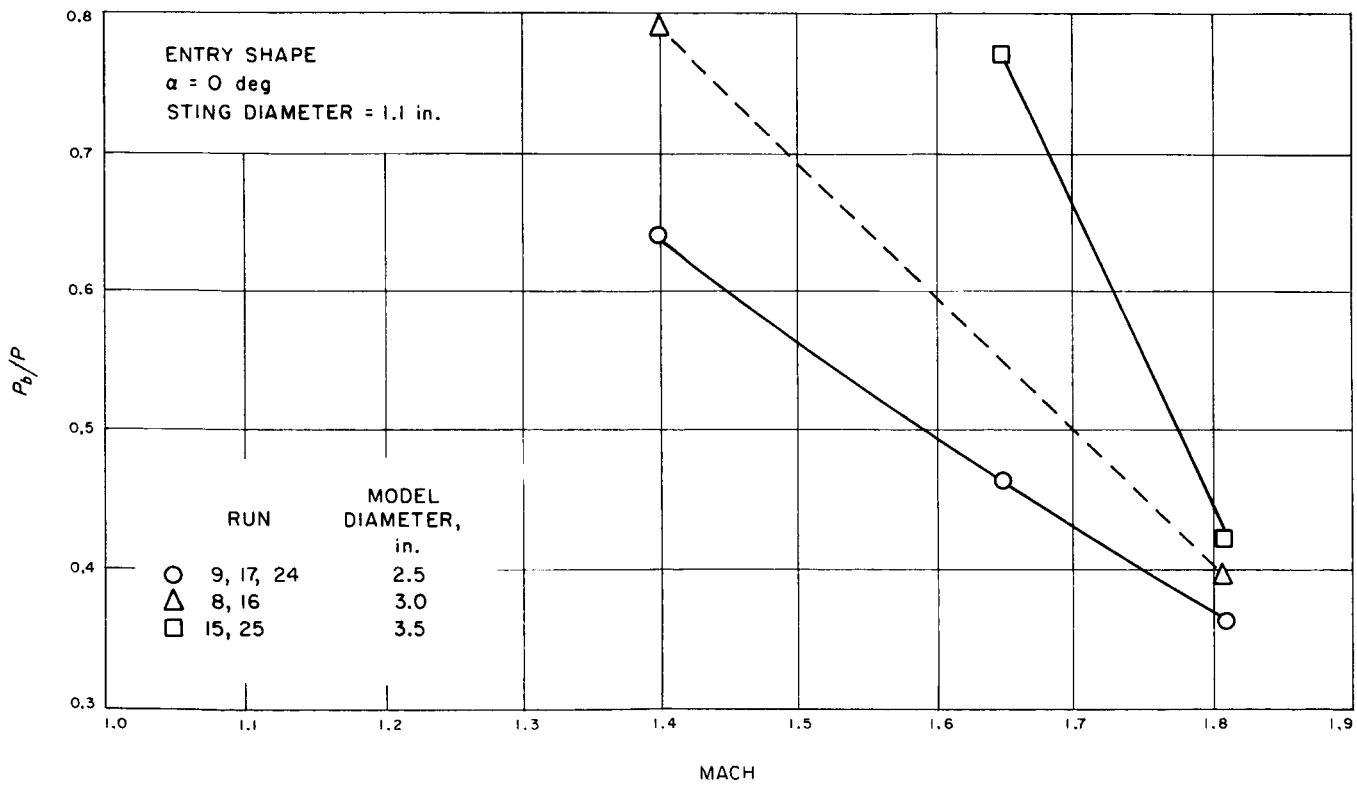
Plot 44. P_b/P vs α for an entry shapePlot 45. C_N vs Mach for an entry shape

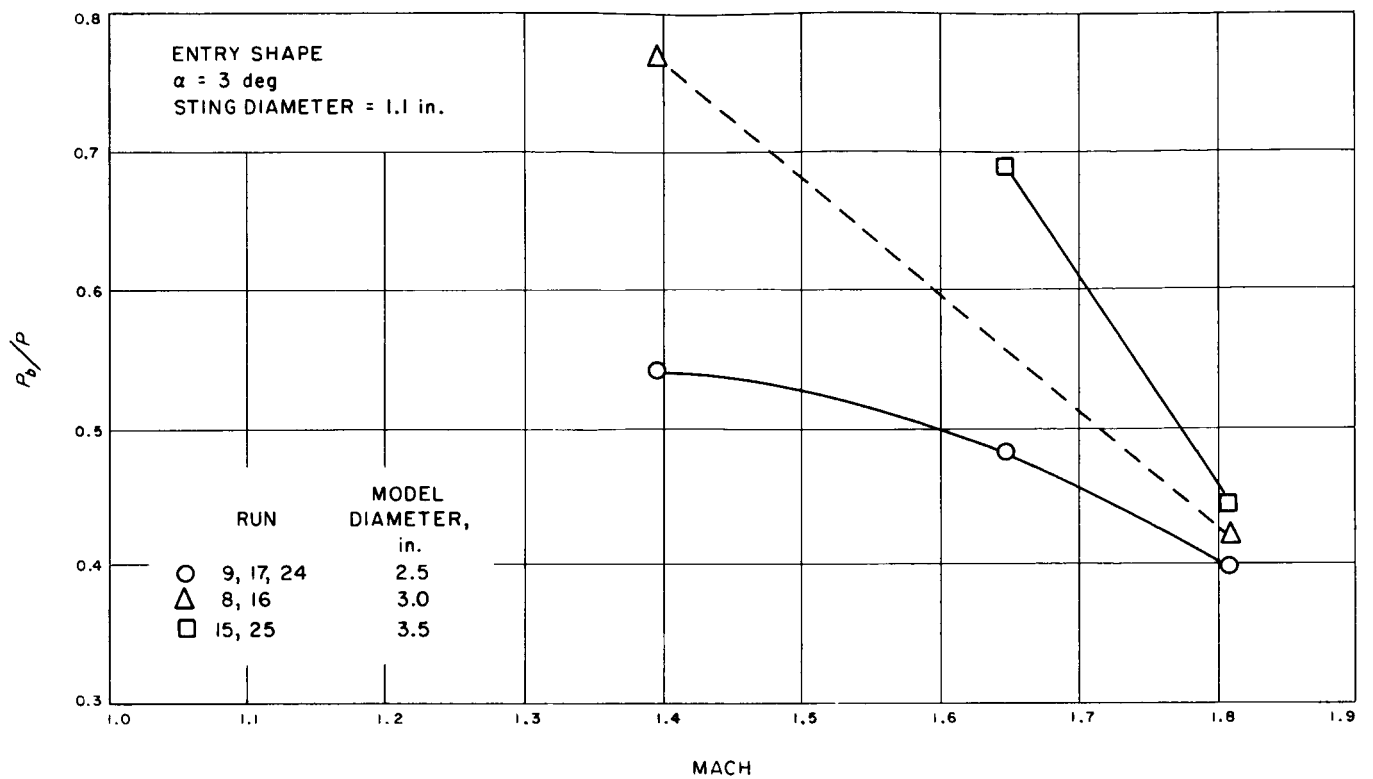
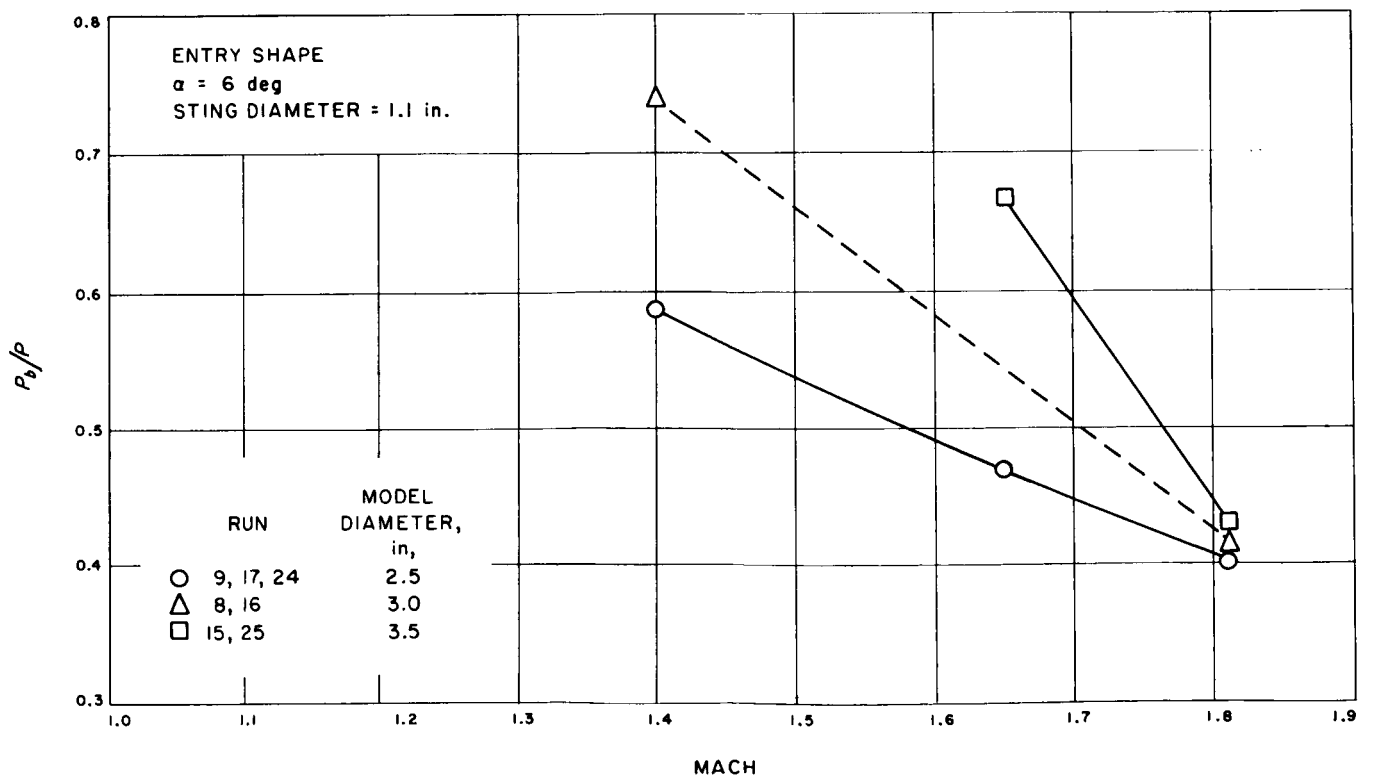
Plot 46. C_N vs Mach for an entry shapePlot 47. C_N vs Mach for an entry shape

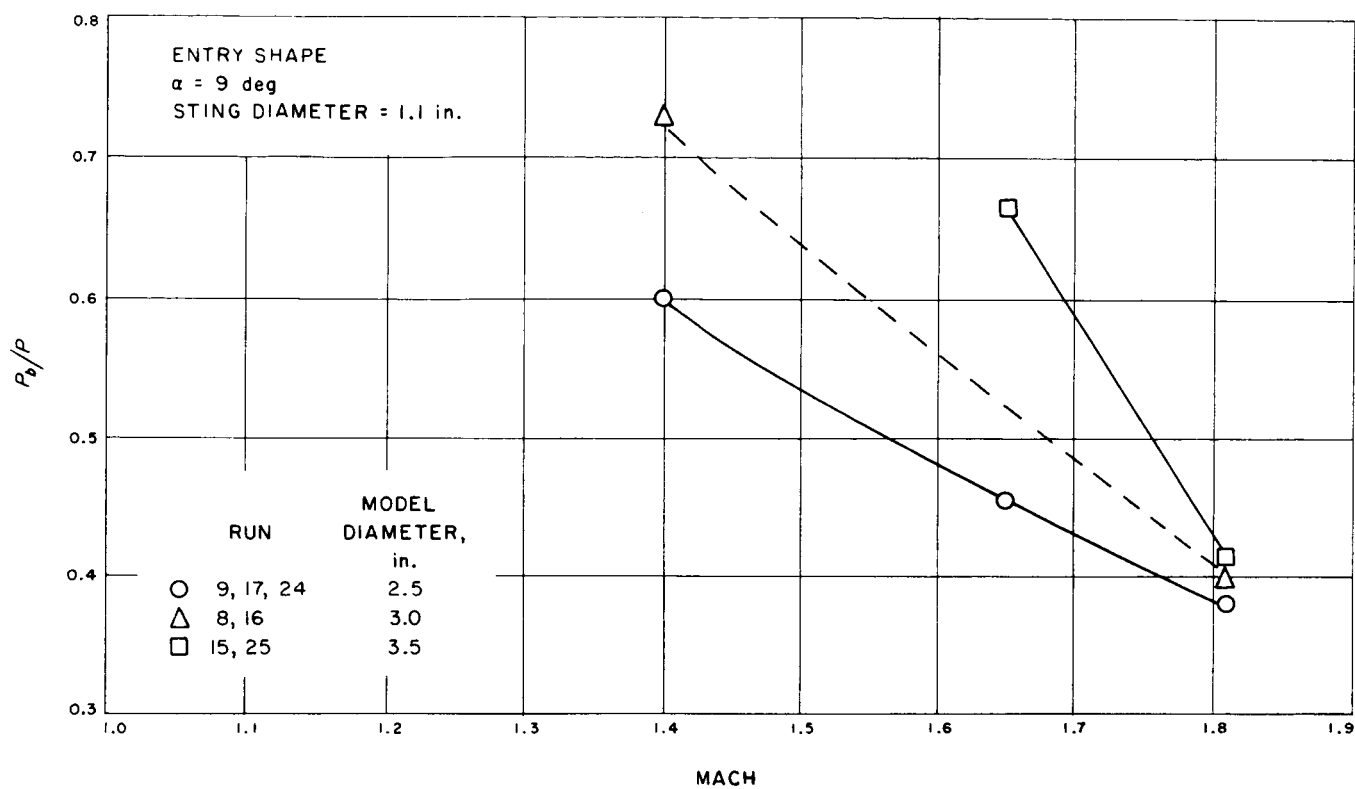
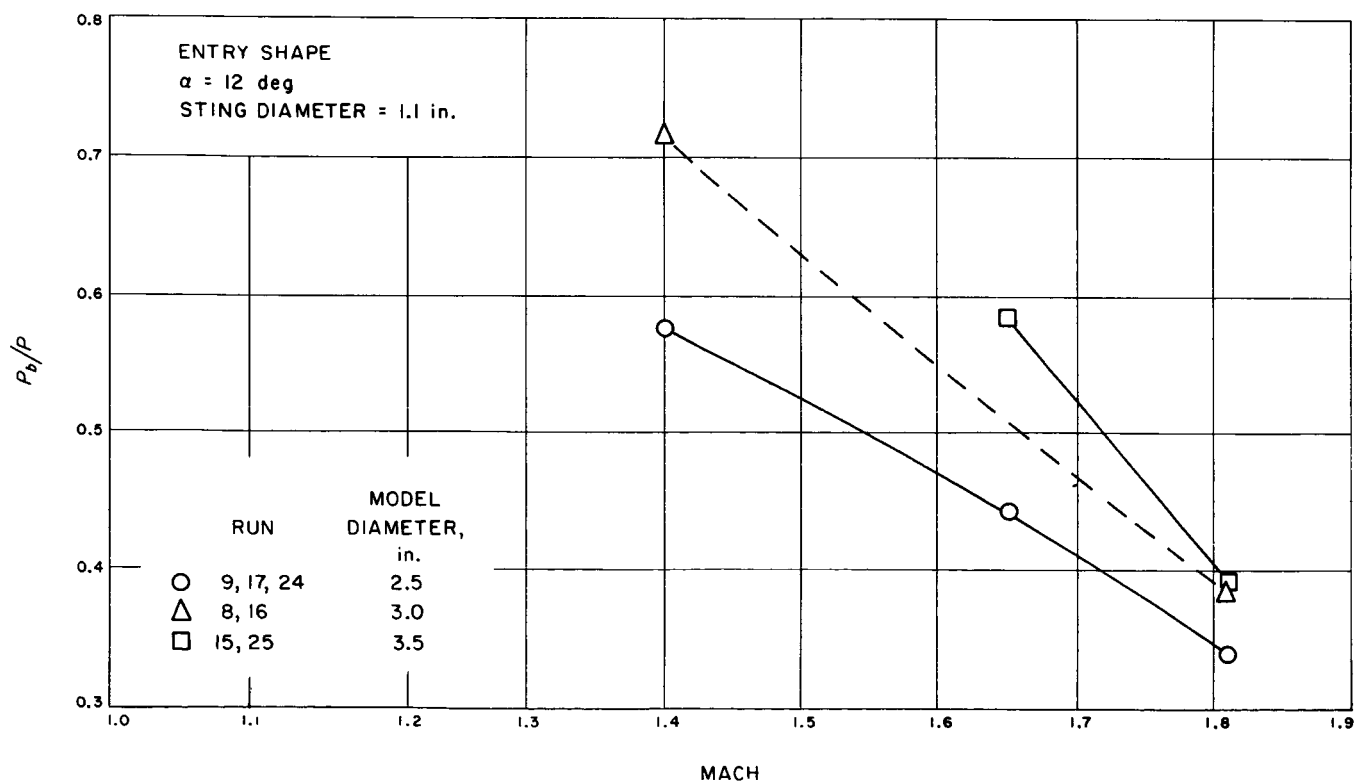
Plot 48. C_N vs Mach for an entry shapePlot 49. C_N vs Mach for an entry shape

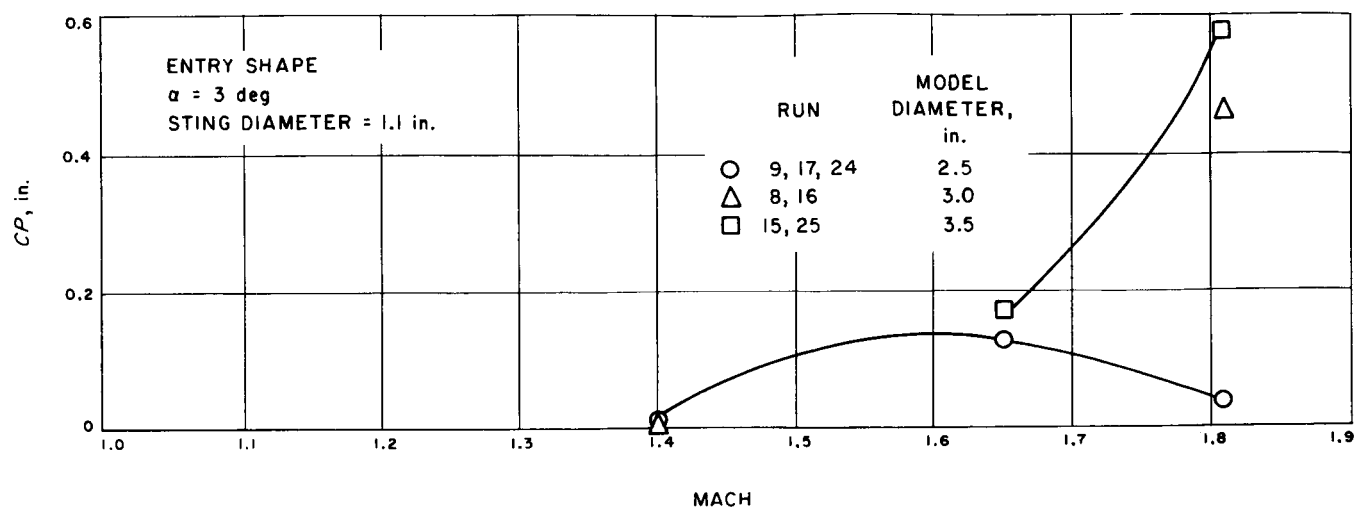
Plot 50. C_M vs Mach for an entry shapePlot 51. C_M vs Mach for an entry shape

Plot 52. C_M vs Mach for an entry shapePlot 53. C_M vs Mach for an entry shape

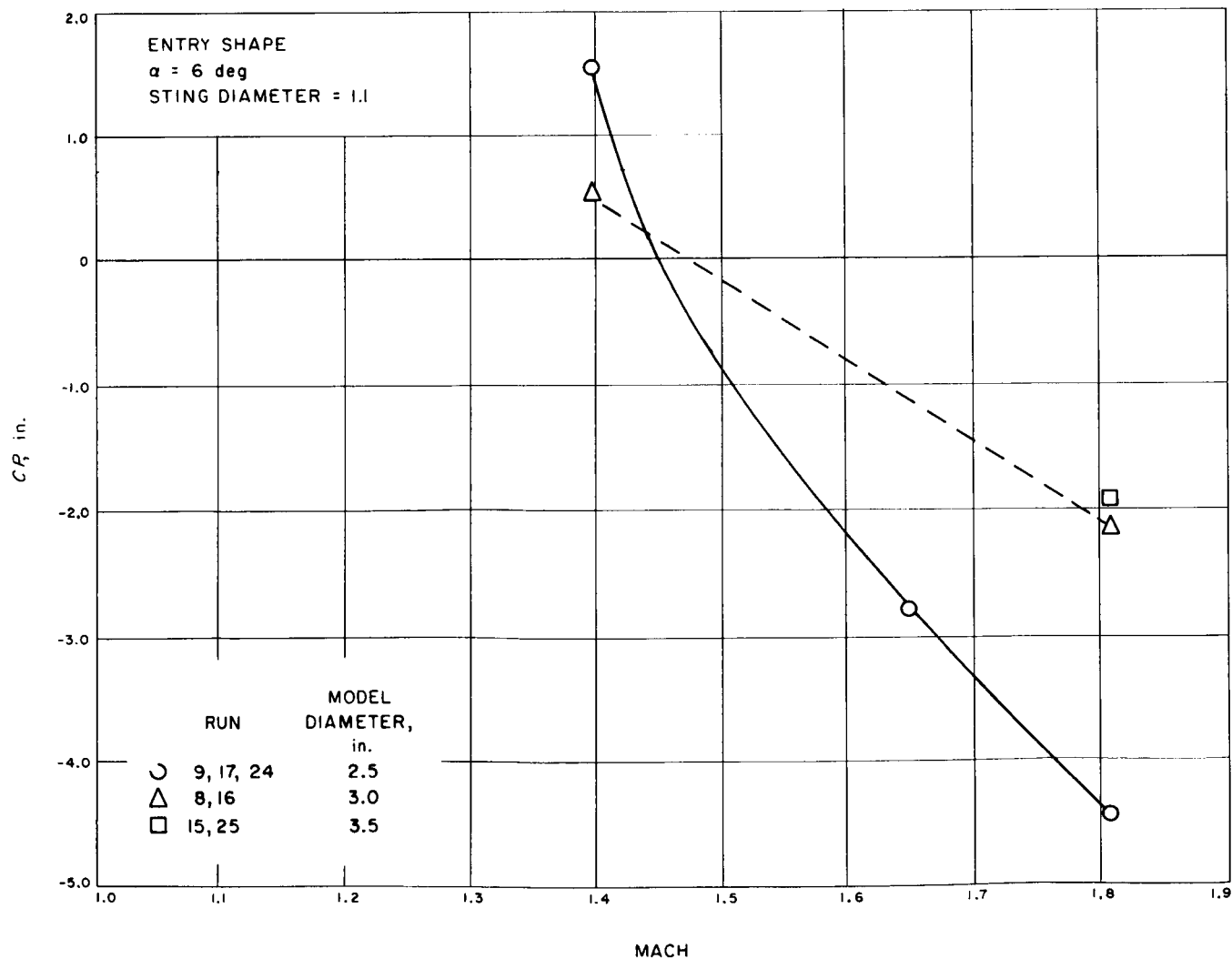
Plot 54. C_M vs Mach for an entry shapePlot 55. P_b/P vs Mach for an entry shape

Plot 56. P_b/P vs Mach for an entry shapePlot 57. P_b/P vs Mach for an entry shape

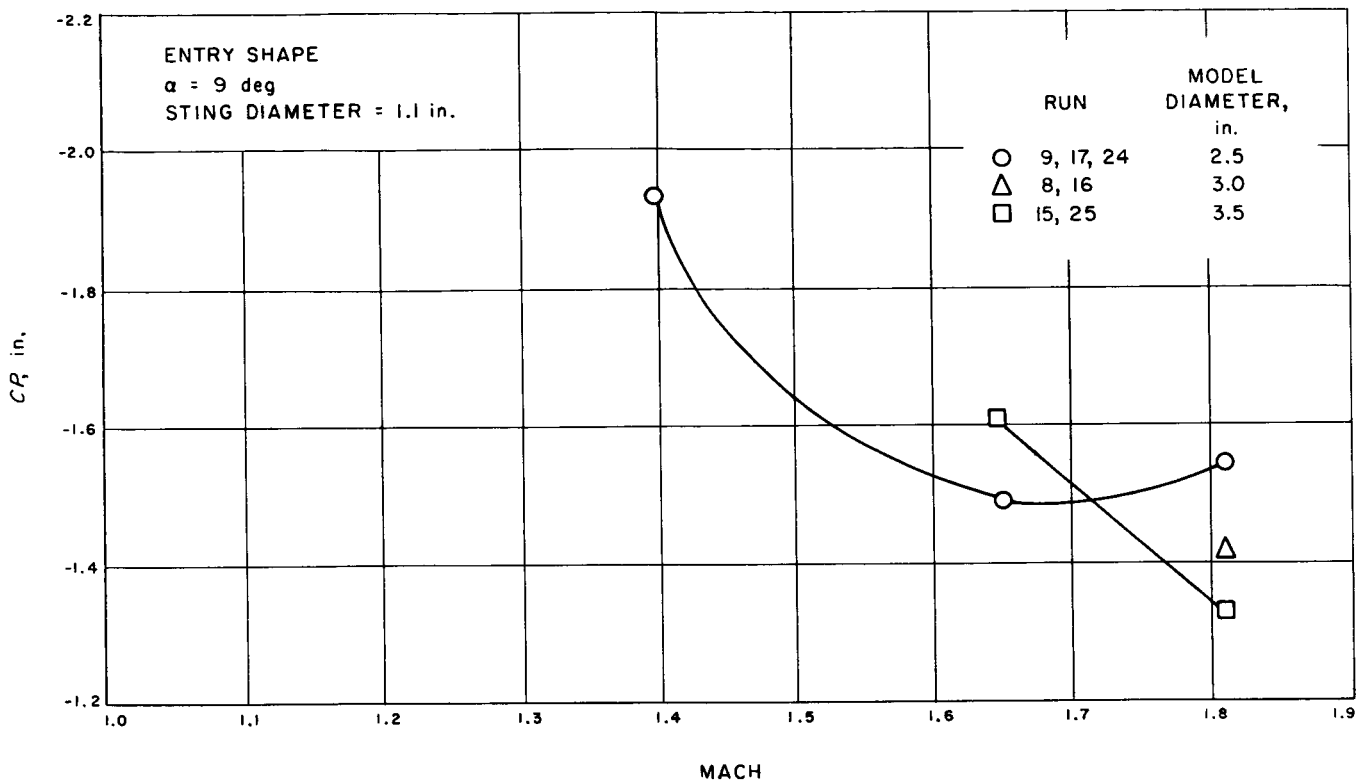
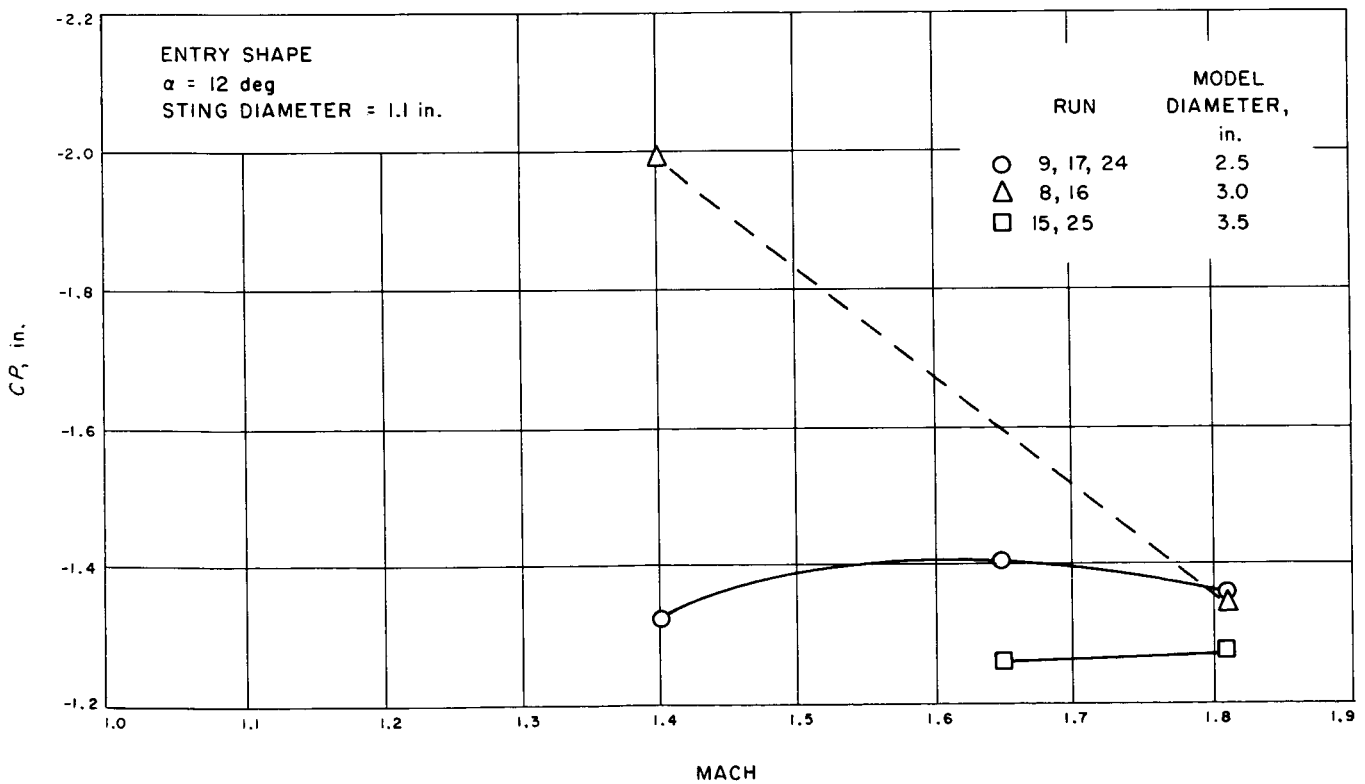
Plot 58. P_b/P vs Mach for an entry shapePlot 59. P_b/P vs Mach for an entry shape

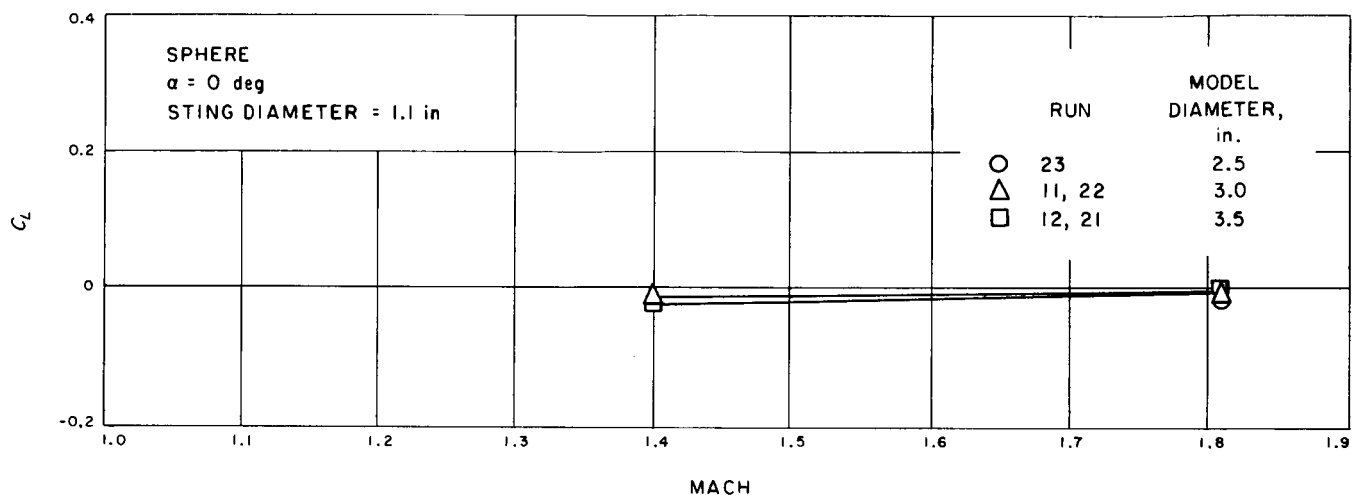
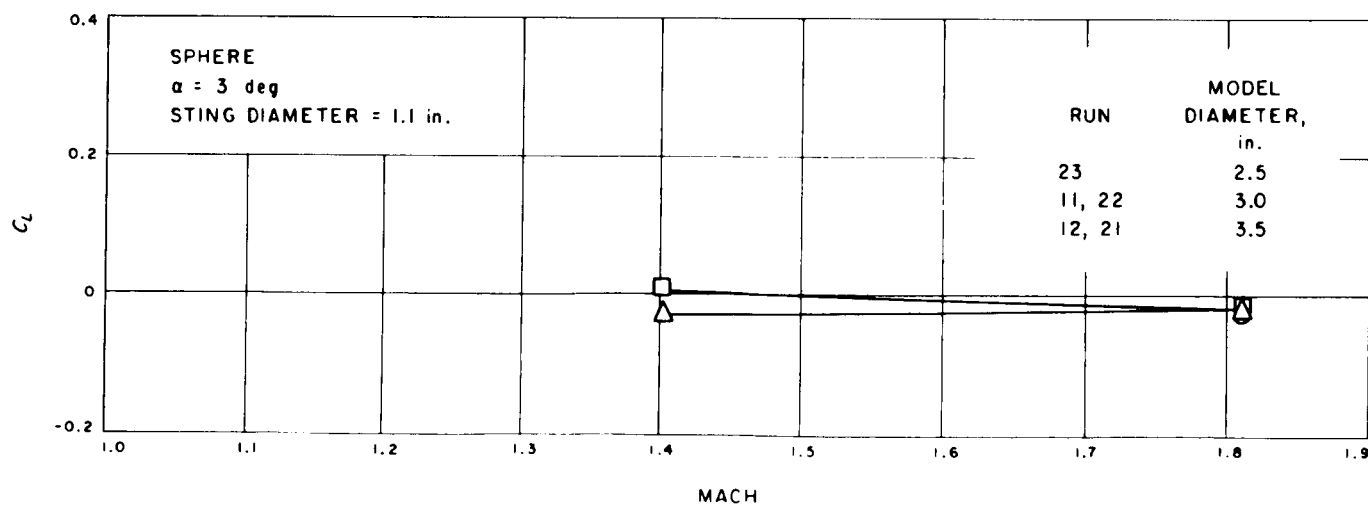


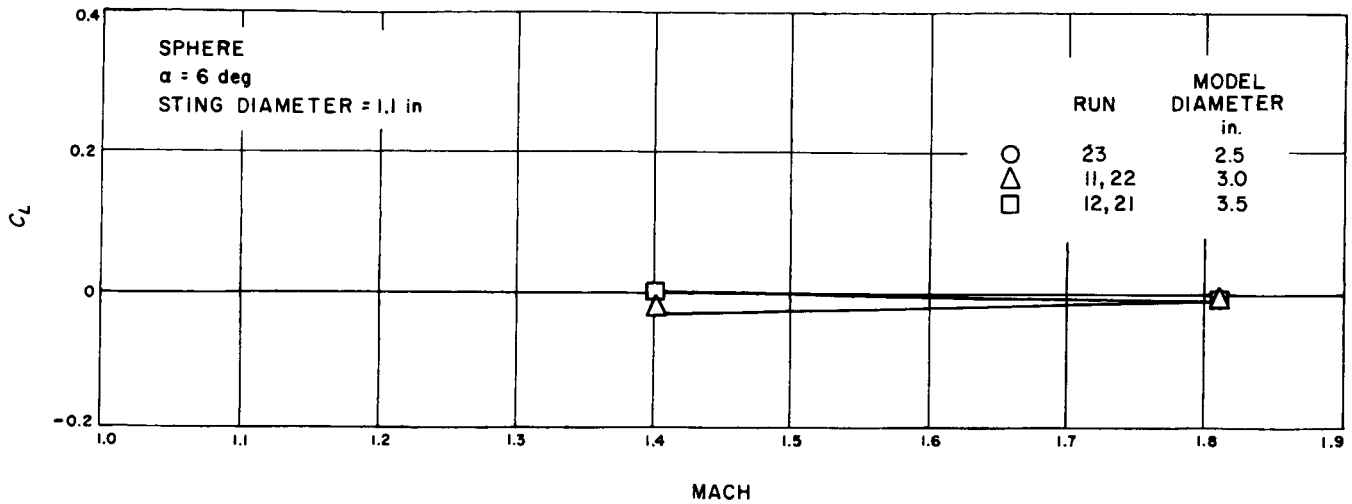
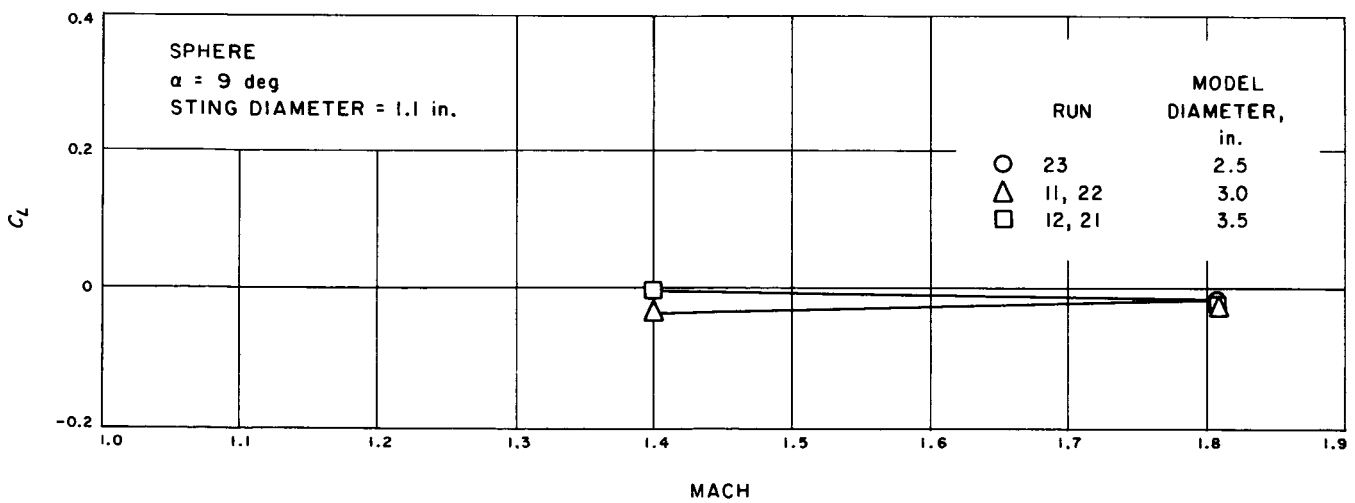
Plot 60. C.P. (in.) vs Mach for an entry shape

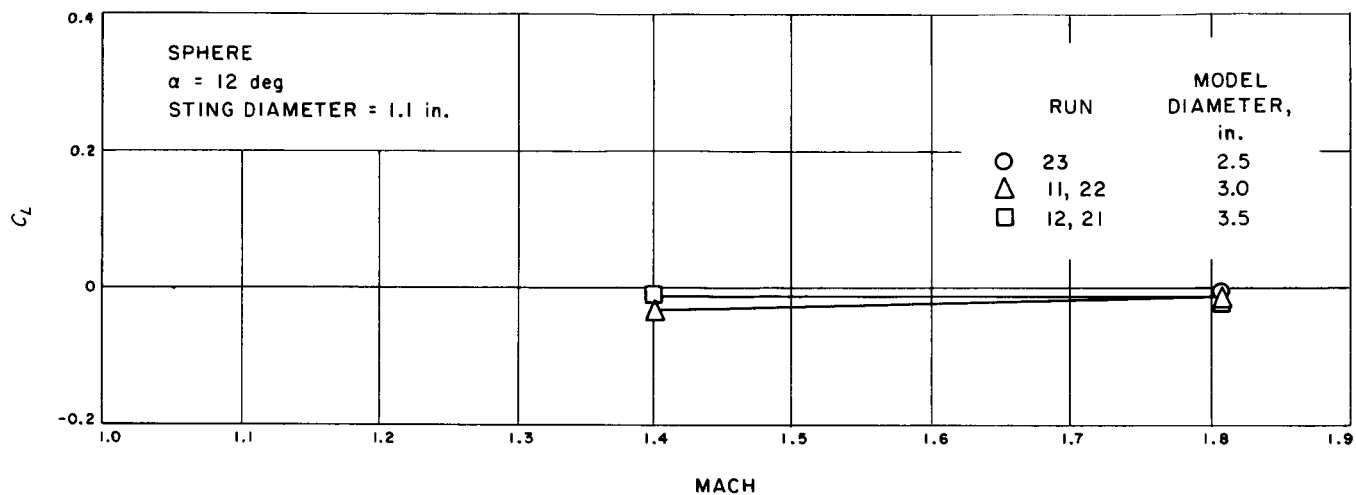
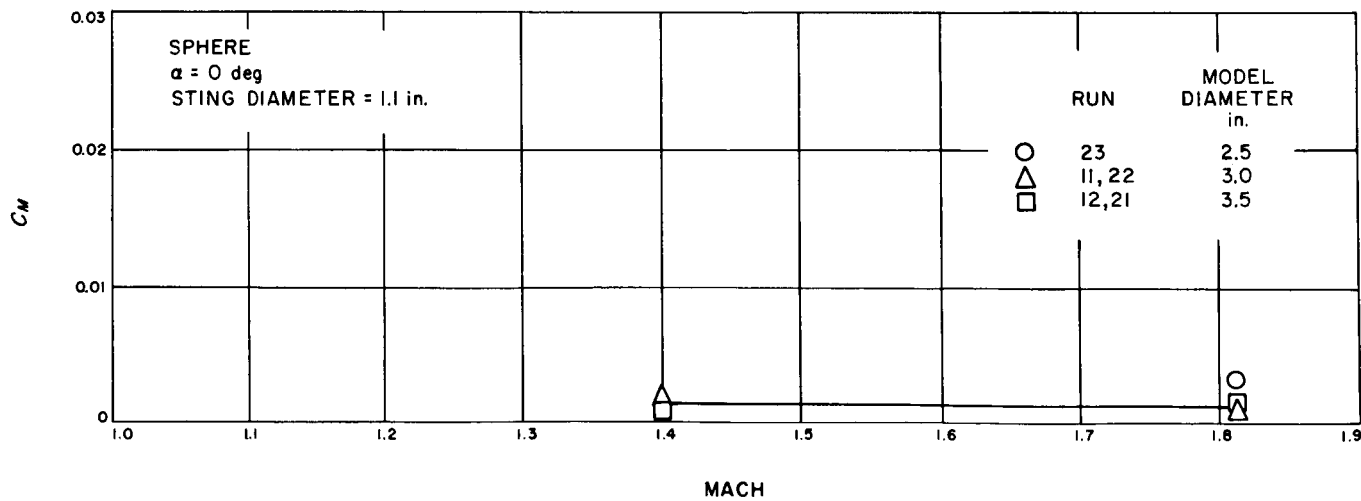


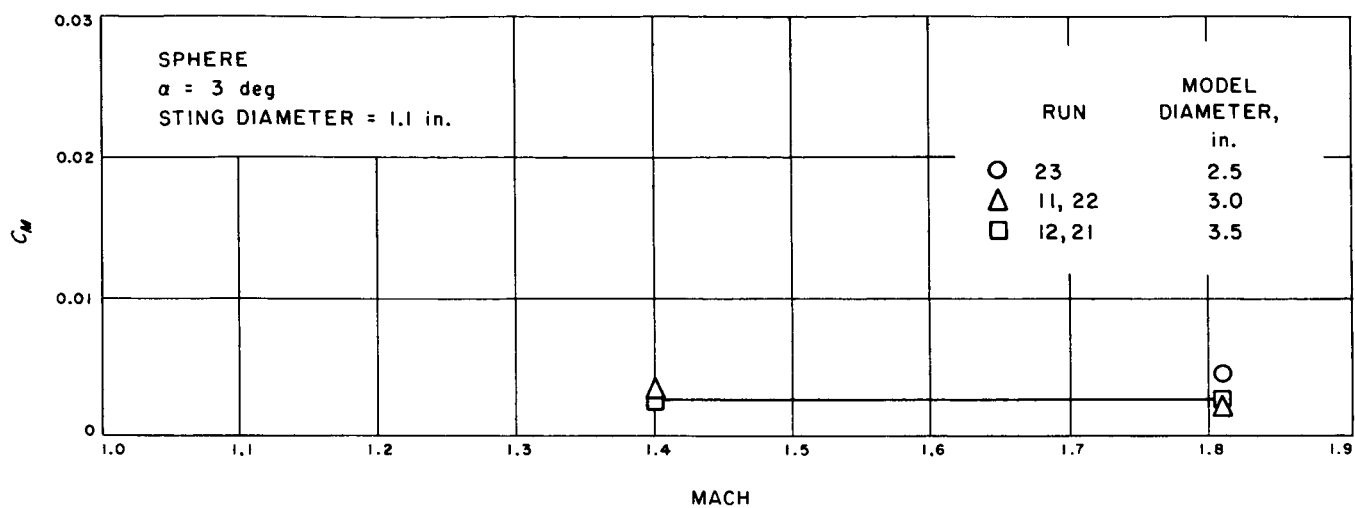
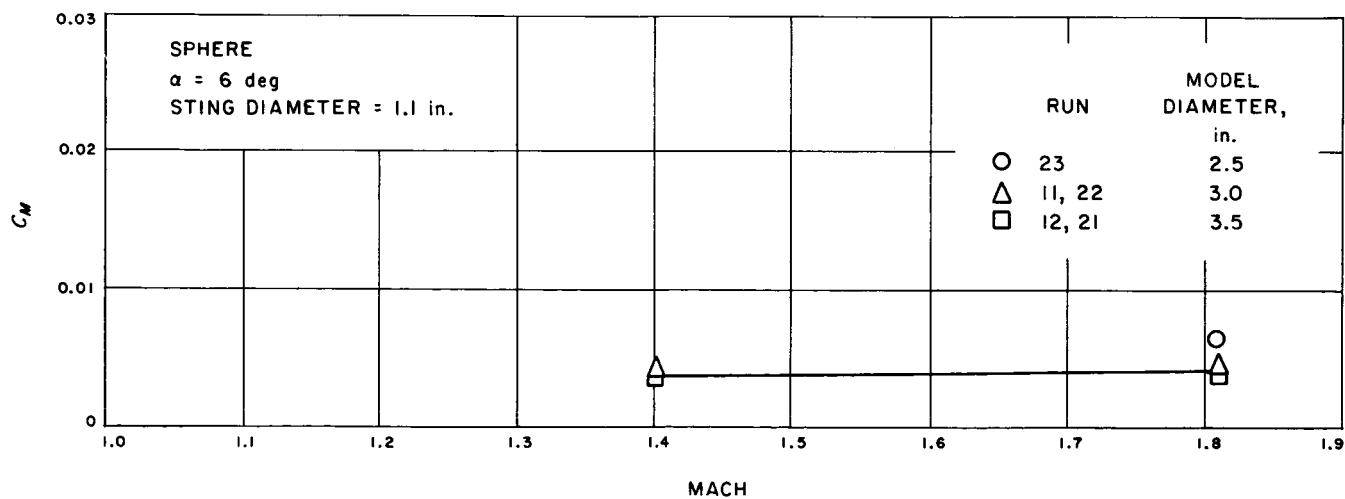
Plot 61. C.P. (in.) vs Mach for an entry shape

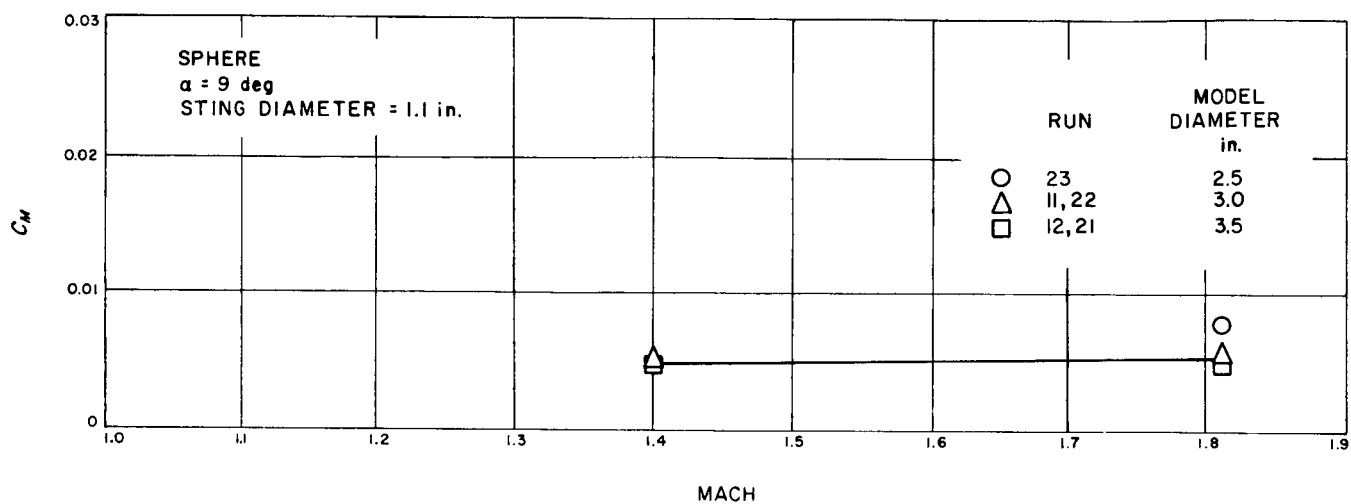
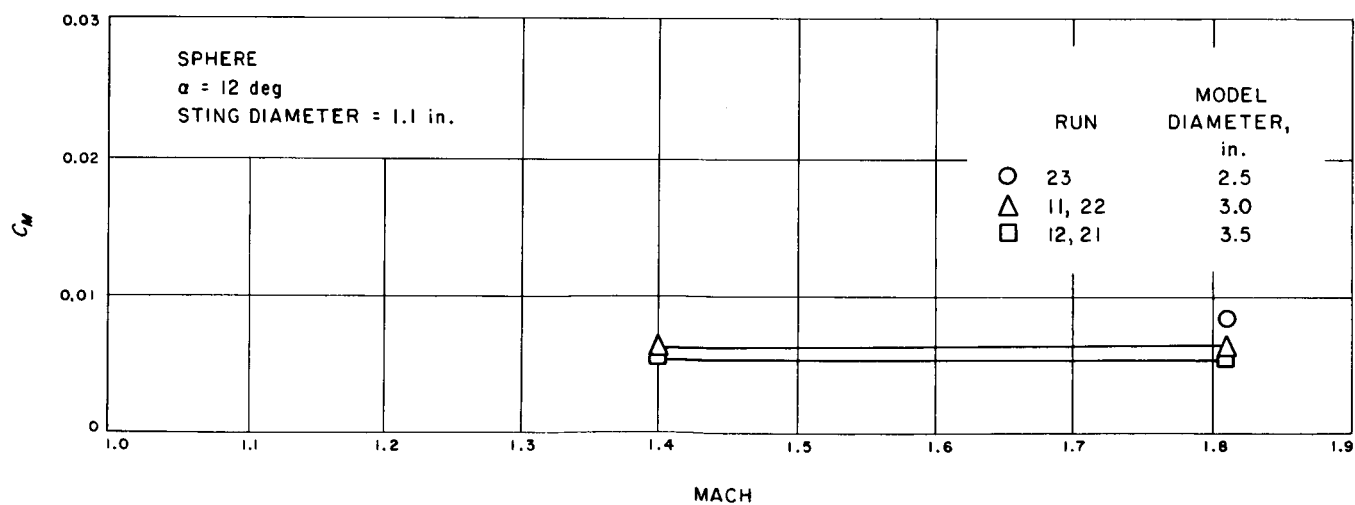
Plot 62. $C.P.$ (in.) vs Mach for an entry shapePlot 63. $C.P.$ (in.) vs Mach for an entry shape

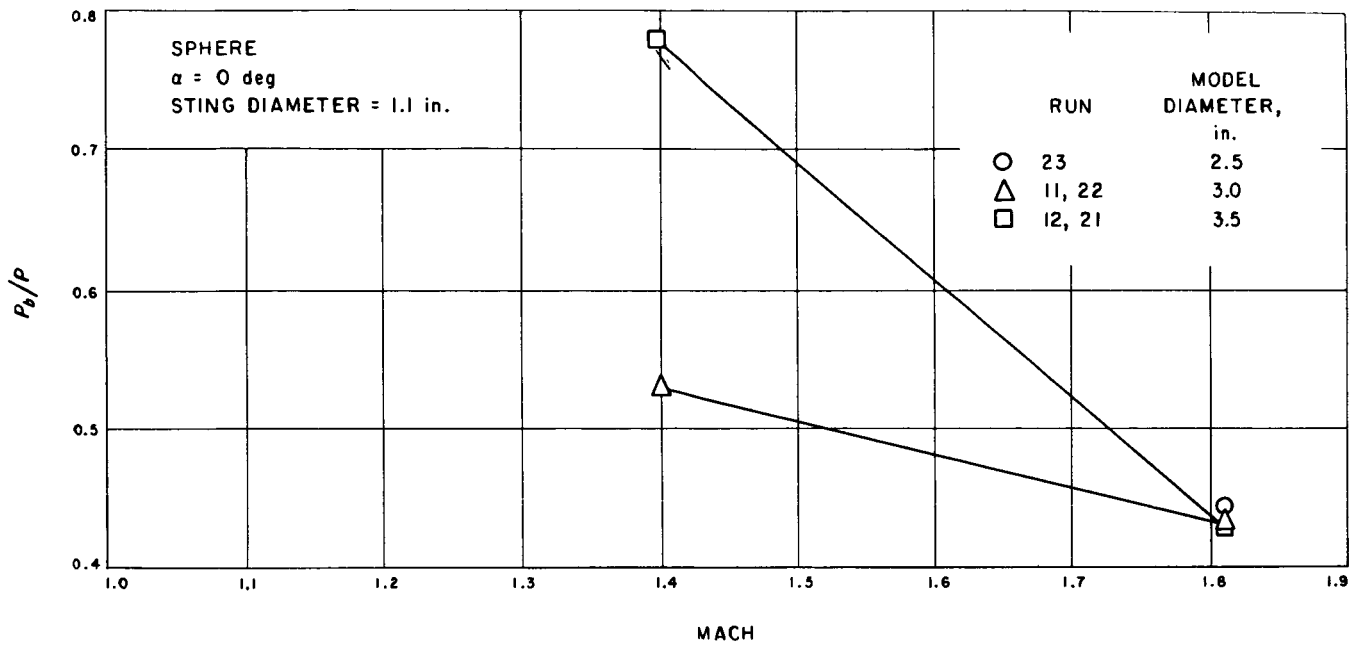
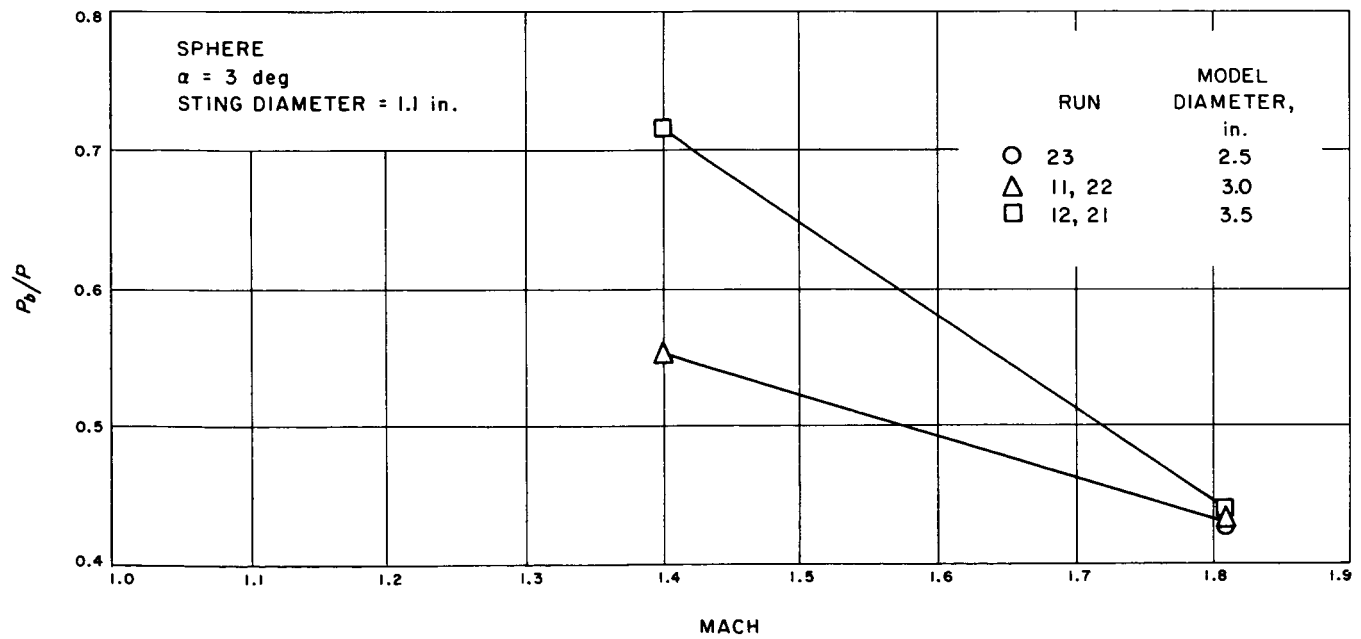
Plot 64. C_L vs Mach for a spherePlot 65. C_L vs Mach for a sphere

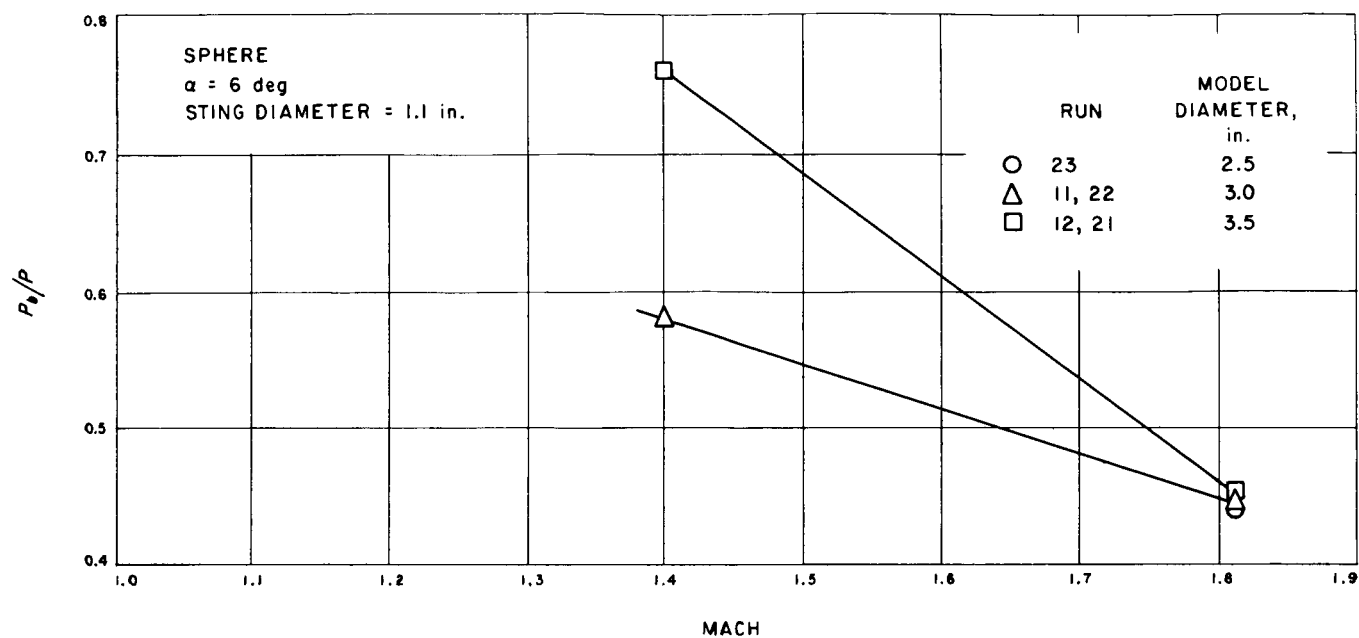
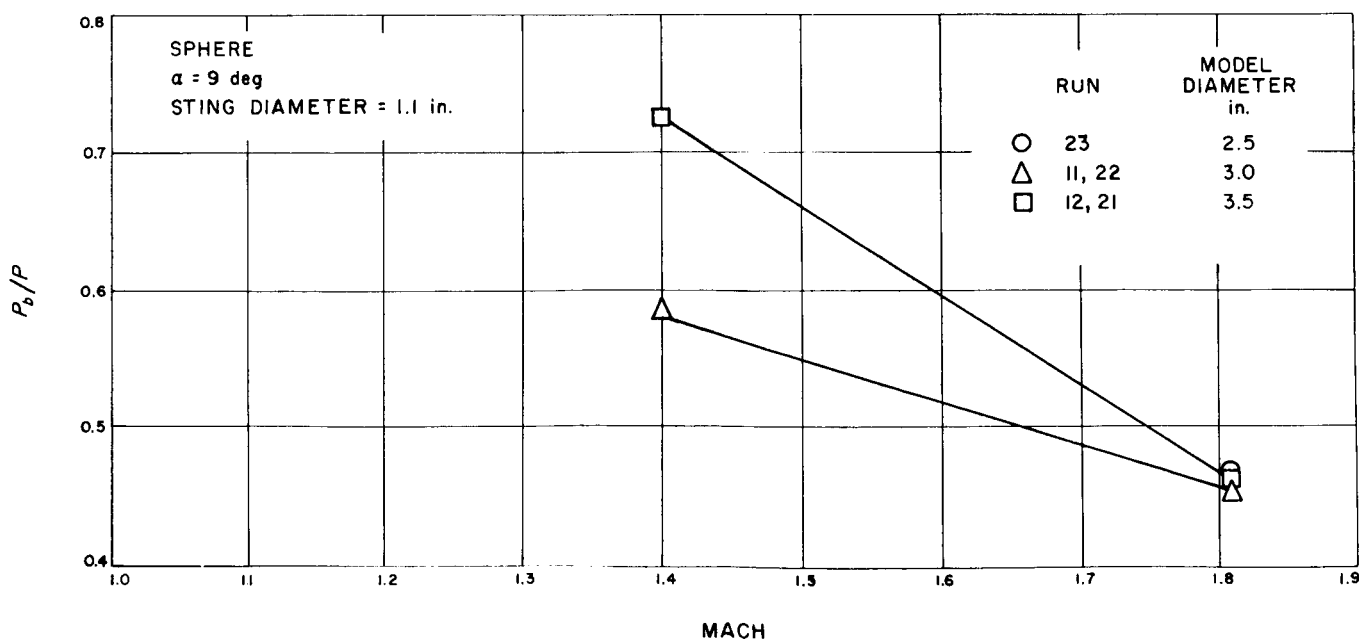
Plot 66. C_L vs Mach for a spherePlot 67. C_L vs Mach for a sphere

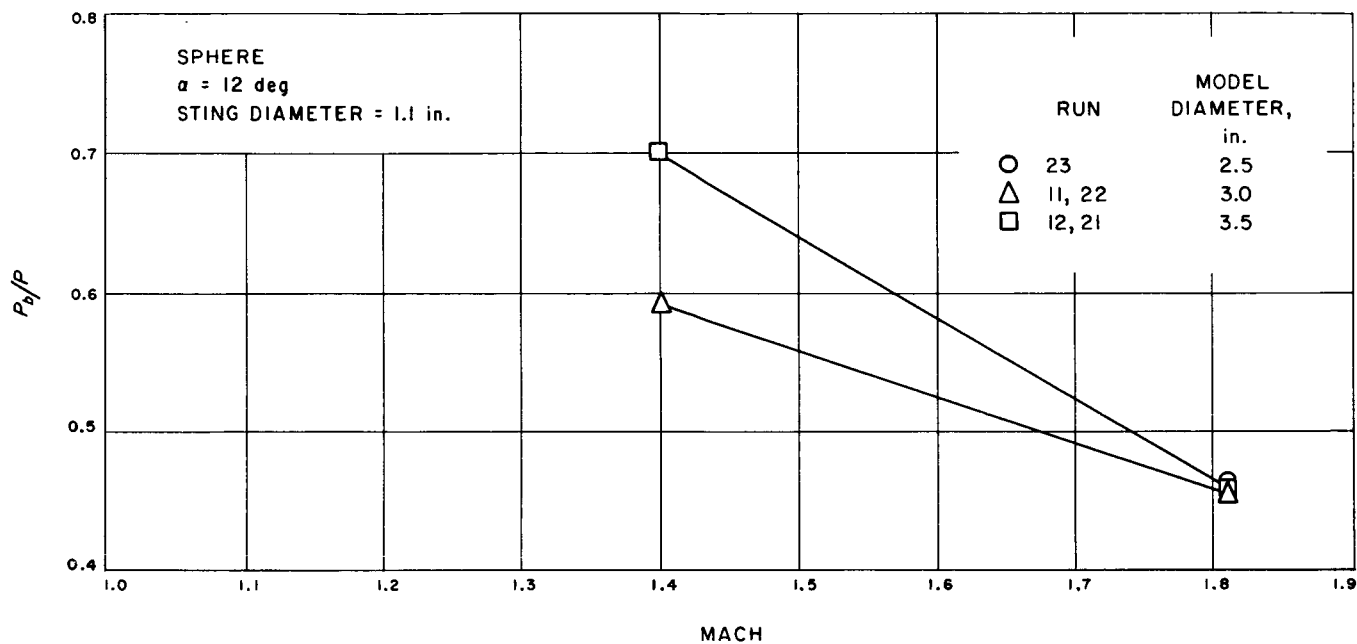
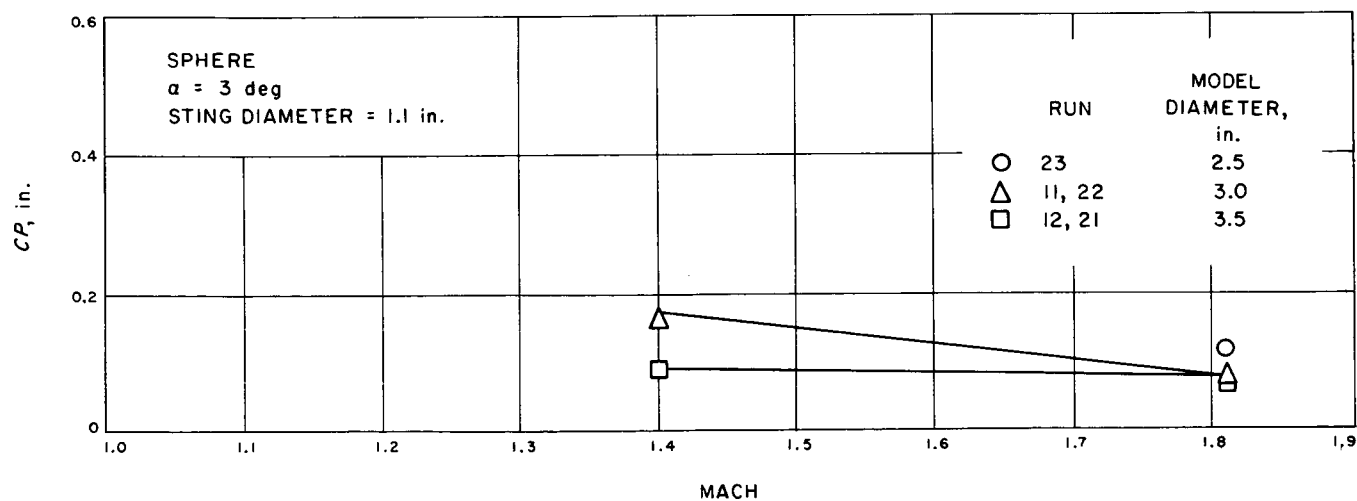
Plot 68. C_L vs Mach for a spherePlot 69. C_M vs Mach for a sphere

Plot 70. C_M vs Mach for a spherePlot 71. C_M vs Mach for a sphere

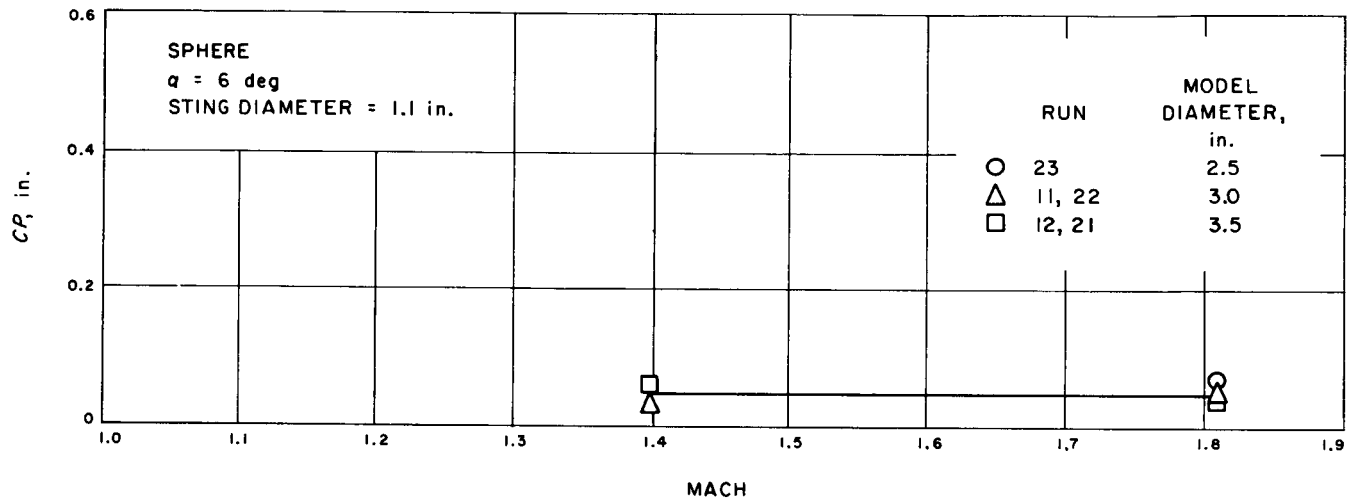
Plot 72. C_M vs Mach for a spherePlot 73. C_M vs Mach for a sphere

Plot 74. P_0/P vs Mach for a spherePlot 75. P_0/P vs Mach for a sphere

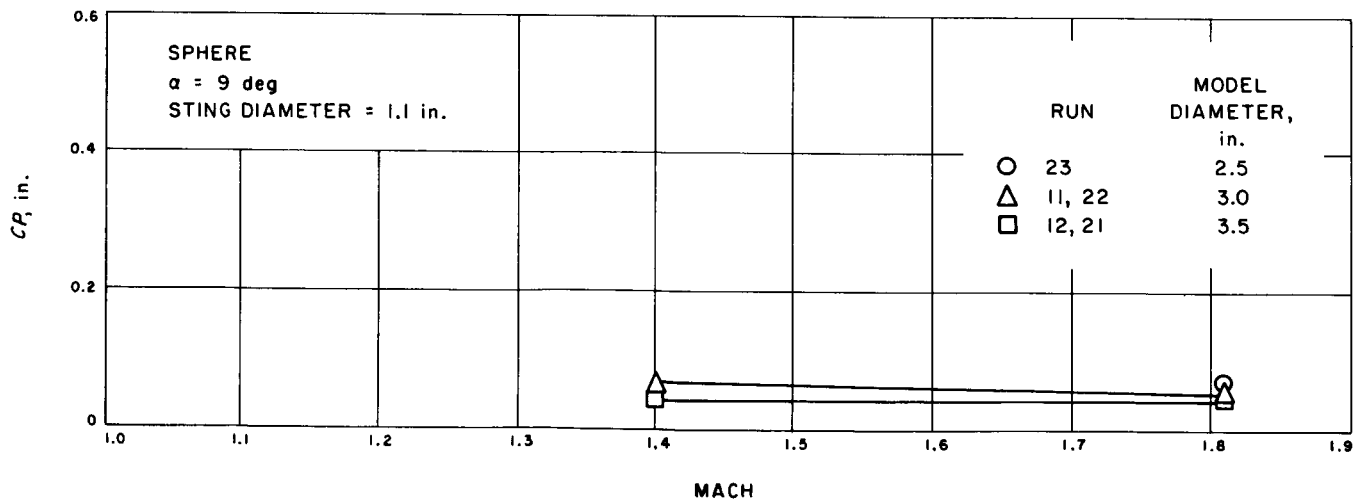
Plot 76. P_b/P vs Mach for a spherePlot 77. P_b/P vs Mach for a sphere

Plot 78. P_b/P vs Mach for a sphere

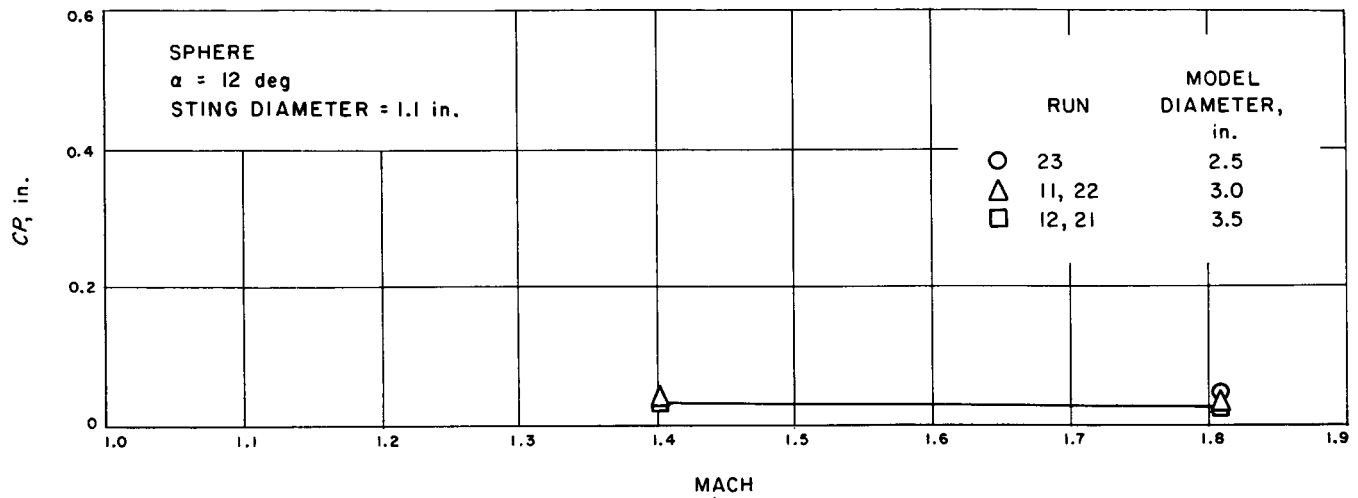
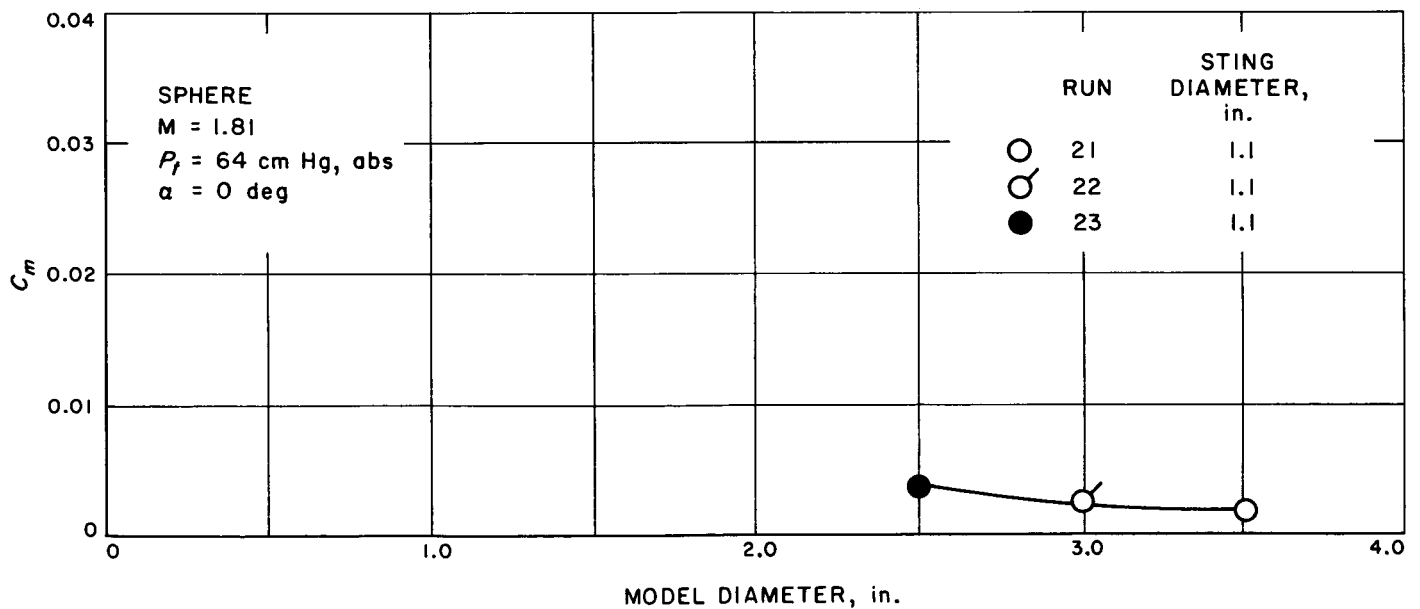
Plot 79. C.P. (in.) vs Mach for a sphere

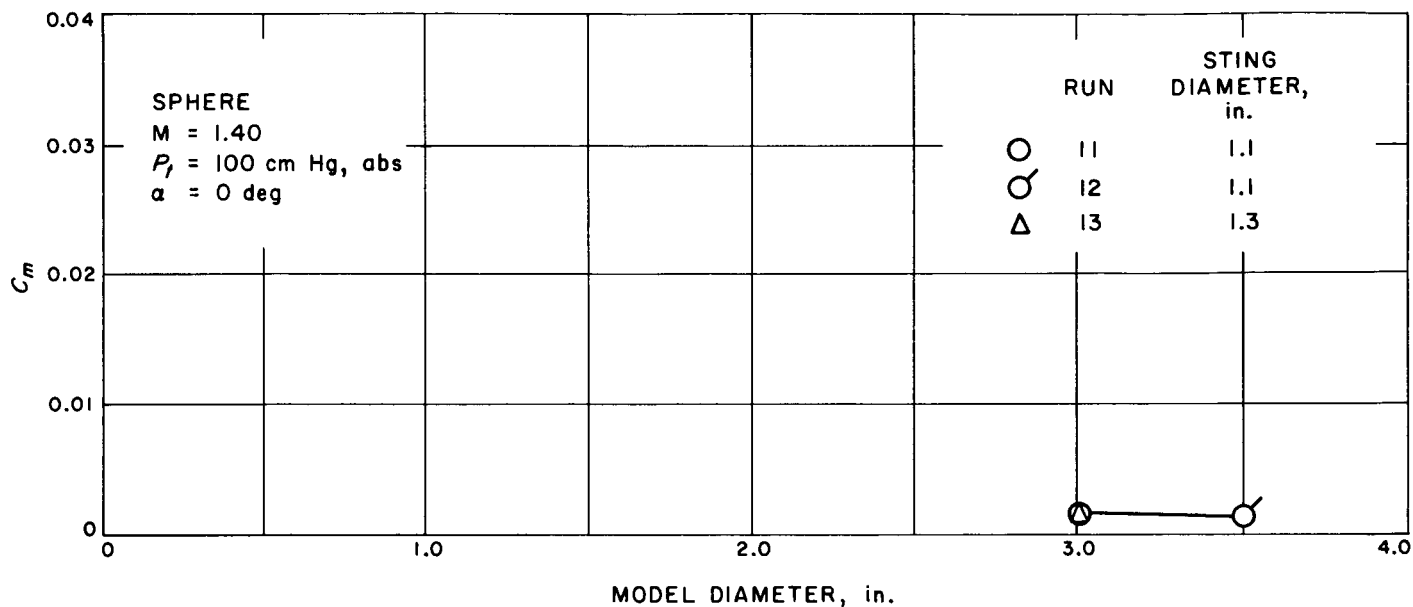
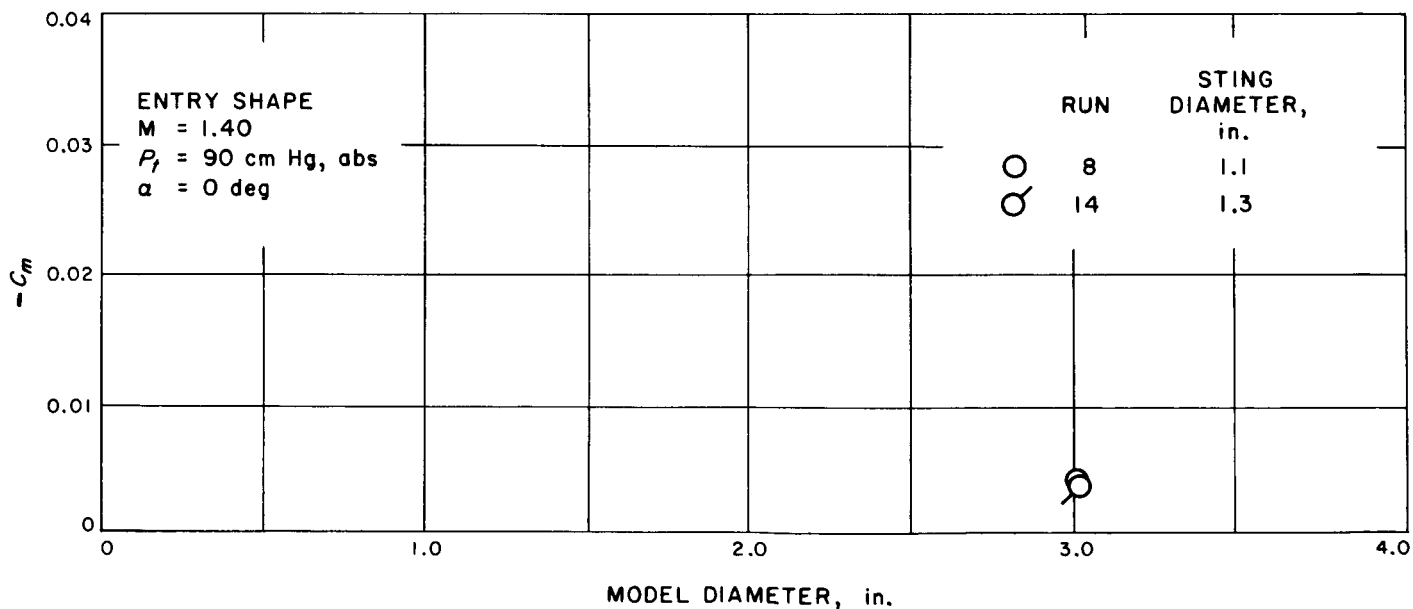


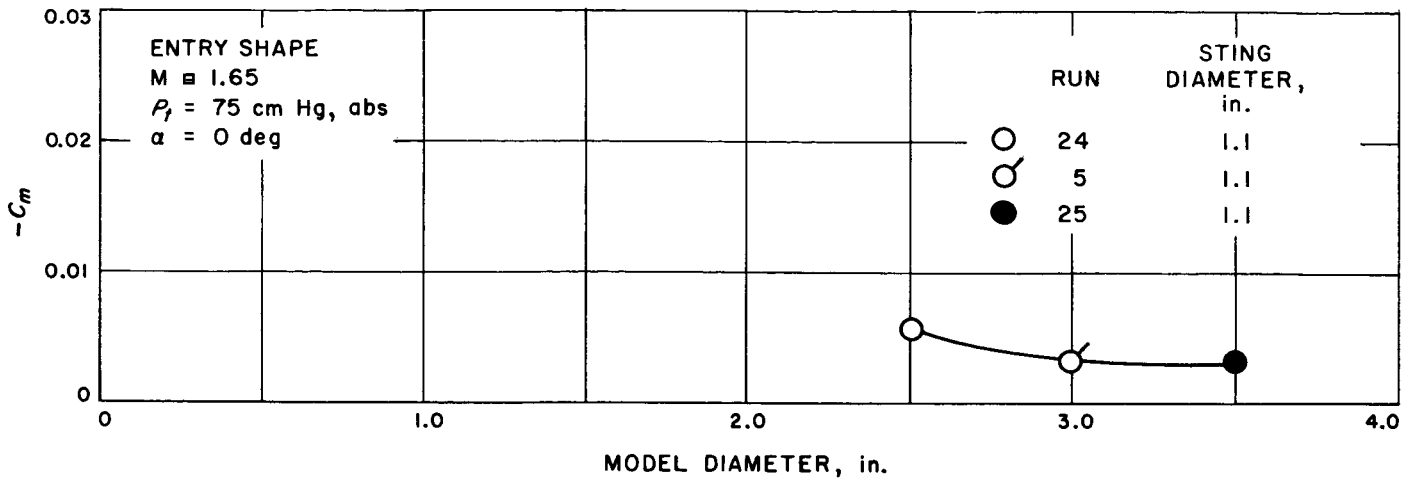
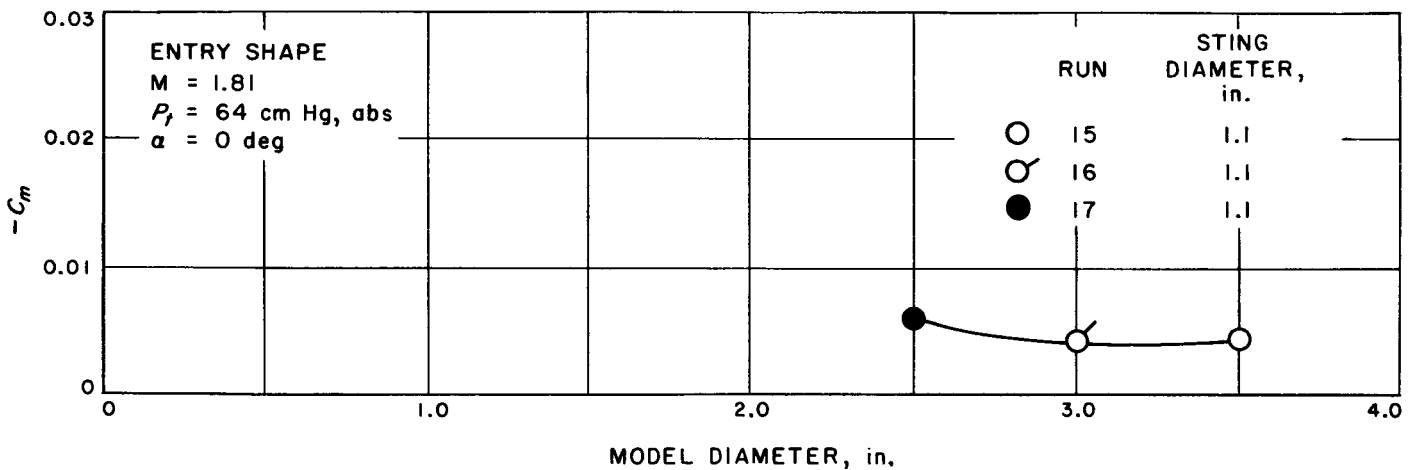
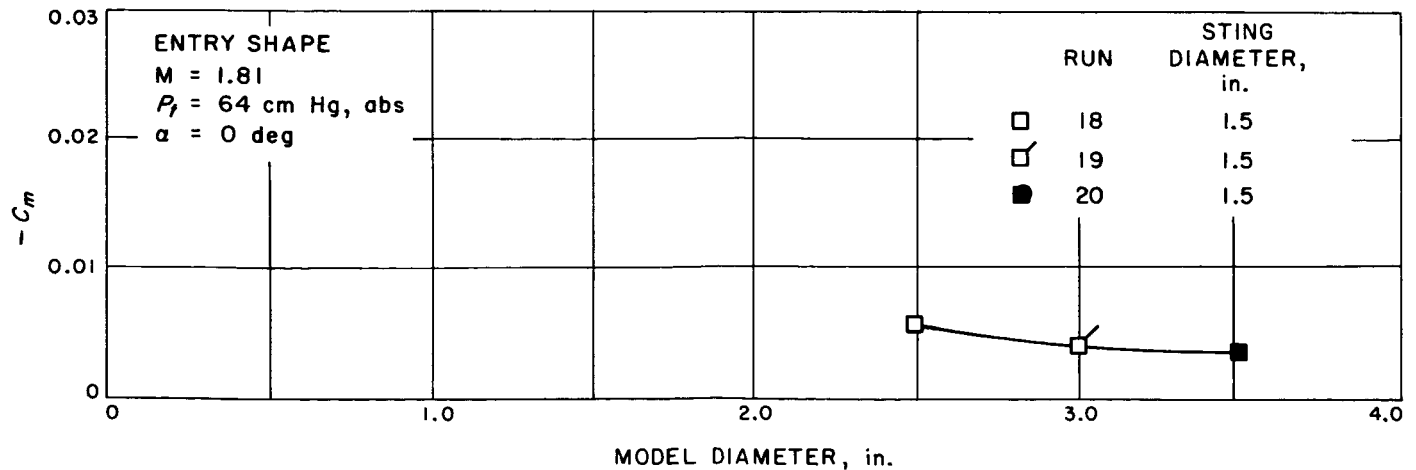
Plot 80. C.P. (in.) vs Mach for a sphere



Plot 81. C.P. (in.) vs Mach for a sphere

Plot 82. $C.P.$ (in.) vs Mach for a spherePlot 83. C_m vs model diameter (in.) for a sphere

Plot 84. C_m vs model diameter (in.) for a spherePlot 85. $-C_m$ vs model diameter (in.) for an entry shape

Plot 86. $-C_m$ vs model diameter (in.) for an entry shapePlot 87. $-C_m$ vs model diameter (in.) for an entry shapePlot 88. $-C_m$ vs model diameter (in.) for an entry shape